Precast Bent System for High Seismic Regions

Laboratory Tests of Column-to-Drilled Shaft Socket Connections

Publication No. FHWA-HIF-13-038

June 2013

HIGHWAYS FOR LIFE

Accelerating Innovation for the American Driving Experience.

Photo courtesy of the Precast/Prestressed Concrete Institute

U.S.Department of Transportation

Federal Highway Administration

Notice

This document is disseminated under the sponsorship of the U.S. Department of Transportation in the interest of information exchange. The U.S. Government assumes no liability for the use of the information contained in this document. This report does not constitute a standard, specification, or regulation.

The U.S. Government does not endorse products or manufacturers. Trademarks or manufacturers' names appear in this report only because they are considered essential to the objective of the document.

Quality Assurance Statement

The Federal Highway Administration (FHWA) provides high-quality information to serve Government, industry, and the public in a manner that promotes public understanding. Standards and policies are used to ensure and maximize the quality, objectivity, utility, and integrity of its information. FHWA periodically reviews quality issues and adjusts its programs and processes to ensure continuous quality improvement.

Technical Report Documentation Page

1. Report No. FHWA-HIF-13-038	2. Government Accession No. N/A	3. Recipient's Catalog No. N/A
4. Title and Subtitle PRECAST BENT SYSTEM FOR HIGH SEISMIC REGIONS: LABORATORY TESTS OF COLUMN-TO-DRILLED SHAFT SOCKET CONNECTIONS		5. Report Date May 2013 6. Performing Organization Code
7. Author(s) Hung Viet Tran[1], John F. Stanton[1], and Marc O. Eberhard[1]		8. Performing Organization Report No.
9. Performing Organization Name and Address BergerABAM, Inc. 33301 Ninth Ave South, Suite 300 Federal Way, WA 98003 [1] University of Washington, Seattle, WA		10. Work Unit No. 11. Contract or Grant No. DTFH61-09-G-00005
12. Sponsoring Agency Name and Address Federal Highway Administration Highways for LIFE Program Office 1200 New Jersey Avenue, SE Washington, DC 20590		13. Type of Report and Period Covered Final Report 14. Sponsoring Agency Code

15. Supplementary Notes

This is a companion report to the final project report, *Precast Bent System for High Seismic Regions* (FHWA-HIF-13-037).

16. Abstract

This report provides detailed information from the laboratory investigation of two precast column-to-drilled shaft large-scale tests, including descriptions of the specimen design, testing, data reduction, and conclusions regarding the use of the connection with the precast bent system.

The tests provide data regarding the performance of the precast column-to-drilled shaft connection. The results indicate that the connection, when used with a precast column, is sufficiently strong to resist plastic hinging in the column above the drilled shaft splice zone. The column reinforcing bars were anchored with headed bar ends to facilitate column strength development. The behavior is emulative of cast-in-place performance. The specimens tested were based on the minimum practical difference in diameters of the shaft relative to the column. When adequate confinement in the reinforcing cage of the shaft is included in the splice zone, the column can form a plastic hinging mechanism above the shaft without incurring damage in the shaft splice zone. If sufficient confinement is not included, then the resulting behavior is undesirable because the splice zone strength rapidly deteriorates.

Recommendations for transverse reinforcement are provided to ensure desirable performance, and these result in more reinforcement in the upper portion of the splice zone than in the lower portion.

17. Key Words	18. Distribution Statement
Bridges, earthquakes, accelerated bridge construction, precast bent, connections, drilled shaft foundations, prefabricated bridge elements and systems	No restrictions. This document is available to the public through the National Technical Information Service, Springfield, VA 22161.

9. Security Classif. (of this report)	20. Security Classif. (of this page)	21. No. of Pages	22. Price
Unclassified	Unclassified	125	

PREFACE

This report consists of the following seven chapters:

Chapter 1 provides background and overview material, including the socket connection concept and the research objective and scope.

Chapter 2 covers the design of the test specimens.

Chapter 3 provides a description of the test setup, instrumentation, and the method of control of the testing process.

Chapter 4 provides a definition of the damage states that were observed and an overview of the damage progression that occurred during testing.

Chapter 5 provides the measured response of the two specimens, including force and moment vs. displacement plots, curvature distributions, displacement histories, and strain histories. Strain histories are provided for all the principal reinforcement types.

Chapter 6 covers the analysis of the observed and recorded data, and it provides a detailed treatment of a proposed strut-and-tie model developed to describe the flow of internal forces. This model is then used to interpret the results.

Chapter 7 provides a summary, conclusions, and recommendations.

Several appendices also are included to provide more detailed information that may be useful in understanding the response of the specimens and the progression of damage.

SI* (MODERN METRIC) CONVERSION FACTORS

APPROXIMATE CONVERSIONS TO SI UNITS

Symbol	When You Know	Multiply By	To Find	Symbol
		LENGTH		
in	inches	25.4	millimeters	mm
ft	feet	0.305	meters	m
yd	yards	0.914	meters	m
mi	miles	1.61	kilometers	km
		AREA		
in^2	square inches	645.2	square millimeters	mm^2
ft^2	square feet	0.093	square meters	m^2
yd^2	square yard	0.836	square meters	m^2
ac	acres	0.405	hectares	ha
mi^2	square miles	2.59	square kilometers	km^2
		VOLUME		
fl oz	fluid ounces	29.57	milliliters	mL
gal	gallons	3.785	liters	L
ft^3	cubic feet	0.028	cubic meters	m^3
yd^3	cubic yards	0.765	cubic meters	m^3
	NOTE: volumes greater than 1000 L shall be shown in m^3			
		MASS		
oz	ounces	28.35	grams	g
lb	pounds	0.454	kilograms	kg
T	short tons (2000 lb)	0.907	megagrams (or "metric ton")	Mg (or "t")
		TEMPERATURE (exact degrees)		
°F	Fahrenheit	5 (F-32)/9 or (F-32)/1.8	Celsius	°C
		ILLUMINATION		
fc	foot-candles	10.76	lux	lx
fl	foot-Lamberts	3.426	$candela/m^2$	cd/m^2
		FORCE and PRESSURE or STRESS		
lbf	poundforce	4.45	newtons	N
lbf/in^2	poundforce per square inch	6.89	kilopascals	kPa

APPROXIMATE CONVERSIONS FROM SI UNITS

Symbol	When You Know	Multiply By	To Find	Symbol
		LENGTH		
mm	millimeters	0.039	inches	in
m	meters	3.28	feet	ft
m	meters	1.09	yards	yd
km	kilometers	0.621	miles	mi
		AREA		
mm^2	square millimeters	0.0016	square inches	in^2
m^2	square meters	10.764	square feet	ft^2
m^2	square meters	1.195	square yards	yd^2
ha	hectares	2.47	acres	ac
km^2	square kilometers	0.386	square miles	mi^2
		VOLUME		
mL	milliliters	0.034	fluid ounces	fl oz
L	liters	0.264	gallons	gal
m^3	cubic meters	35.314	cubic feet	ft^3
m^3	cubic meters	1.307	cubic yards	yd^3
		MASS		
g	grams	0.035	ounces	oz
kg	kilograms	2.202	pounds	lb
Mg (or "t")	megagrams (or "metric ton")	1.103	short tons (2000 lb)	T
		TEMPERATURE (exact degrees)		
°C	Celsius	1.8C+32	Fahrenheit	°F
		ILLUMINATION		
lx	lux	0.0929	foot-candles	fc
cd/m^2	$candela/m^2$	0.2919	foot-Lamberts	fl
		FORCE and PRESSURE or STRESS		
N	newtons	0.225	poundforce	lbf
kPa	kilopascals	0.145	poundforce per square inch	lbf/in^2

*SI is the symbol for the International System of Units. Appropriate rounding should be made to comply with Section 4 of ASTM E380.
(Revised March 2003)

TABLE OF CONTENTS

LIST OF FIGURES

LIST OF TABLES

LIST OF ABBREVIATIONS AND ACRONYMS

AASHTO	American Association of State Highway and Transportation Officials
ABC	Accelerated Bridge Construction
BDM	Bridge Design Manual
HSS	Hollow structural section
LRFD	Load and Resistance Factor Design
LVDT	Linear variable differential transformer
MEF	Maximum effective force
PTFE	Polytetraflouroethylene
WSDOT	Washington State Department of Transportation

NOTATION

A_{tr} = Area of shaft transverse reinforcement or spiral (in^2)

A_l = Total area of longitudinal column reinforcement (in^2)

$A_{l,sh}$ = Total area of longitudinal shaft reinforcement (in^2)

c = Depth to the neutral axis

D = Diameter of shaft spiral (in.)

d = Distance from the extreme compression fiber to the extreme tension longitudinal reinforcement

e = Distance from the inner bar to the outer bar

E_s = Modulus of elasticity of reinforcement (ksi)

f_r = Concrete modulus of rupture (ksi)

f_s = Tensile stress in reinforcement (ksi)

f_{yt} = Specified minimum yield strength of shaft transverse reinforcement (ksi)

f_{ul} = Specified minimum tensile strength of column longitudinal reinforcement (ksi), 90 ksi for A615 and 80 ksi for A706

l_{ns} = Total noncontact lap splice length

l_s = Class C tension lap splice length of the column longitudinal reinforcement (in.)

L_{tr} = Distance between the outer bars

R = Radius of shaft spiral (in.)

s_{tr} = Spacing of shaft transverse reinforcement (in.)

VOL_s = Total volume of steel, including both longitudinal and transverse in the splice

ϵ_s = Tensile strain in reinforcement (ksi)

θ = Inclination angle of the strut (degree or rad)

Φ = Curvature (1/in.)

CHAPTER 1. INTRODUCTION

THE NEED FOR RAPID CONSTRUCTION

Bridge substructures are most commonly constructed of cast-in-place concrete. Despite having some clear advantages (e.g., ease of transportation and to making continuous connections), cast-in-place concrete has two main drawbacks: long on-site construction times and large labor requirements in the field, which can result in high construction costs. Using cast-in-place construction for bridge replacement is particularly disruptive when it exacerbates traffic congestion. Therefore, there is an urgent need to develop methods for accelerating bridge construction.

Using precast bridge elements is one solution for reducing on-site construction time, field labor requirements, and traffic delays. Although large substructures (and even full bridges) can be constructed off-site, precast elements are usually limited to beams and columns to make fabrication and transportation easier. The quality of the individual precast elements cast in a factory often exceeds the quality of elements cast in the field. However, maintaining quality in the on-site connections between these precast elements is more difficult. Achieving good connections is particularly challenging in seismically hazardous areas, like the Pacific Northwest, in which the largest forces are developed at the beam-to-column or column-to-footing connections. Therefore, it is vital to develop economical connections that are strong enough to resist seismic excitation and easy to construct with high quality.

SOCKET CONNECTION CONCEPT

A lot of research has been performed on precast bridge connections, but mainly for applications in which the seismic demands are low.[1] Less research has been performed for applications in seismically active regions. Hieber et al. summarized the state of the art in this area in 2005.[2] Since then, Hieber et al. performed numerical analyses of precast piers, and Wacker et al. developed displacement and force-based design procedures.[3,4]

In 2008, Pang et al. proposed using “large-bar” connections to connect beams and columns.[5] They proposed to connect the elements with a small number of large bars that would fit into large ducts. Steuck et al. showed that bars as large as No. 18 could be anchored within the typical depth of a cap beam.[6,7] Cohagen et al. later proposed using unbonded post-tension strands to help re-center the column after the earthquake.[8] In 2011, Restrepo et al. summarized the development of a precast concrete bent-cap system for seismic regions.[9] Haraldsson developed the concept of using a socket connection to connect the base of a precast column with a cast-in-place spread footing.[10]

This report adapts the column-to-foundation socket concept to connections between a precast column and cast-in-place drilled shaft, which has a lot of benefit in bridge construction in urban areas. In this connection, the bottom of the precast column is roughened, where it will be embedded in the drilled shaft.

The construction stages are shown in figure 1.

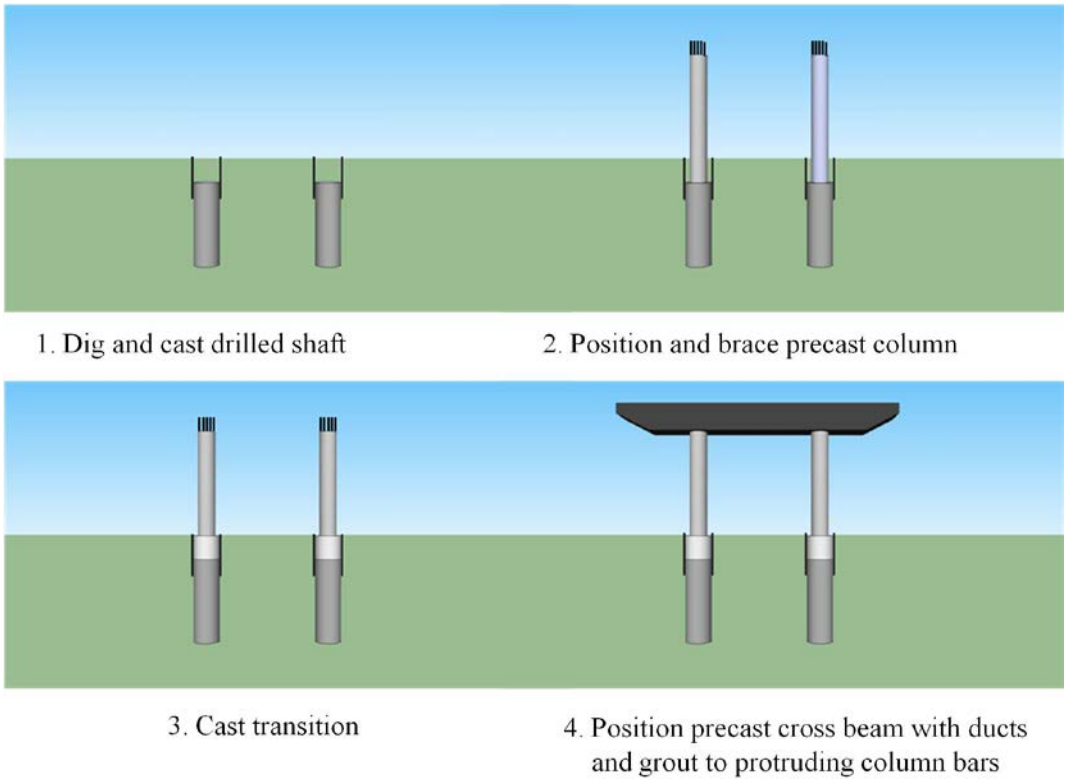

Figure 1. Diagram. Precast bridge bent construction stages.

RESEARCH OBJECTIVES AND SCOPE

The objective of this research is to evaluate the behavior of precast column-to-drilled shaft connections. Particular emphasis is placed on inelastic behavior under cyclic excitations that may occur during a severe earthquake. Experimental and analytical studies of the behavior of the connection are described. The behavior is discussed with respect to quasi-static hysteretic behavior under cyclic loads.

This research was designed to answer the following questions:

- Does the column-to-drilled shaft connection behave like a non-contact lap splice, as assumed in the Washington State Department of Transportation (WSDOT) Bridge Design Manual (BDM)?[(11)]
- Does the WSDOT BDM design formula for proportioning transverse reinforcement of the shaft transition result in acceptable seismic response?
- Do the three wraps of spiral at the end of the shaft work like anchorage or undergo large lateral force transmitted by the column?

Two scaled (1/3.6) tests were performed. One specimen was designed to satisfy the current design specifications for cast-in-place systems, as described in the following references:

- American Association of State Highway and Transportation Officials (AASHTO) Load and Resistance Factor Design (LRFD) Bridge Design Specifications.[12]
- AASHTO Seismic Guide Specifications.[13]
- WSDOT BDM.[11]

The second specimen was designed similarly, except that the spiral in the shaft was reduced by half, with the intention that the specimen would fail in the shaft.

CHAPTER 2. DESIGN OF TEST SPECIMENS

Two drilled shaft-column connection specimens (DS-1 and DS-2) were designed, constructed, and tested at the University of Washington. The design and construction of the specimens are described in this chapter. The detailed design drawings are shown in appendix A, and the material test reports are shown in appendix B.

CONFIGURATION OF TEST SPECIMENS

The two specimens each consisted of a precast column, embedded in a cast-in-place drilled shaft, which in turn was anchored to the testing rig by a cast-in-place base. For both specimens, these three components had the following geometries:

- Precast Column: The cantilever-precast columns had a diameter of 20 inches and a span of 60 inches, resulting in a shear span-to-depth ratio of 3.
- Drilled Shaft: The cast-in-place drilled shaft had a diameter of 30 inches and a length of 31 inches, which slightly exceeded the length of the transition region (28 inches).
- Base: The drilled shaft was embedded in a 74-inch by 48-inch by 24-inch cast-in-place base to anchor the specimen to the base of the testing rig.

The test specimen dimension and reinforcement were scaled (1/3.6) from a prototype, as shown in table 1. The diameter of the prototype column and shaft were chosen as 6 feet and 9 feet, respectively, to make the transition region more critical. The scale factor was chosen as 3.6 to match the 20-inch diameter of column specimens tested by previous researchers.[10,14]

The only difference between specimen DS-1 and specimen DS-2 was that the amount of spiral in the column-to-shaft transition region was reduced by half in DS-2.

Table 1. Prototype and specimen design dimensions.

	Prototype	**Specimen (*Scale factor: 1/3.6*)**
Column diameter	6 ft	20 in.
Shaft diameter	9 ft	30 in.
Column cover	2 in.	0.6 in.
Shaft cover	6 in.	1.7 in.

DESIGN OF PROTOTYPE AND TEST COLUMNS

The test column was designed to have a reinforcement ratio of 1 percent, which was provided using 10 No. 5 bars. The transverse reinforcement ratio was chosen as 0.82 percent to be consistent with previous tests done at the University of Washington. (See references 5, 8, 10, and

14.) Thus, the transverse reinforcement was 3-gauge (0.244-inch-diameter) spirals at a pitch of 1.25 inches. All reinforcement was assumed to be ASTM A706, and the nominal concrete strength was assumed to be 6 ksi.

The flexural strength of the column in the specimens was found by performing moment-curvature analysis using the Mphi18 program developed at the University of Washington. Steel properties were modeled according to the AASHTO Seismic Guide Specifications, and the confined concrete properties were modeled using Kent and Park's model.[15] However, the values of the confined concrete strength, the strain at peak stress, and the ultimate compression strain were generated from the properties of the confinement reinforcement using Mander's formula, rather than using the values recommended by Kent and Park.[16,17] Details of the moment-curvature analysis are shown in chapter 6. The constant axial load applied in the column was 10 percent the axial load capacity of the column ($0.1P_o$=159 kips). Using the above moment-curvature program, the ultimate moment capacity of column cross section was $M_u = 3{,}507$ kip-in.

The embedment part of the column (28 inches) had an octagonal shape and was circumscribed inside the circular section of the upper part of the column. The outside surface was intentionally roughened with a saw-tooth detail similar to the one required by the WSDOT BDM for prestressed girders. The dimension of the saw-tooth detail was used in the shear-friction design procedure proposed by the AASHTO LRFD. All dimensions designed for the prototype were scaled down to specimen dimensions.

The ends of the longitudinal column reinforcement were terminated with rebar end anchors, instead of using the more conventional detail of bending the longitudinal bars outwards into the foundation. This kind of anchor helped to reduce the development length of longitudinal reinforcement and made the connection between the precast column and cast-in-place drilled shaft more constructible.

DESIGN OF SPECIMEN COLUMN-TO-DRILLED SHAFT CONNECTION

The embedded length of the column in the drilled shaft was based on the scaled-down non-contact lap splice length of the shaft prototype according to the WSDOT BDM. This length calculation was proposed by McLean and Smith.[18] The embedded length is equal to $l_{ns} = l_s + e$, where $l_{ns} =$ length of noncontact lap splice, $l_s =$ lap splice length required by AASHTO LRFD 5.11.5.3 or $l_s = 1.7l_d$ (for a Class C lap splice) where l_d is the development length of the larger bar, and $e =$ distance between the shaft and column longitudinal reinforcement.

The shaft longitudinal reinforcement was designed to form a plastic hinge in the column. Therefore, the yield moment of the shaft had to be larger than the moment at the base of the shaft (5,319 kip-in.) due to the overstrength moment and shear from the column above. Calculation showed that using 30 bundles with 2 No. 3 bars per bundle for the longitudinal shaft reinforcement in the test specimens would satisfy the requirement.

The shaft spirals were designed as non-contact lap splices according to the WSDOT BDM, sections 7.4.4 and 7.8.2. Accordingly, the spacing for spiral was given as shown in figure 2.

$$s_{tr} = \frac{2\pi A_{sp} f_{ytr} l_s}{k A_l f_{ul}}$$

Figure 2. Equation. Spacing of shaft spiral.

In addition, the spirals within non-contact lap splice zone should not be less than No. 6 at 6-inch pitch in the prototype. However, the spacing should not exceed 9 inches.

To satisfy all these requirements, No. 6 spirals at 8-inch pitch were used in prototype, which would be a bundle of two 9-gauge wires (0.148-inch diameter) at 3-inch pitch. However, in specimen DS-2, to increase the likelihood of failure in the connection, the amount of spiral was reduced by half to one 9-gauge wire at 3-inch pitch. The shaft reinforcement details are summarized in table 2.

Table 2. Shaft reinforcement.

Item	Prototype	DS-1	DS-2
Longitudinal reinforcement	Two No. 11 bars per bundle, total of 30 bundles	Two No. 3 bars per bundle, total of 30 bundles	Two No. 3 bars per bundle, total of 30 bundles
Spiral	No. 6 at 8-in. pitch	Two 9-gauge wires at 3-in. pitch	One 9-gauge wire at 3-in. pitch

WSDOT BDM section 7.4.5 requires three turns of the wire at the end to terminate the spiral. This is an anchorage requirement. However, in the case of the column-shaft connection, it was believed that the extra turns also provided extra strength at the top of the transition region.

The bottom of the shaft connected with a 74-inch by 48-inch by 24-inch cast-in-place footing to attach the specimen to the testing rig. The longitudinal bars of the drilled shaft were hooked at the bottom mat of the footing, as shown in figures 3 and 4.

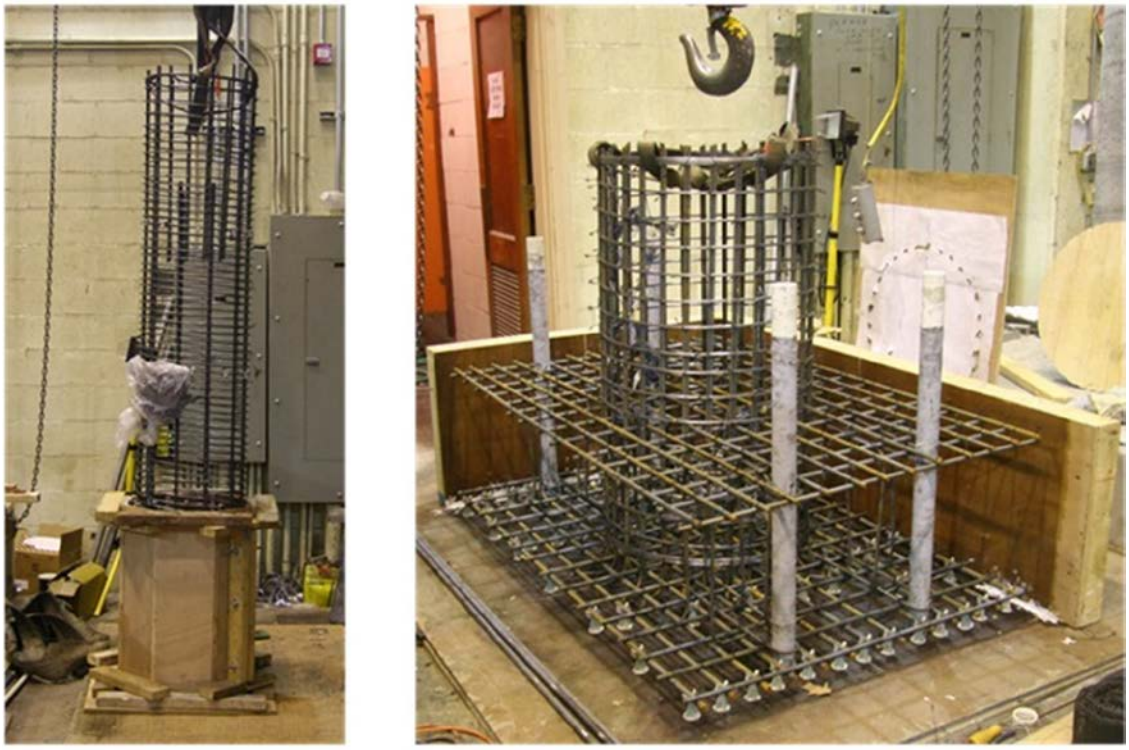

Figure 3. Photos. Column reinforcement (left) and shaft-footing reinforcement (right).

Figure 4. Photos. Specimen construction (left) and specimen test setup (right).

CHAPTER 3. EXPERIMENTAL PROGRAM

Quasi-static, cyclic tests were performed to evaluate the seismic performance of two column-to-drilled-shaft connections (DS-1 and DS-2). In such testing, deformations are applied at a rate much lower than would be applied during an earthquake.

This chapter describes the test setup, displacement history, instrumentation, and data acquisition. The two drilled-shaft tests were part of a larger research program seeking to develop a family of connections for rapid construction of bridges. Therefore, the experimental program for these tests was similar the ones conducted by Haraldsson and Janes on spread footings.[10,14]

TEST SETUP

The two specimens were tested by using the self-reacting rig shown in figure 5. The rig included a base, two vertical columns, a horizontal beam, two diagonal braces, and a servo-controlled actuator:

- The base consisted of two blocks of concrete, attached to two W24x94 beams, one on each side of the blocks. These components were post-tensioned together by four, threaded Williams bars placed in plastic tubes through the blocks and beams.
- Two vertical W24x94 columns were welded at the end of the two base beams.
- A horizontal W14x14 beam was bolted to the two vertical columns at the same level as the lateral load.
- The two vertical beams of the frame were stiffened on each side with a diagonal horizontal structural section (HSS) 6x6x3/8.
- The lateral loads were applied to the column with a servo-controlled actuator with a capacity of 220 kips. One end of the actuator was attached to the column, and the other end was connected to the horizontal beam.

The specimens were positioned in the rig, leveled with shims, and then attached to the base with Hydro-stone. To prevent the specimen from overturning under cyclic excitations, four threaded 1.25-inch-diameter Williams bars were placed in plastic tubes through the footing of specimens and threaded into nut cast into the concrete block of the rig's base. The top nuts on these bolts were tightened to 125 kips to hold the footing of the specimens down to the base.

The column axial load was provided by the 2.4-million-lb. Baldwin Universal Testing Machine. The force was transferred to the column through a spherical bearing. The top of the bearing slid in a channel attached to the Baldwin. To minimize friction, the spherical surface of the bearing was greased, a stainless steel plate was placed in the channel, and a greased sheet of polytetraflouroethylene (PTFE) was glued to the top and the sides of the bearing.

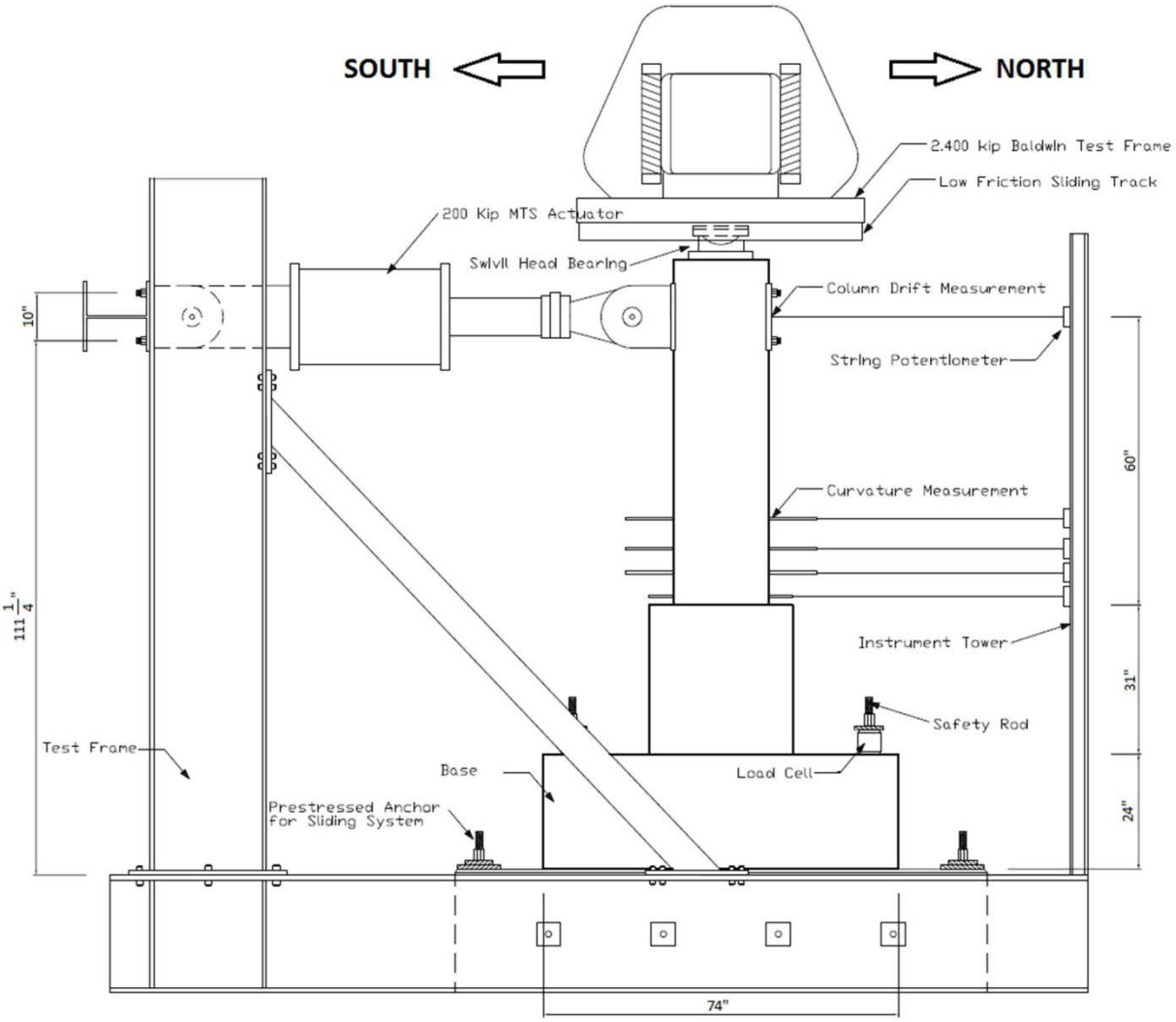

Figure 5. Diagram. Test setup.

INSTRUMENTATION

The axial load applied in the top of column was monitored by load cells in the Baldwin Universal Testing Machine. The lateral load was monitored by load cells in the MTS actuator. The response of the specimen was monitored by potentiometers, linear variable differential transformers (LVDTs), a research-grade motion capture system, and strain gauges.

The horizontal displacement of the column at the elevation of the lateral load (60 inches above the column-shaft interface) was monitored in two ways. On the north side, the displacement of the column was monitored with a string potentiometer attached to a steel reference column, which was unloaded, as shown in figure 6. In addition, the actuator displacement was monitored using the LVDT built into the actuator, and the displacement of the loading frame with respect to another unloaded frame was monitored by another LVDT (on the south side). Thus, a second measure of the absolute displacement of the column was calculated as the sum of displacement

of the actuator (MTS LVDT in figure 6) and the deformation of test rig. These two ways of measuring the top displacement yielded nearly identical results, as shown in figure 7.

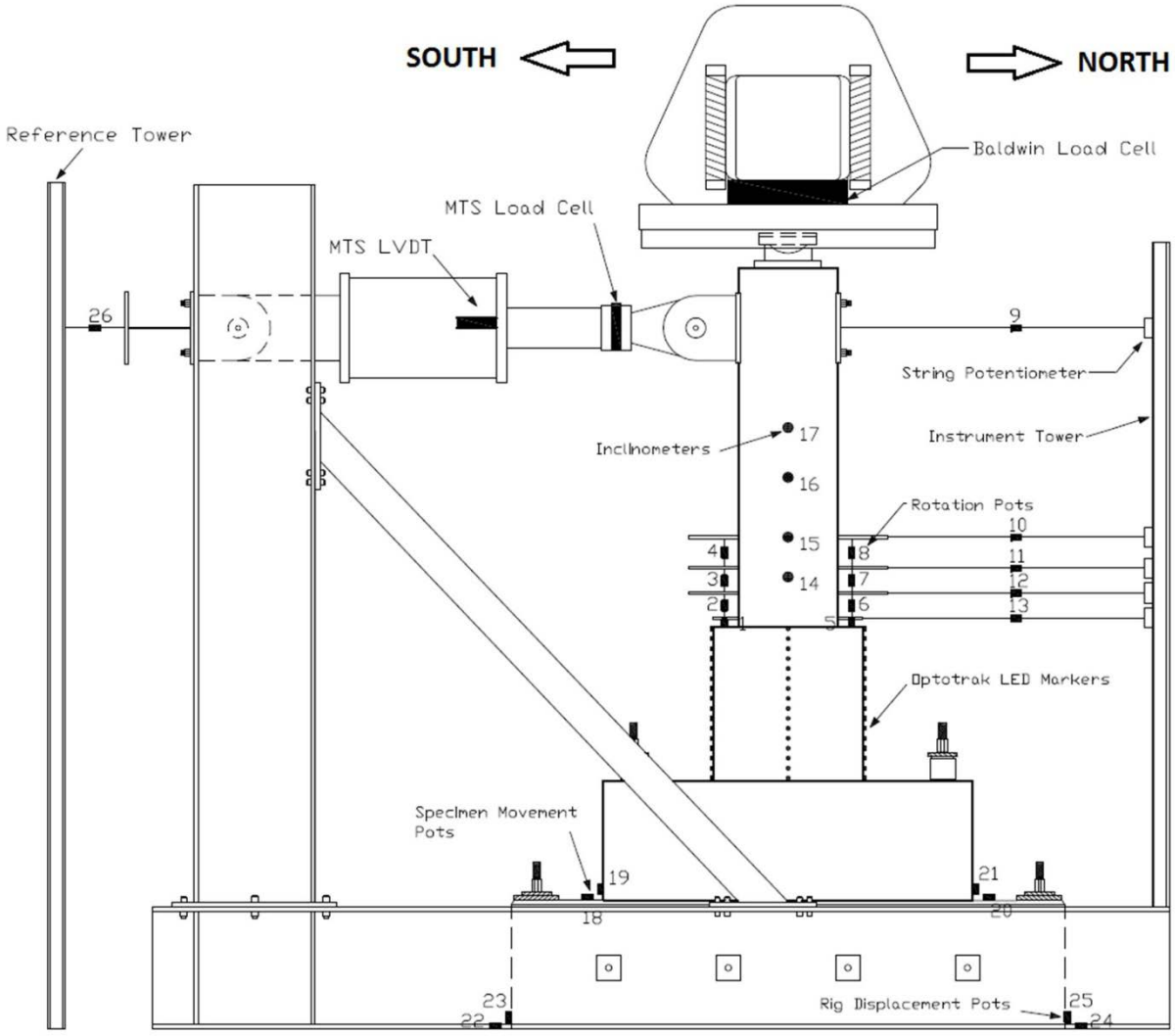

Figure 6. Diagram. Locations of external instruments.

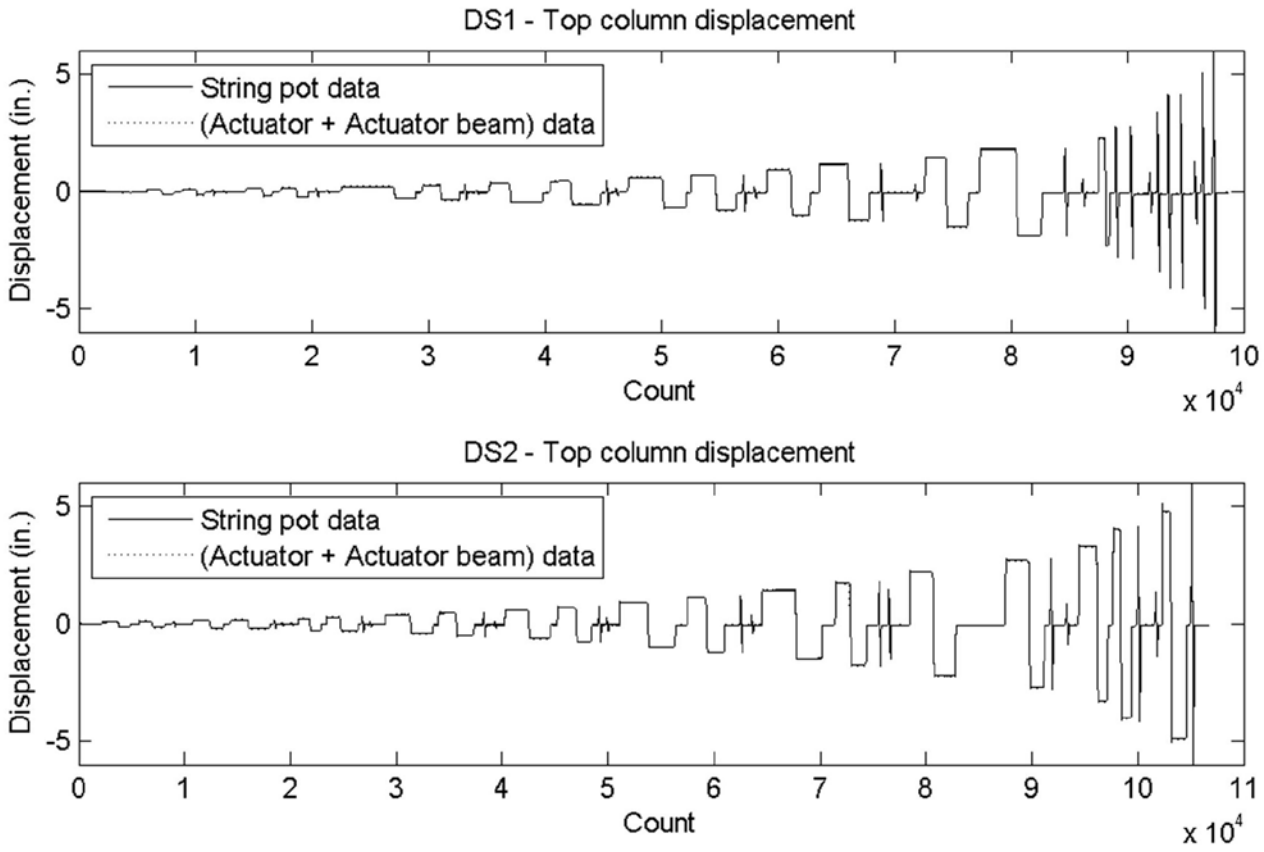

Figure 7. Diagram. Top column displacement comparison for DS-1 (top) and DS-2 (bottom).

The horizontal displacements of the column and transition region were monitored by string potentiometers. Four string potentiometers were connected to the end of the four north curvature rods to measure the displacement of column at these positions. The relative displacements between the footing of specimens and concrete blocks, and between the concrete blocks and ground, were captured by potentiometers. Four potentiometers (numbered 18 through 21) were used to capture uplift and slip relative displacement between the footing and concrete block in the north and south side. Another four potentiometers (numbered 22 through 25) were used to captured uplift and slip relative displacement between the concrete block and ground in the north and south side. The positions of these potentiometers are shown in figure 6.

To determine relative rotations of the column for the four segments at the base of the column, eight potentiometers (numbered 1 through 8) were set up in the north and south sides to measure the relative displacement of threaded rods (called curvature rods). The relative rotation calculation is provided in the next chapter. The rods were located 2, 7, 12, and 18 inches above the interface. Detailed installation is illustrated in figure 6. To determine absolute rotations of the column, four inclinometers (numbered 14 through 17) were attached on the east side of the column at 10, 18, 30, and 40 inches above the interface.

Strain gauges were attached to some key shaft and column longitudinal reinforcing bars, and in shaft spirals in the transition area of the column and shaft, as shown in figure 8.

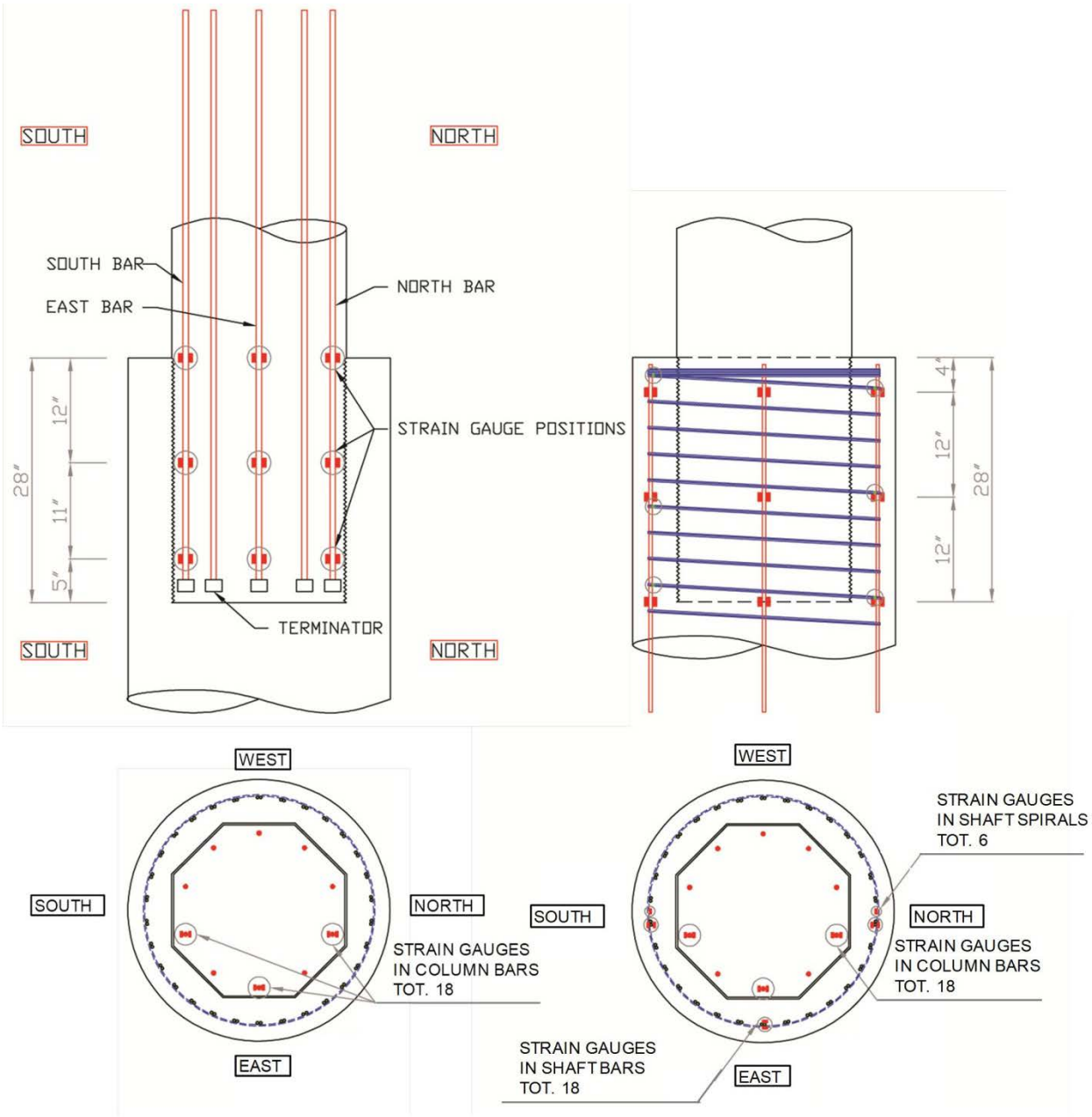

(a) Location of gauges in he column (b) Location of gauges in the shaft

Figure 8. Diagram. Locations of strain gauges.

The gauges on the longitudinal bars and spiral were installed at three levels—top, middle, and bottom of the transition—to capture strain data to help understand the mechanism, force distribution, and behavior of the connection. All strain gauges were supplied by Texas Instruments, type FLA-6-11-5LT, which were used to reduce the effect of temperature variations on the recorded data.

Markers of the research-grade motion capture system were attached to the column and shaft surface in the north, west, and south sides to measure displacement (see figure 6). Another four

markers were attached close to the north curvature rods' positions to compare the data of the string pots and the motion capture system. In specimen DS-2, more markers were set up in the column to determine the rotation of the column to compare with the inclinometer data. As discussed in chapter 5, the research-grade motion capture system and the potentiometers provided consistent results.

Data were recorded with a sampling rate 4Hz using LabVIEW software.

DISPLACEMENT HISTORY

First, the axial load applied in the column was increased to an unfactored dead load value of 159 kips. This axial load was kept constant until the end of testing. Later, the specimen was subjected to displacement controlled cyclic excitation. The displacement history was the same as in previous testing in the Rapid Construction project at the University of Washington. (See references 5, 8, 10, and 14.) This displacement history was a modification of a loading history for precast structural walls recommended in the National Earthquake Hazards Reduction Program (NEHRP).[19]

The displacement history included of sets of four cycles. The peak amplitudes of the cycle in a set were 1.2A, 1.4A, 1.4A, and 0.33A, where A is the maximum peak amplitude in the previous set. The small amplitude cycle was intended to evaluate the residual small-displacement stiffness in the specimen after the maximum peak amplitude cycle of each set. In all cycles, the actuator moved from zero displacement to the peak cycle displacement in 20 seconds. The positive and negative peak displacement were called "peak" and "valley." After peak loading to the south, where the longitudinal column reinforcement in specimen DS-1 fractured and the shaft transverse reinforcement in specimen DS-2 fractured, the testing was stopped. The target displacement history is provided in figure 9 and table 3.

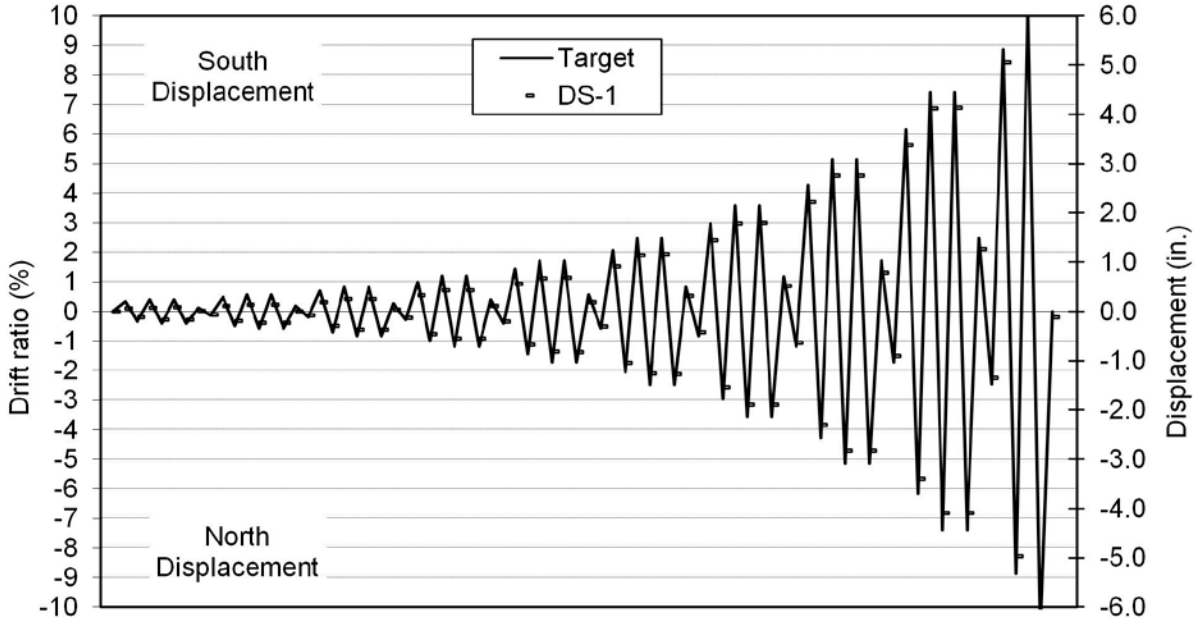

a) Specimen DS-1

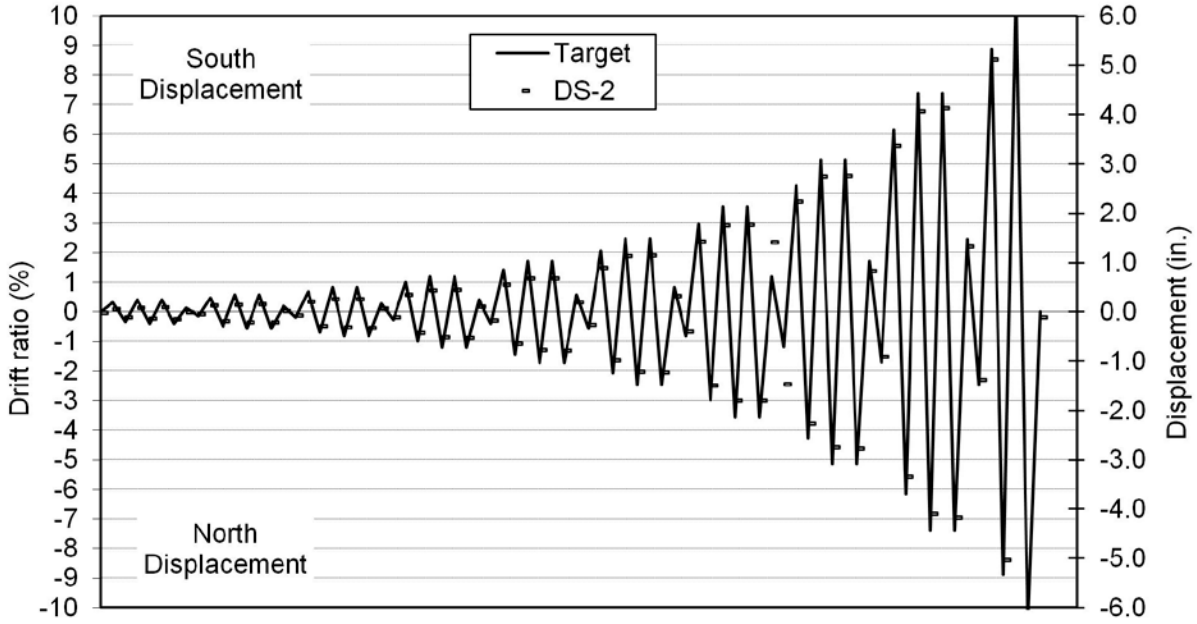

b) Specimen DS-2

Figure 9. Graphs. Lateral loading displacement history.

Table 3. Target displacement history.

Set	Cycle	Drift Ratio (%)	Displ. (in.)	DS-1 Displ. (in.)		DS-2 Displ. (in.)
1	1	±0.33	±0.20	P	0.06	0.05
				V	-0.12	-0.12
	2	±0.40	±0.24	P	0.08	0.09
				V	-0.16	-0.14
	3	±0.40	±0.24	P	0.09	0.10
				V	-0.16	-0.15
	4	±0.13	±0.08	P	0.01	-0.01
				V	-0.06	-0.04
2	1	±0.48	±0.29	P	0.11	0.13
				V	-0.19	-0.18
	2	±0.58	±0.35	P	0.14	0.15
				V	-0.22	-0.21
	3	±0.58	±0.35	P	0.15	0.16
				V	-0.22	-0.21
	4	±0.19	±0.12	P	0.01	0.02
				V	-0.07	-0.07
3	1	±0.69	±0.41	P	0.20	0.21
				V	-0.29	-0.28
	2	±0.83	±0.50	P	0.26	0.25
				V	-0.36	-0.32
	3	±0.83	±0.50	P	0.26	0.26
				V	-0.36	-0.33
	4	±0.28	±0.17	P	0.04	0.06
				V	-0.12	-0.11
4	1	±1.00	±0.60	P	0.34	0.35
				V	-0.45	-0.42
	2	±1.19	±0.72	P	0.43	0.43
				V	-0.55	-0.52
	3	±1.19	±0.72	P	0.44	0.44
				V	-0.55	-0.53
	4	±0.40	±0.24	P	0.12	0.11
				V	-0.20	-0.17
5	1	±1.43	±0.86	P	0.56	0.55
				V	-0.67	-0.64
	2	±1.72	±1.03	P	0.68	0.67
				V	-0.81	-0.77
	3	±1.72	±1.03	P	0.69	0.68
				V	-0.82	-0.78
	4	±0.57	±0.34	P	0.20	0.19
				V	-0.30	-0.27
6	1	±2.06	±1.24	P	0.91	0.90
				V	-1.03	-0.99
	2	±2.48	±1.49	P	1.15	1.13
				V	-1.25	-1.21
	3	±2.48	±1.49	P	1.17	1.15
				V	-1.26	-1.22
	4	±0.83	±0.50	P	0.32	0.32
				V	-0.42	-0.40
7	1	±2.97	±1.78	P	1.45	1.43
				V	-1.53	-1.50
	2	±3.57	±2.14	P	1.80	1.75
				V	-1.88	-1.80
	3	±3.57	±2.14	P	1.81	1.77
				V	-1.89	-1.80
	4	±1.19	±0.71	P	0.53	1.42
				V	-0.63	-1.47
8	1	±4.28	±2.57	P	2.23	2.24
				V	-2.29	-2.27
	2	±5.14	±3.08	P	2.76	2.75
				V	-2.81	-2.75
	3	±5.14	±3.08	P	2.76	2.76
				V	-2.81	-2.77
	4	±1.71	±1.03	P	0.79	0.83
				V	-0.89	-0.90
9	1	±6.16	±3.70	P	3.38	3.38
				V	-3.39	-3.35
	2	±7.40	±4.44	P	4.13	4.07
				V	-4.09	-4.10
	3	±7.40	±4.44	P	4.14	4.13
				V	-4.09	-4.17
	4	±2.47	±1.48	P	1.28	1.33
				V	-1.34	-1.38
10	1	±8.87	±5.32	P	5.06	5.12
				V	-4.96	-5.04
	2	±10.65	±6.39	P	6.30	6.20
				V	-6.01	-6.03
	3	±10.65	±6.39	P		
				V		
	4	±3.55	±2.13	P		
				V		

CHAPTER 4. DAMAGE PROGRESSION

This chapter defines the damage states and describes the damage progression. The progression of damage throughout the test was recorded with detailed sketches, measurements of crack propagation and crack widths, and photos (see appendix C).

DEFINITIONS OF DAMAGE STATES

The performance of each specimen was related to key damage states, as defined in the University of Washington Pacific Earthquake Engineering Research (PEER) Center Structural Performance Database and defined in table 4.[20] These states provided a convenient basis for comparing the progression of damage in the specimens.

Table 4. Damage state descriptions.

Damage Event	Description
First significant horizontal crack	Crack width ≥ 0.02 inches
First significant diagonal crack	Diagonal crack extends 1/4 of column diameter. Crack width ≥ 0.02 inches
First open residual crack	Residual crack width ≥ 0.01 inches
First yield of longitudinal reinforcement	First strain gauge that reaches yield strain (0.00212)
First yield of transverse reinforcement	First strain gauge that reaches yield strain (0.00212)
First spalling in footing	Observed spalling on surface
First spalling in column	Observed flaking, minor spalling
Significant spalling in column	Spalled height ≥ 1/4 of column diameter
Fully spalled	Spalling height no longer increases with increasing deformation
Exposure of longitudinal reinforcement	First observation of column longitudinal reinforcement.
Buckling of longitudinal reinforcement	First observation of column longitudinal bar buckling.
Large cracks in concrete core	Crack width ≥ 0.08 inches
Fracture of transverse reinforcement	Observation or sound
Fracture of longitudinal reinforcement	Observation or sound
Loss of axial capacity	Instability of member

DAMAGE PROGRESSION

On the day before testing, pre-test cycles were performed to verify that the instruments were working correctly. The columns were loaded axially up to 90 kips and were cycled at +/- 0.035 percent lateral drift. No cracks were detected.

On the day of testing, each column was loaded vertically to 159 kips, which corresponded to the scaled-down, unfactored dead load on the bridge column. That vertical load was kept constant throughout the test.

The lateral excitation history consisted of sets of four cycles and was controlled in terms of lateral displacement. The amplitudes of the cycles were described in chapter 3. The positive loading direction (with a maximum at "peak") was defined by the actuator being in tension and displacements to the south. Each new set of cycles started in the positive direction. In the negative direction, the extreme displacement is referred to as the "valley."

The continuity of the loading differed among the cycles of each set. In the first two cycles of each set, cycling was interrupted at extreme displacements ("peak" and "valley") to allow inspection of cracks. At zero displacement, between cycles, the biggest residual crack width was measured. In the second two cycles, the loading was continuous with no interruptions and no cracks were inspected or marked.

Specimens DS-1 and DS-2 were each subjected to a total of 38 cycles (up to cycle 10-2). The results are shown in table 5 and figure 10, where they are compared with the results of spread footing specimens SF-1 and SF-2 of Haraldsson and SF-3 of Janes.[10,14] It should be noted that, for many damage states, close correlation between the drilled shaft and spread footing specimens should not be expected because the two systems behave rather differently. For example, in the drilled shafts, the drift ratio was computed by dividing the total displacement at the load point by the height (60 inches) of the column alone, regardless of any lateral deformation over the height of the shaft. The same definition of drift ratio was used in the spread footing connections, but in them, there was no lateral deformation of the footing.

The details of the damage progression for specimens DS-1 and DS-2 are also shown in figure 10. In the initial cycles, up to about 0.7 percent drift ratio, the cracks in both specimens were fine and closed almost completely at zero displacement between cycles. At about 0.7 percent drift ratio, the longitudinal steel in the column yielded and the first significant horizontal cracks appeared. Those cracks did not close completely when the load dropped to zero.

After the longitudinal column reinforcement yielded, the behaviors of specimens DS-1 and DS-2 differed significantly. In DS-1, the damage was concentrated in the column, and the specimen eventually failed by fracture of the longitudinal steel in the plastic hinge region of the column, in what might be thought of as a typical column failure. The longitudinal bars buckled, causing a kink in the spiral steel, which initiated its fracture. After the spiral fractured, the longitudinal bars straightened and re-buckled with each load cycle and eventually fractured due to the low-cycle fatigue caused by the alternate bending and straightening. The longitudinal steel in the shaft never yielded, and the transverse steel in the shaft yielded but never fractured. This behavior, characterized by concentration of damage in the column, was similar to that of specimens SF-1 and SF-2.

Table 5. Damage milestones for all five specimens.

Damage Event	Specimen DS-1						Specimen DS-2						Specimen SF-1			Specimen SF-2			Specimen SF-3		
	Shaft			Column			Shaft			Column											
	Set	Cycle	Drift (%)	Set	Cycle	Drift (%)	Set	Cycle	Drift (%)	Set	Cycle	Drift (%)	Set	Cycle	Drift (%)	Set	Cycle	Drift (%)	Set	Cycle	Drift (%)
First significant horizontal crack	4	2	0.72	4	1	0.56	4	2	0.72	4	2	0.72	4	1	0.69	3	2	0.56	3	1	0.49
First significant diagonal crack	6	1	1.52/ -1.72	5	2	1.13/ -1.35	6	1	1.49/ -1.65	6	1	1.49/ -1.65	6	1	1.68/ -1.80	6	1	1.74	6	1	1.71
First open residual crack	5	3	1.16/ -1.37	5	2	1.13/ -1.35	6	2	1.89/ -2.02	6	2	1.89/ -2.02	6	1	1.68/ -1.80	4	3	0.88/ -0.95	5	1	1.13/ -1.23
First yield of longitudinal reinforcement	N/A	N/A	N/A	4	2	0.72	N/A	N/A	N/A	4	1	0.58	3	1	-0.55	3	2	0.47	3	1	-0.51
First yield of transverse reinforcement	8	1	3.71/ -3.82	N/A	N/A	N/A	6	3	1.92/ -2.03	N/A	N/A	N/A	9	1	0.33	9	2	-5.41	8	2	-4.77
First spalling in footing	6	1	1.52/ -1.72	N/A	N/A	N/A	7	1	2.38/ -2.50	N/A	N/A	N/A	N/A	N/A	N/A	N/A	N/A	N/A	9	2	7.11/ -6.92
First spalling in column	N/A	N/A	N/A	5	2	1.13/ -1.35	N/A	N/A	N/A	N/A	N/A	N/A	5	1	1.07/ -1.21	5	1	1.10/ -1.19	5	3	1.41/ -1.49
Significant spalling in column	N/A	N/A	N/A	7	2	3.00/ -3.14	N/A	N/A	N/A	N/A	N/A	N/A	6	2	-2.25	7	1	2.64	6	2	2.13/ -2.21
Full spalling in column	N/A	N/A	N/A	9	2	6.88/ -6.82	N/A	N/A	N/A	N/A	N/A	N/A	9	3	7.08/ -6.90	8	1	3.98	9	1	5.84/ -5.76
Exposure of longitudinal reinforcement	N/A	N/A	N/A	9	3	6.90/ -6.81	9	3	6.89/ -6.95	N/A	N/A	N/A	9	1	-5.68	9	2	-6.85	9	3	7.15/ -6.93
Buckling of longitudinal reinforcement	N/A	N/A	N/A	9	3	6.90/ -6.81	N/A	N/A	N/A	N/A	N/A	N/A	9	2	7.09/ -6.88	9	3	7.19/ -6.88	9	3	7.15/ -6.93
Large cracks in concrete core	N/A	N/A	N/A	7	2	3.00/ -3.14	7	1	2.38/ -2.50	6	1	1.49/ -1.65	10	2	10.61	10	2	-9.95	10	2	10.58/ -9.97
Fracture of transverse reinforcement	N/A	N/A	N/A	10	1	8.43	8	2	4.59	N/A	N/A	N/A	9	2	-6.88	10	1	-8.29	10	1	8.72
Fracture of longitudinal reinforcement	N/A	N/A	N/A	10	2	10.49	N/A	N/A	N/A	N/A	N/A	N/A	10	2	10.61	10	2	10.65	N/A	N/A	N/A
Loss of axial capacity	N/A	N/A	N/A	N/A	N/A	N/A	N/A	N/A	N/A	N/A	N/A	N/A	N/A	N/A	N/A	N/A	N/A	N/A	10	3	10.7

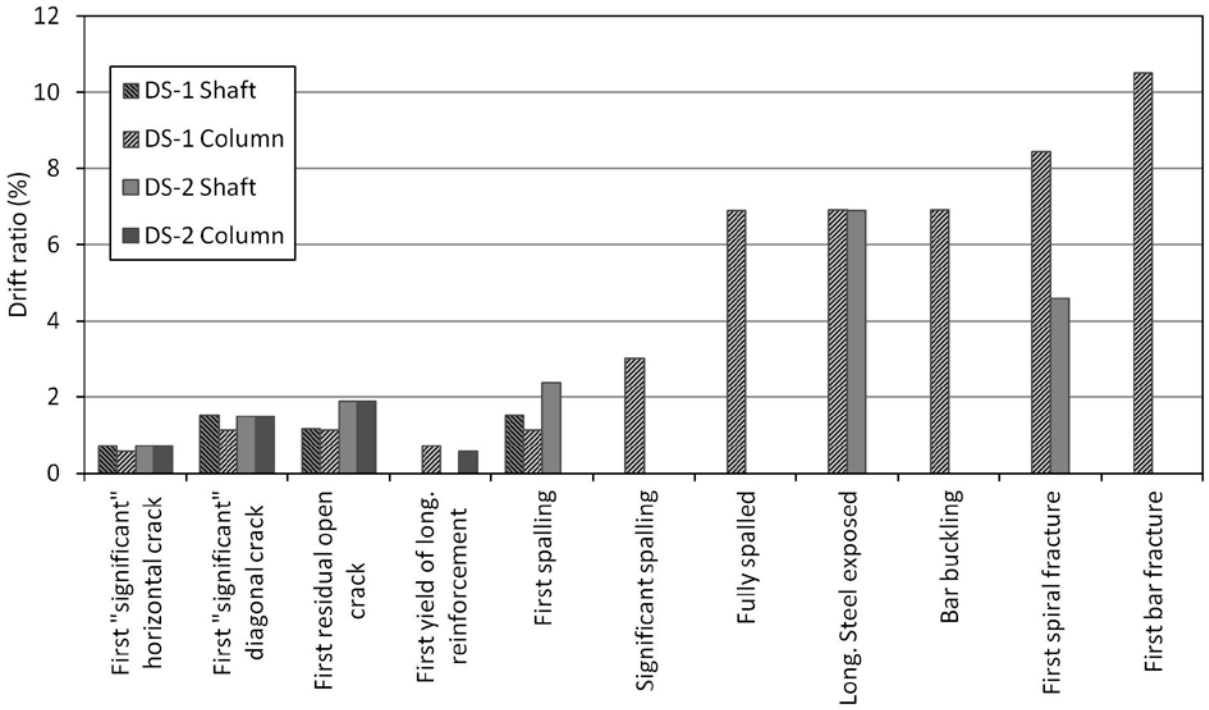

Figure 10. Chart. Comparison of specimens' drift ratios for the major damage states.

In specimen DS-2, the amount of spiral steel in the shaft was only half that in specimen DS-1. It is therefore not surprising that the transverse reinforcement in the shaft yielded earlier in DS-2 and subsequently fractured. The behavior of the specimen was characterized by very large cracks opening in the shaft, which suffered extensive shear deformations as a result. Failure was initiated by fracture of the spiral steel in the shaft, starting at the top and progressing downwards. The damage to the shaft caused the load to drop even though the drift was increasing. The longitudinal bars in the column did not buckle, and by observation, it was known that the spirals in the column never fractured.

In the drilled shaft specimens, shear sliding between the precast column and cast-in-place shaft was an important behavioral mechanism. No instrumental measurements could be made, so visual observations provided the only available evidence, and those observations could be made primarily after the test was complete. Figure 11 shows specimen DS-1 after the test. The damage to the shaft exists mainly in the small region of top cover concrete above the ends of the vertical bars. In the remainder of the shaft, the column is still held firmly by friction. Figure 12 shows specimen DS-2 after testing. There, the shaft has been pried open by the lateral movements of the column so the column could be lifted freely out of the shaft with no frictional resistance. The prying action on the shaft yielded the transverse steel in it and led to the large deformations.

Figure 11. Photo. Specimen DS-1 after testing.

Figure 12. Photo. Specimen DS-2 after testing.

CHAPTER 5. MEASURED RESPONSE

This chapter reports the measured responses of specimens DS-1 and DS-2 during testing.

MOMENT-DRIFT RESPONSE

The moment-drift response is similar to the load-displacement response, but it differs slightly, because the moment includes components from both the vertical and lateral loads, whereas the load-displacement response includes only the horizontal load.

The moment at the base of column is given by the equation in figure 13.

$$M_c = h_1.V - F_{fric}.h_2 + (\Delta_2 - \Delta_3).P$$

Figure 13. Equation. Moment at the base of the column.

In figure 13:

M_c = the column moment at the base.

h_1 = height from the column-shaft interface to the line of action of the lateral load.

h_2 = is the height from the interface to the top of column where the axial load, P, is applied by the Baldwin Universal Testing Machine.

V = applied lateral load.

F_{fric} = the friction force between the bearing and the sliding channel, and the greased steel-to-steel spherical element on bearing.

Δ_1 = the lateral displacement at the location of the lateral load.

Δ_2 = the lateral displacement at the top of column.

Δ_3 = the lateral displacement at the top of transition, was taken approximately as lateral displacement at the first curvature rod (2 inches above the top of transition).

These parameters are illustrated in figure 14.

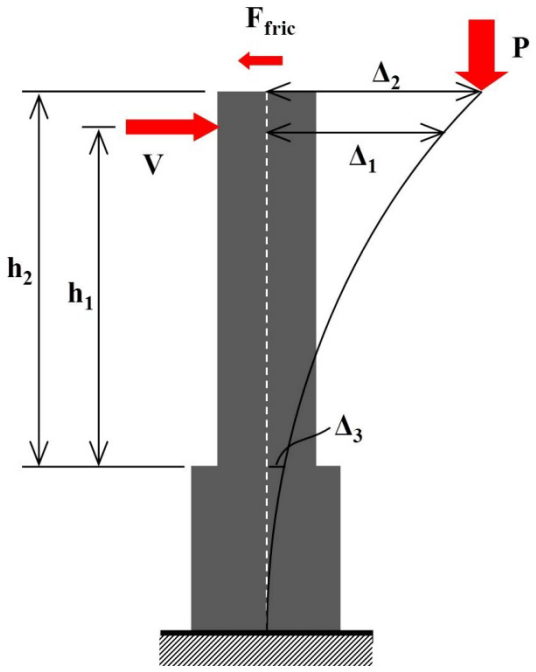

Figure 14. Diagram. Displacements and forces on test specimen.

In the absence of a measured value for Δ_2, it was approximated by assuming the column rotated as a rigid body about its base, in which case the equations in figure 15 and 16 hold true.

$$(\Delta_2 - \Delta_3) \approx (\Delta_1 - \Delta_3).\frac{h_2}{h_1}$$

Figure 15. Equation. Determination of axial load lateral displacement.

$$M_c = h_1.V - F_{fric}.h_2 + (\Delta_1 - \Delta_3).\frac{h_2}{h_1}.P$$

Figure 16. Equation. Moment at the base of the column.

It should be noted that the vertical load, P, contributed about one-third of the total moment at the maximum drift, and less than that at smaller drifts. Thus, any relative error in the approximation of Δ_2 creates a smaller relative error in the moment calculation.

Figure 17 shows the moment vs. drift ratio response of the test specimens DS-1 and DS-2. Because the columns used in these specimens were nominally identical to those used in spread footing specimens SF-1 and SF-2 by Haraldsson and SF-3 by Janes, results from those tests are shown for comparison.[10,14] The measured response of specimen DS-1 was similar to those of specimens SF-1 and SF-2. In all three cases, failure occurred by plastic hinging in the column, while the connection region in the foundation remained largely undamaged. However, in specimens DS-2 and SF-3, failure occurred in the connection region after some damage had first occurred in the column. This difference is apparent in the figures for those specimens, in which the strength decays with increasing drift more rapidly than is the case in SF-1, SF-2, and DS-1.

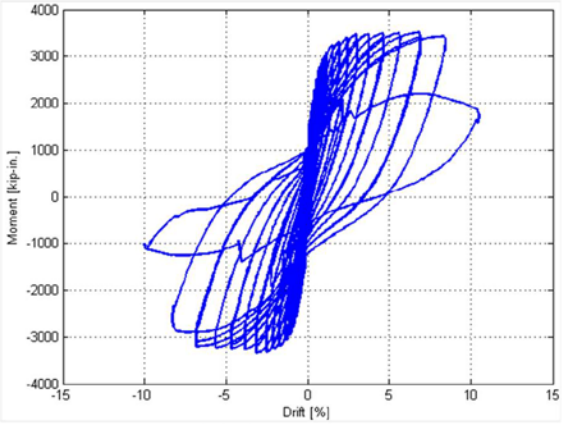

a). Specimen DS-1 moment-drift response

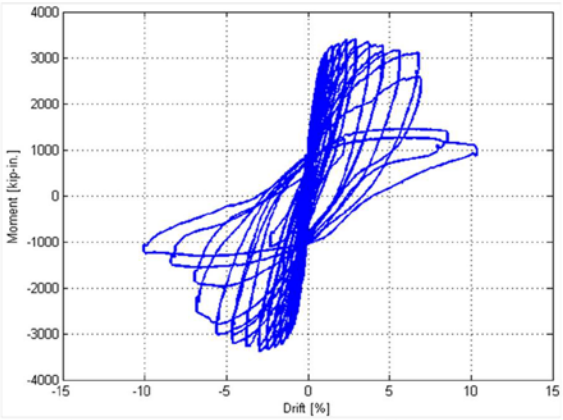

b). Specimen DS-2 moment-drift response

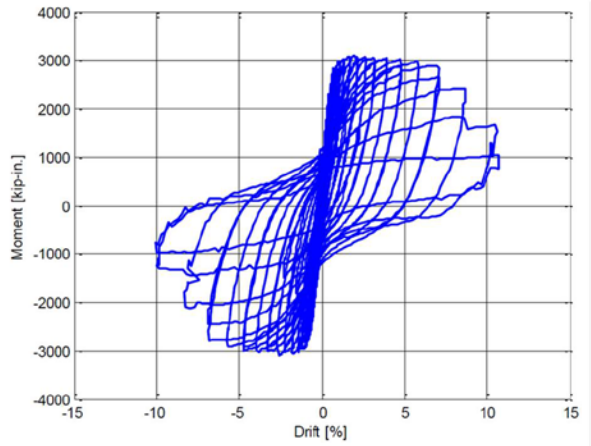

c). Specimen SF-1 moment-drift response

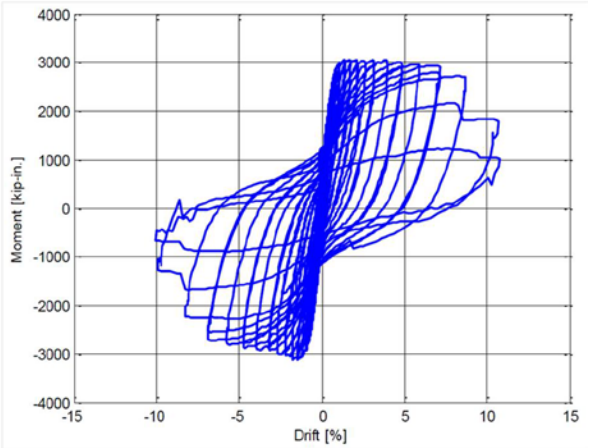

d). Specimen SF-2 moment-drift response

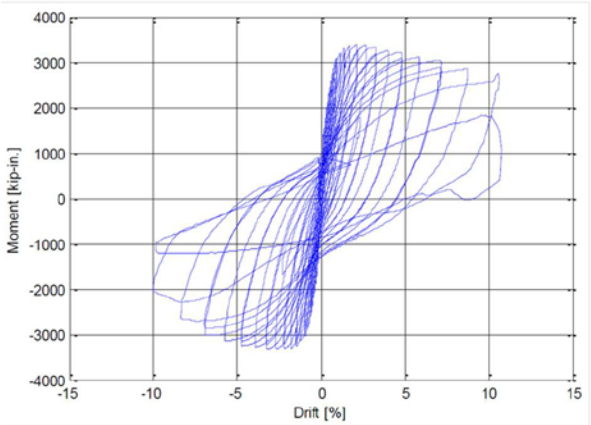

e). Specimen SF-3 moment-drift response

Figure 17. Graphs. Moment vs. drift ratio response.

In all cases, the peak moment occurred at about 2.5 to 3 percent drift ratio, and the moment first dropped below 80 percent of the peak value at about 8 percent drift, except in DS-2 where it occurred at about 7 percent drift; the response was very ductile. The similarity between the peak strengths in specimens SF-1, SF-2, and DS-1 was expected because the columns were nominally identical and the specimen strength was controlled by the column response. (The primary difference was the concrete strengths.)

As shown in table 6, the maximum moments at the interface were approximately 3,400 kip-in. in both specimens DS-1 and DS-2. The stiffness of the columns was measured at the force corresponding to the first yield of column reinforcement. It shows that DS-1 had nearly the same stiffness as DS-2.

Table 6. Moment and drift ratio at maximum and 80 percent of maximum resistance.

Points of Interest	DS-1		DS-2	
	North Direction	South Direction	North Direction	South Direction
Secant Stiffness at Initial Yield Moment (kip/in.)	109	126	101	122
Maximum Column Interface Moment (kip-in.)	-3,290	3,476	-3373	3,393
Drift Ratio at Maximum Column Interface Moment (%)	-3.09	6.83	-2.96	2.90
80% of Maximum Column Interface Moment (kip-in.)	-2,657	2,811	-2,293	2,337
Drift Ratio at 80% of Maximum Interface Column Moment (%)	-8.27	8.15	-5.95	6.84

The columns were also stiffer in the south direction of loading, which was the direction in which they were first loaded. This behavior was observed for both specimens. The exact reason for this behavior is unknown, but it appears to be related to the level of cracking, which is likely to have been larger in the direction of second loading.

Failure is commonly defined at the point where the maximum moment is 80 percent of peak moment. In specimen DS-1, it occurred after 8.0 percent drift ratio and corresponded to the onset of buckling of the column longitudinal reinforcement. However, in specimen DS-2, it occurred at about 6.0 percent drift, when vertical and diagonal cracks had propagated throughout the transition region, and the spirals were at incipient fracture.

The lateral load, V, used in the equations in figures 14 through 16, was corrected for friction in the sliding bearing using the recommendation proposed by Brown.[21] The test setup in the Baldwin Universal Testing Machine created frictional resistance in the system by two

mechanisms: rotation between the greased steel-to-steel spherical element in the swivel head bearing and sliding between the bearing's top flat plate and the channel attached to the Baldwin head. The friction component in the channel was minimized by placing a silicon-greased Teflon sheet on the bearing where it slid against smooth stainless steel plates in the channel. This correction was done previously in research on accelerated bridge construction (ABC) at the University of Washington.[5,21] The rotational element in the bearing was also greased, but because it consists of two mating steel surfaces, the friction there is necessarily higher.

The correction model consists of a bilinear spring with a spring stiffness, k, of 60 kips/in., and has a maximum friction force, $F_{max\ friction}$, of $\mu_{eff}.P$, where μ_{eff} is a calculated coefficient of friction and was taken as 0.016, and P is the target axial load (160 kips).[21] Therefore, the estimated maximum resistance of approximately 2.56 kips. This is approximately 5 percent of the maximum applied lateral load in both tests.

EFFECTIVE FORCE

The effective force acting on the specimens was calculated by dividing the moment at the interface by the height from the interface to the line of action of the lateral load. The equation in figure 16 is divided by h_1 to obtain the equation in figure 18.

$$F_{eff} = V - F_{fric}.\frac{h_2}{h_1} + (\Delta_1 - \Delta_3).\frac{h_2}{h_1^2}.P$$

Figure 18. Equation. Effective lateral force.

In figure 19, the effective force is plotted against displacement for both specimens. The shapes of the curves are identical to the moment-drift responses, but they are expressed in terms of the effective force and displacement.

Table 7 summarizes the values of 100 percent and 80 percent of the maximum effective force (MEF) and the corresponding displacements.

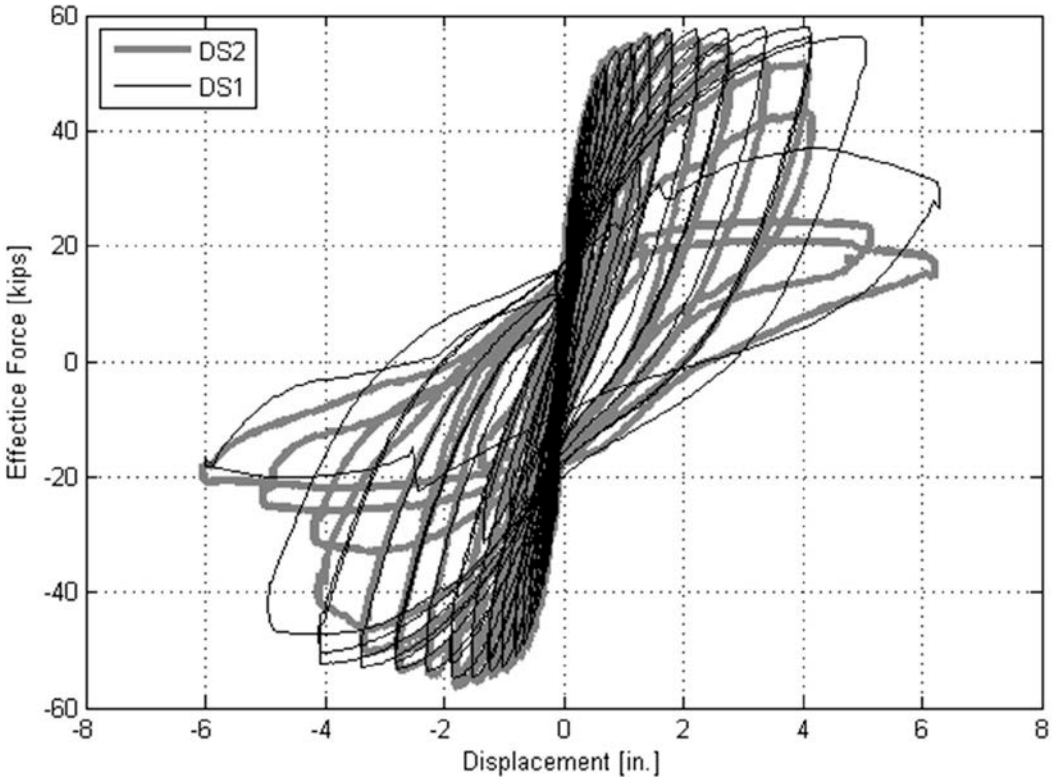

Figure 19. Graph. Effective force-displacement response.

Table 7. Effective force and displacement at maximum and 80 percent maximum of resistance.

Points of Interest	DS-1		DS-2	
	North Direction	South Direction	North Direction	South Direction
Maximum Effective Force (kips)	-54.8	57.9	-56.21	56.5
MEF Displacement (in.)	-1.85	4.10	-1.80	1.74
80% of Maximum Effective Force (kips)	-43.8	46.3	-45.0	45.2
80% of MEF Displacement (in.)	-4.96	4.89	-3.57	4.02

CURVATURE

Average curvatures were computed from the measured displacement data at selected locations along the columns and shafts. They are reported here to show the distribution of bending deformations and to evaluate the contribution of bending to the total displacement.

In the columns, the curvatures were computed from local rotations, and near the bottom of the column, these were established by measuring the differential displacement on either side of the column of rods that were embedded horizontally into the concrete (see figure 20). These were

referred to as “curvature rods.” Higher up the column, where no curvature rods existed, the rotations were obtained from inclinometers attached to the column face.

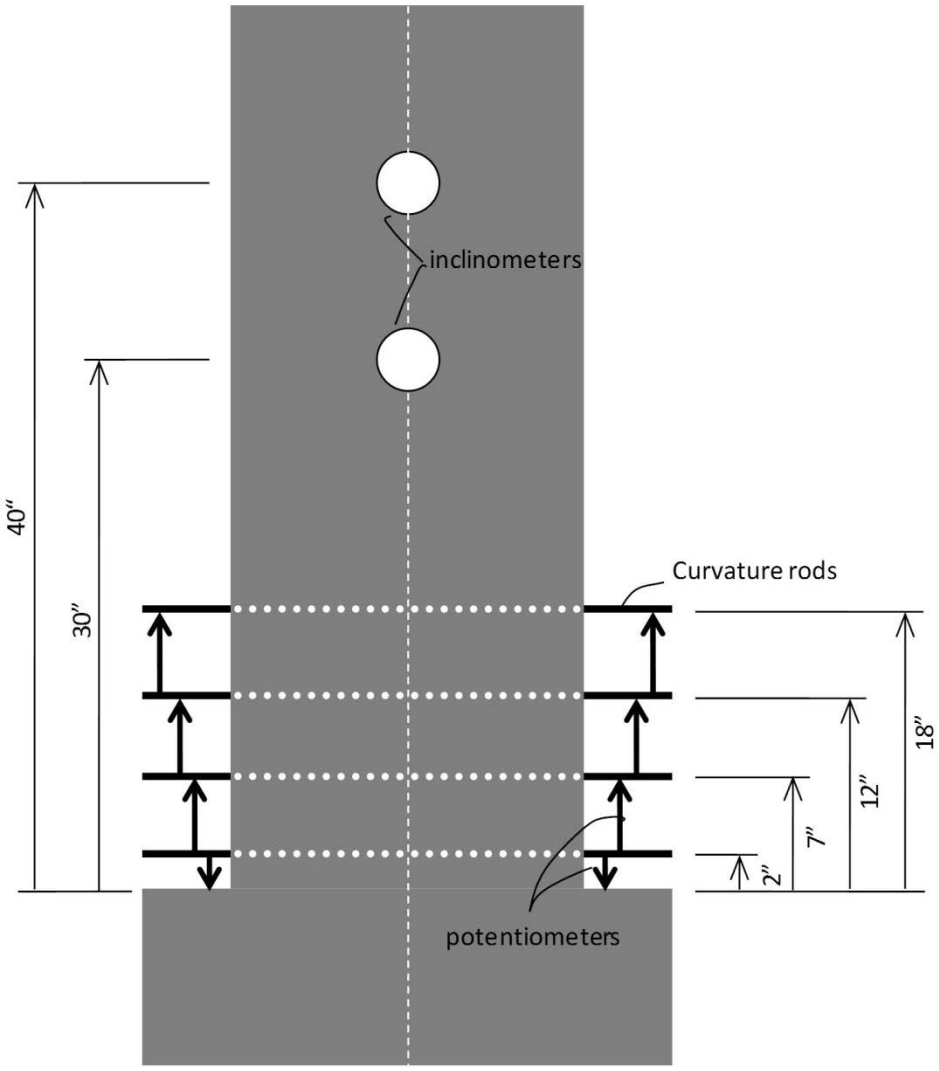

Figure 20. Diagram. Detailed curvature rods setup.

These methods were also used by Haraldsson and Janes.[10,14] Curvature rods were embedded in the column about 2, 7, 12, and 18 inches above the interface. The average curvatures between rods were plotted at the mid-point of those segments. The curvatures were calculated using the equation shown in figure 21.

$$\varphi_{\mathrm{i}} = \left(\frac{\delta_{\mathrm{i,N}} - \delta_{\mathrm{i,S}}}{L_i}\right) / H_i$$

Figure 21. Equation. Calculating curvature.

In figure 21:

φ_i = the calculated average curvature.

$\delta_{i,N}$ and $\delta_{i,S}$ = the relative displacement between rods on the north side and south side at particular height above the interface.

L_i = the horizontal length between north and south potentiometers.

H_i = the height of each segment.

Above the rod position, the column average curvatures were obtained by the column average rotation difference between two inclinometers.

The shaft average curvatures were determined from the shaft rotation at selected locations (measured by the motion capture system). At each level, one marker was attached on each of the north, south, and west sides of the shaft. The rotations of the shaft were taken as the rotation of the plane defined by these three points.

Figure 22 shows the average column curvature versus height for selected drift ratios. The height was relative to the column-shaft interface.

The curvatures were plotted up to 6.8 percent drift. The curvature data at higher drift were not reliable because the spalling of concrete in the column in specimen DS-1 and in the top surface of the shaft in specimen DS-2 affected the potentiometers. The column curvature distribution was similar in both specimens until 3.0 percent drift. These curvatures were similar because, up to that drift, the majority of the displacement was in both cases provided by the column. The deformation was distributed over the column height, with the largest values at the bottom. The latter were caused by the formation of a significant crack at the column-shaft interface, which dominated the displacement measured by the potentiometers. The segment length at the bottom was also short (2 inches), and the average rotation measured included column rotation and bending rotation; thus, the computed curvature was relatively high. The concept of curvature is based on the existence of a continuous deformation field. In a cracked, discontinuous, medium, such as the concrete in the columns and shafts, the calculated curvature is not unique and depends on both the segment size and the locations of the cracks relative to the segment boundaries. Nonetheless, the distribution of computed curvature gives an overall sense of the distribution of bending deformations.

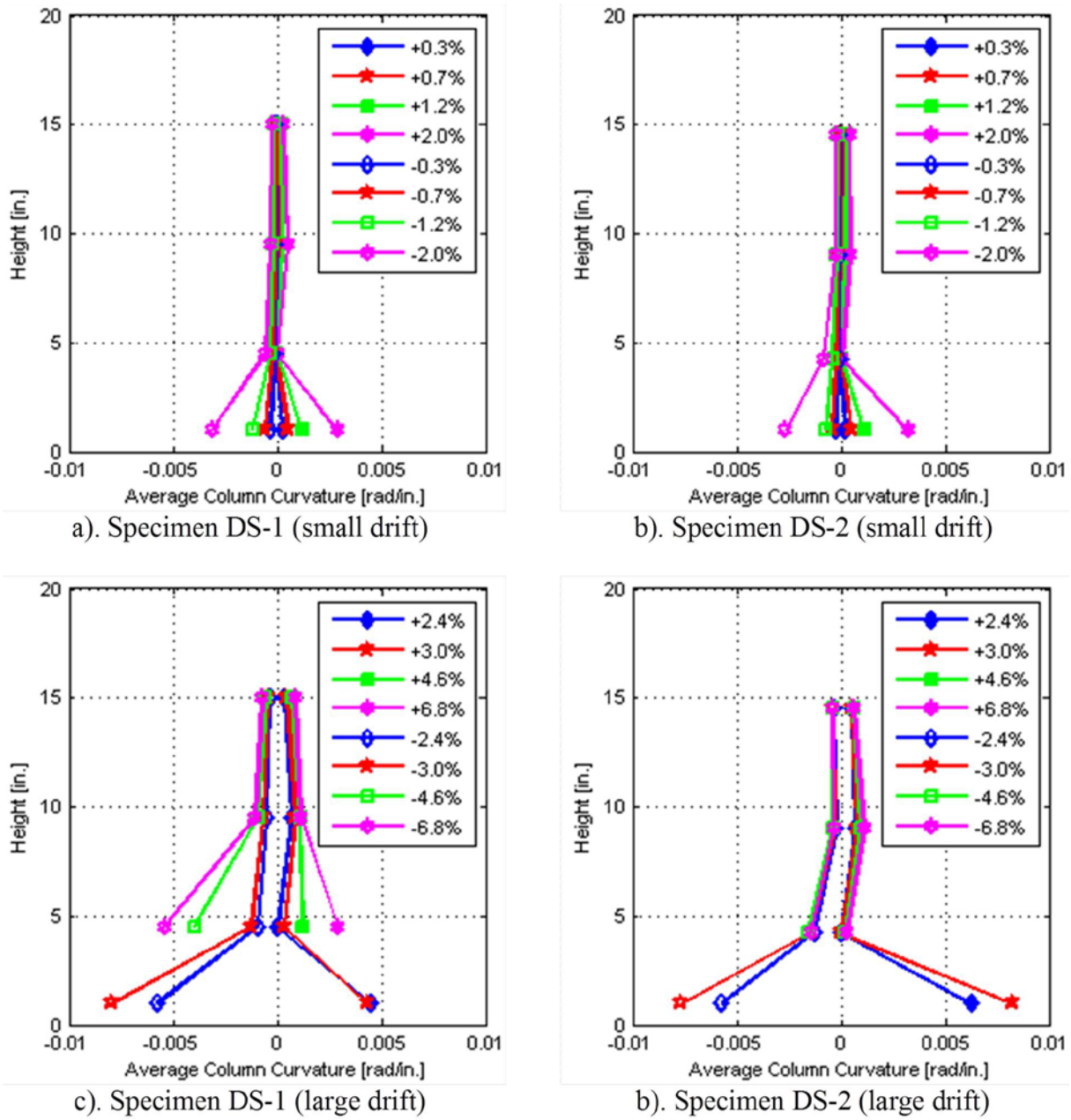

a). Specimen DS-1 (small drift)

b). Specimen DS-2 (small drift)

c). Specimen DS-1 (large drift)

b). Specimen DS-2 (large drift)

Figure 22. Graphs. Average column curvature (specimen DS-1 and DS-2).

At higher drift ratios (after 3.0 percent drift), because of the onset of spalling at the top of transition, the strain values at the bottom segment measured by potentiometers were unreliable; they are plotted in the figures. The column curvature distribution differed between the two specimens. In DS-1, the average curvature at 5 inches above the interface increased rapidly while it did not change in DS-2. That was consistent with the damage progression in two tests when spalling occurred in DS-1 and did not happened in DS-2. The bond stress between the column and shaft started degrading, and the shaft in specimen DS-2 started to deform significantly. Thus, at any given drift, the column curvature was smaller in specimen DS-2 than in specimen DS-1.

In DS-2, a method using three “Optotrak” markers was used to measure rotation in the column to compare with the result of using curvature rods. The column average curvature versus height for selected drift ratios are provided in figure 23. The results of column curvature distribution were quite similar by using Optotrak markers and curvature rods. The different curvatures at the bottom segment were unknown, but these values were unreliable, as explained previously.

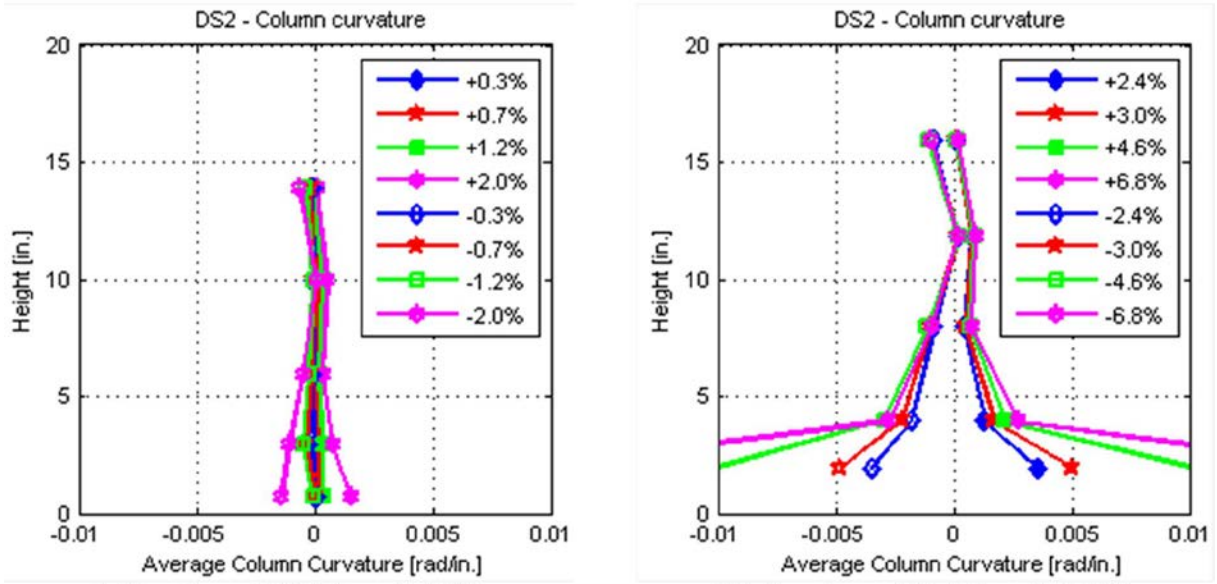

a). Specimen DS-2 (small drift)

b). Specimen DS-2 (small drift)

Figure 23. Graphs. Average column curvature (measured by Optotrak) in specimen DS-2.

The average shaft curvature versus height for selected drift ratios is shown in figure 24. The curvatures in the shafts were also distributed non-uniformly, with the largest values at the base. Such distribution reflects the existence of a flexural crack at the base. Each of the peaks of curvature corresponds to a horizontal crack position. Note that the scales on the column and shaft plots are different, and that the shaft curvatures were smaller by about an order of magnitude than the column curvatures.

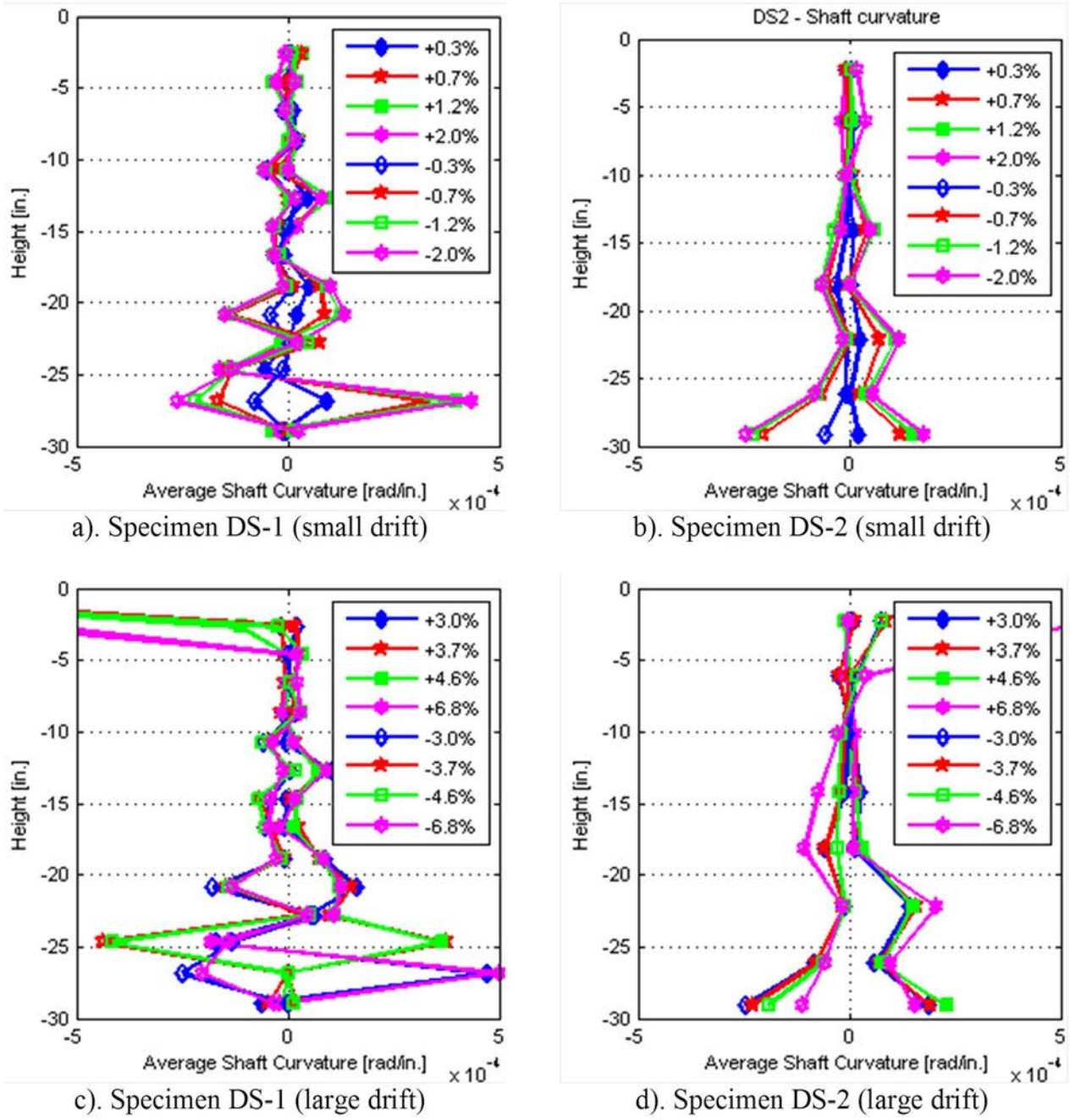

a). Specimen DS-1 (small drift)

b). Specimen DS-2 (small drift)

c). Specimen DS-1 (large drift)

d). Specimen DS-2 (large drift)

Figure 24. Graphs. Average shaft curvature for specimens DS-1 and DS-2.

DISPLACEMENT

In the test specimens, the horizontal displacement at the top of the column depended on the deformations of the individual elements. To simplify discussion, those deformations are broken down into the following components, which are illustrated in figure 25.

1. *Shaft bending deformations.* These are the curvatures of the shaft, and they depend on the elongation of one vertical face and the shortening of the opposite one. Curvature was

measured by the three Optotrak markers attached to the shaft at the same level, using the motion capture system. At each level, one Optotrak marker was attached on each of the north, south, and west sides of the shaft. The rotations of the shaft were taken as the rotation of the plane defined by these three points. Then, the average curvature of segment was calculated by dividing the difference of rotation at the adjacent level to the segment's height.

2. *Shaft shear deformations*. These deformations consist of pure shear deformations of the shaft. They were obtained by subtracting the shaft bending displacements from the total horizontal displacements. The total displacements were obtained from the horizontal displacements measured by the motion capture system (and verified by the string potentiometers). The bending displacements were obtained by integrating the rotations obtained from the shaft bending deformations.
3. *Column end rotations.* The column can rotate as a rigid body, due to damage in the transition region of the shaft. These rotations were obtained from the bottom inclinometer attached to the column, and from the group of three Optotrak markers attached to the bottom of the column (2 inches above the interface).
4. *Column bending deformations.* These deformations consist of the curvatures of the column. Rotations were measured at discrete locations up the column, and the average curvature was computed from the difference between rotations at adjacent locations. The rotations were obtained using inclinometers, curvature rod instruments, and Optotrak data.
5. *Column shear deformations.* These consist of the pure shear deformations of the column. They were very small in both cases, and they were estimated by subtracting the total displacement to the displacement of components 1, 2, 3, and 4. This value would include error in this computation.

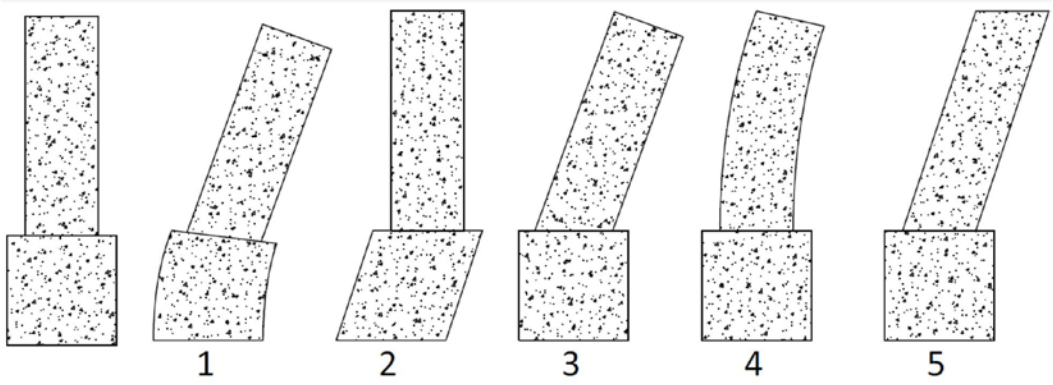

Figure 25. Illustration. Displacement types.

The displacements were calculated at the top of the column (60 inches above the interface). The shaft bending displacements were calculated by numerically integrating the shaft curvature over the height of the shaft. The shaft shear displacements were calculated by subtracting the shaft bending displacements at the top of the shaft from the total shaft displacement (using Optotrak measurements). The displacements due to column end rotation were calculated as the product of column height and the difference between the rotation of the column at 10 inches above the

interface (measured by an inclinometer) and the rotation of shaft at the interface (measured by the Optotrak). The displacements due to column bending were calculated by numerically integrating of the column curvature. The column shear displacement and error of the instruments were calculated by subtracting the displacements due to shaft bending, shaft shear, column end rotation, and column bending from the displacement at the top of the column (as measured by a string potentiometer).

Vertical displacements were measured only by the Optotrak system. No values are presented here.

The method of measuring rotation of specimens using groups of three Optotrak markers was compared with the results obtained using the inclinometers to show the accuracy of this method. The comparison is shown in figures 26 and 27 for the results measured in specimen DS-2. The comparison shows that the Optotrak method and the inclinometers provided similar results.

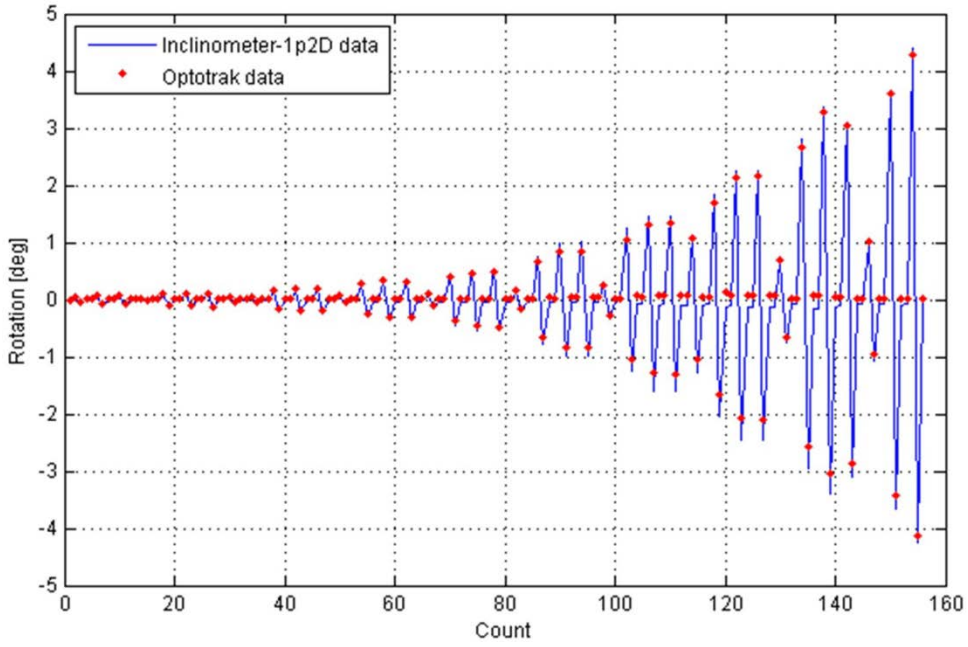

Figure 26. Graph. Rotation comparison at 10 inches above the interface position (specimen DS-2).

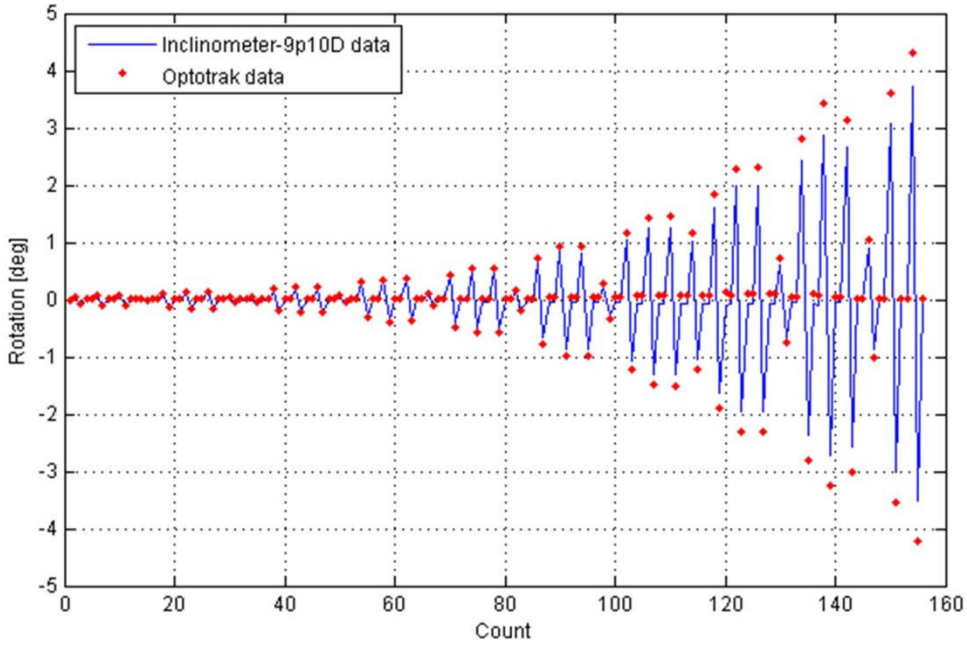

Figure 27. Graph. Rotation comparison at 18 inches above the interface position (specimen DS-2).

The displacement profiles of the shaft and column are plotted for specimens DS-1 and DS-2 in figure 28 and figure 29, respectively. The vertical axis represents the distance above the base of the shaft, while the horizontal axis is the displacement in inches. Note that the shaft was 30 inches high, and the height of the column, measured from the top of the shaft to the loading point, was 60 inches.

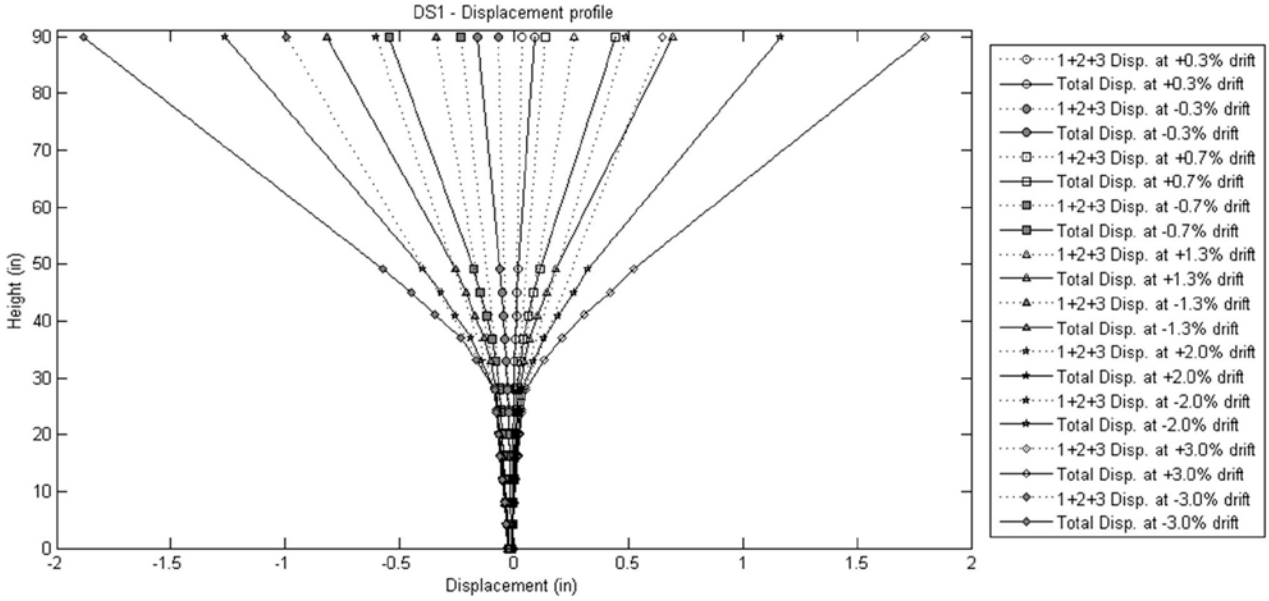

Figure 28. Graph. Specimen DS-1 displacement profile.

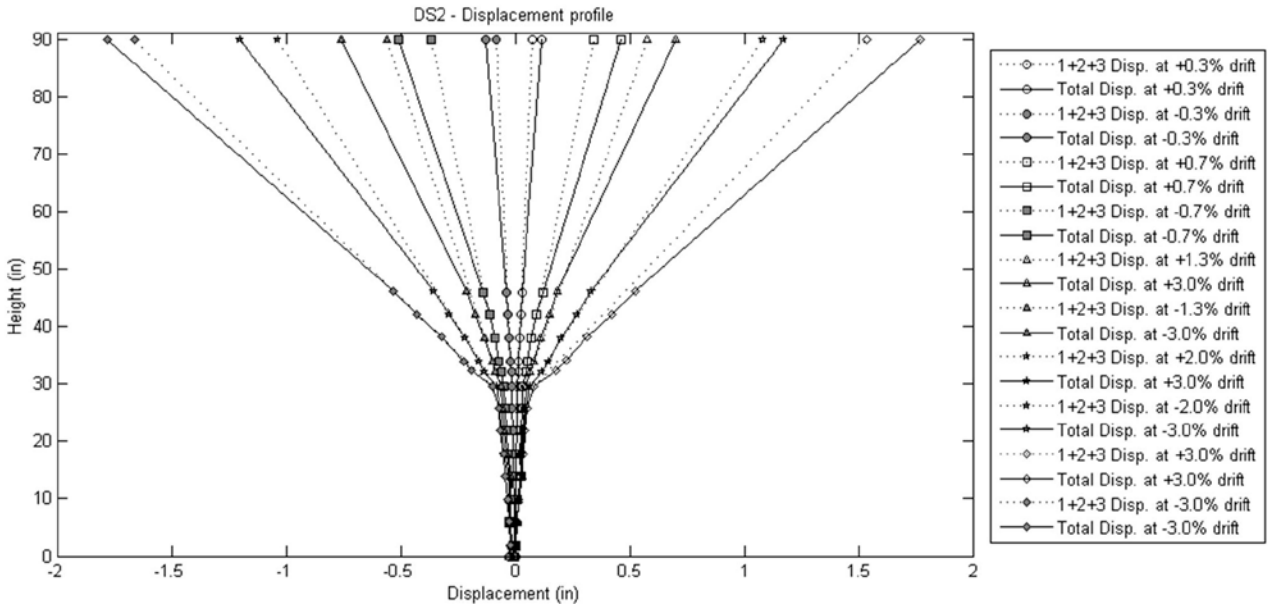

Figure 29. Graph. Specimen DS-2 displacement profile.

Profiles are given for the peak displacement in each cycle set, up to 3.0 percent drift. Separate curves are given for the positive and negative directions. For each load level, two curves are presented. The solid line represents the total displacement, while the dashed line represents the sum of the displacements due to components 1, 2, and 3 (shaft bending, shaft shear, and column base rotation). Components 1 and 2 may be thought of as shaft contributions to the overall displacement. Component 3 may be thought of as a column boundary condition contribution, which is nearly zero in Haraldsson's column-spread footing socket connection.[(10)] The differences between the dashed and solid lines for any load level, therefore, represent the displacement due to column bending and shear, or the column contributions to the total displacement. In all cases, the column shear component small compared with the column-bending component.

Up to 0.7 percent drift, the displacement profiles of specimens DS-1 and DS-2 were similar. The angle of dotted lines at the interface position corresponded to the appearance of column base rotation. Thus, the column base rotations were nearly zero because there was no angle at the interface position in the dotted lines.

However, after 0.7 percent drift, the behaviors of specimens DS-1 and DS-2 were different. Overall, the majority of the displacement in specimen DS-1 arose from column deformations, because a plastic hinge started to form in the column. By contrast, in specimen DS-2 the column deformations were small, and the column base rotations deformations dominated the behavior of the specimen.

The details of the response were as follows. In specimen DS-1, the column bending deformation kept increasing with each cycle up to 3.0 percent drift. This was suggested by the rapid increasing of the distance between solid lines and dotted lines at the top position at the same drift. On the other hand, in specimen DS-2, the column bending deformation decreased after 0.7 percent drift and was very small at 3.0 percent drift. The majority of the total displacement was attributable to column base rotation, which was 0.012 rad (1.2 percent drift) in DS-1 and 0.007

rad (0.7 percent drift) in DS-2. However, in DS-2, the percentage of the column base rotation contribution to total deformation was higher than in DS-1.

The contributions of the various displacement types are shown in figures 30 and 31. In specimen DS-2, after cycles to 7 percent drift, large vertical cracks appeared in the shaft. Thus, the data obtained from the Optotrak marker attached in the shaft were not reliable for calculating the curvature of the shaft. Therefore, the displacement of the shaft bending, column shear, and error were not reliable after 7 percent drift.

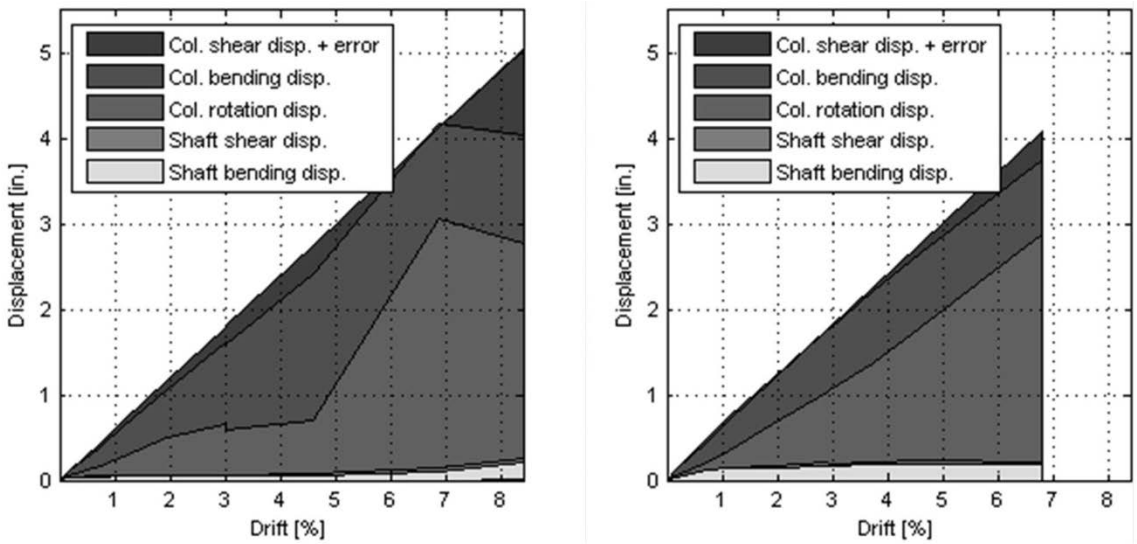

a). Specimen DS-1 b). Specimen DS-2

Figure 30. Graphs. Displacement-drift response (specimens DS-1 and DS-2).

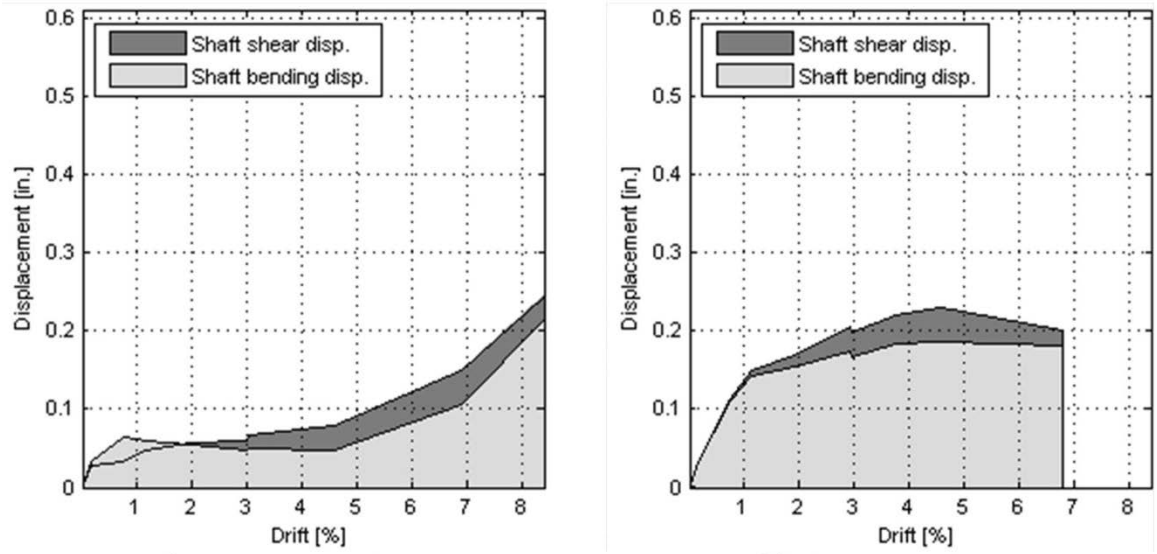

a). Specimen DS-1 b). Specimen DS-2

Figure 31. Graphs. Displacement-drift response of shaft (specimens DS-1 and DS-2).

As shown in the figures, the column bending deformations were higher in DS-1 than in DS-2 before decreasing at 7 percent drift. At this time, the column rebar was buckling and the concrete was crushed. In DS-2, the column bending deformation was smaller, and most of displacement at the top of the column was the column rotation displacement. In the shaft, the shaft shear deformation was similar in DS-1 and DS-2. However, the shaft bending in DS-2 was higher than in DS-1.

STRAINS IN COLUMN REINFORCING BARS

The longitudinal reinforcing bars in the column were gauged as shown in figure 32. Because they were configured symmetrically, only the East reinforcing bars were gauged. In both specimens, gauges were attached on the reinforcing bars in pairs at three locations: 0 in., 12 in. and 23 in. below the interface of the shaft and column.

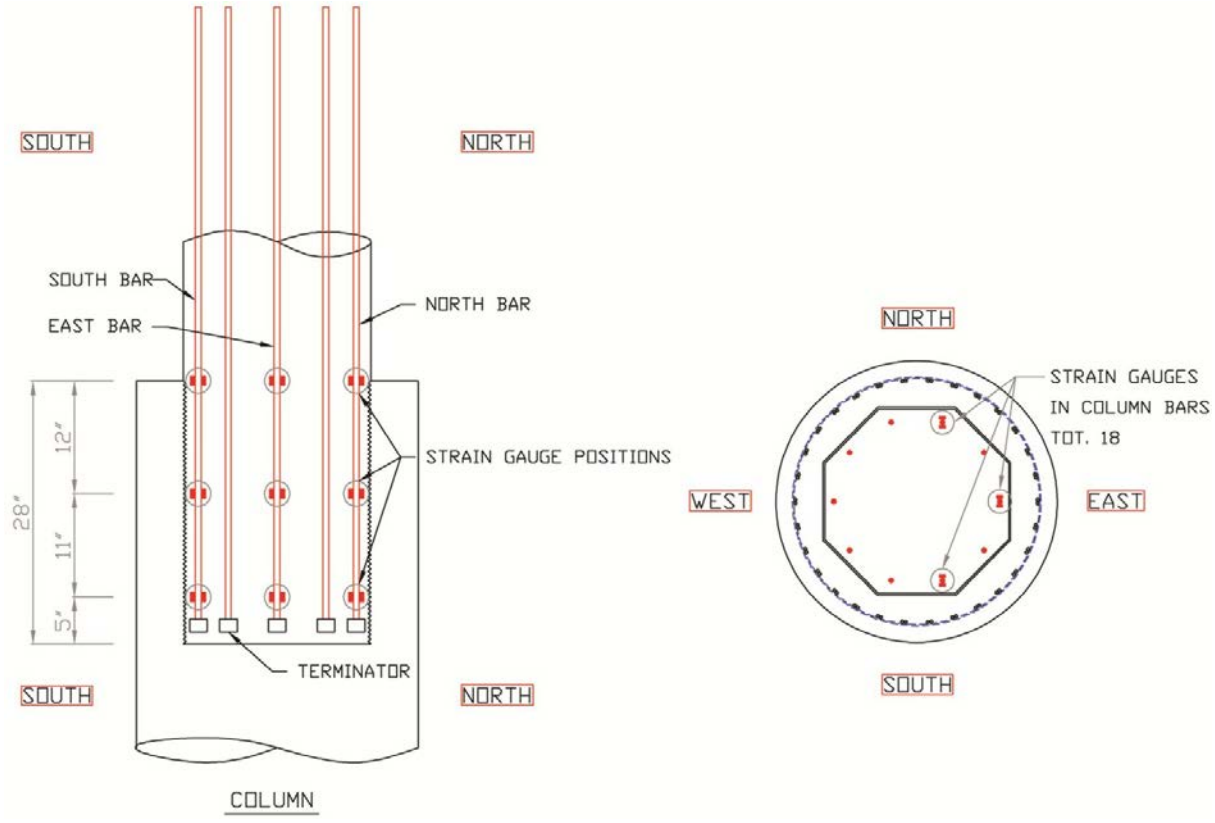

Figure 32. Diagrams. Column strain gauge positions.

Figure 33 shows the axial strain distributions (obtained by averaging the readings from each pair of gauges) over the height of the north, south, and east reinforcing bars at various drifts for DS-1 and DS-2. The strains were plotted up to 3 percent drift. Both specimens show similar strain profiles before yielding in the reinforcing bars. The plots show that the reinforcing bars in the north and south experienced alternate tension and compression as they were loaded cyclically, and they started to yield in tension at the column-shaft interface at 0.7 percent drift. The east reinforcing bars were located at the mid-depth of the column, so they experienced almost equal

tension strains when the column was displaced to the north and south. They started to yield in tension at 1.2 percent drift.

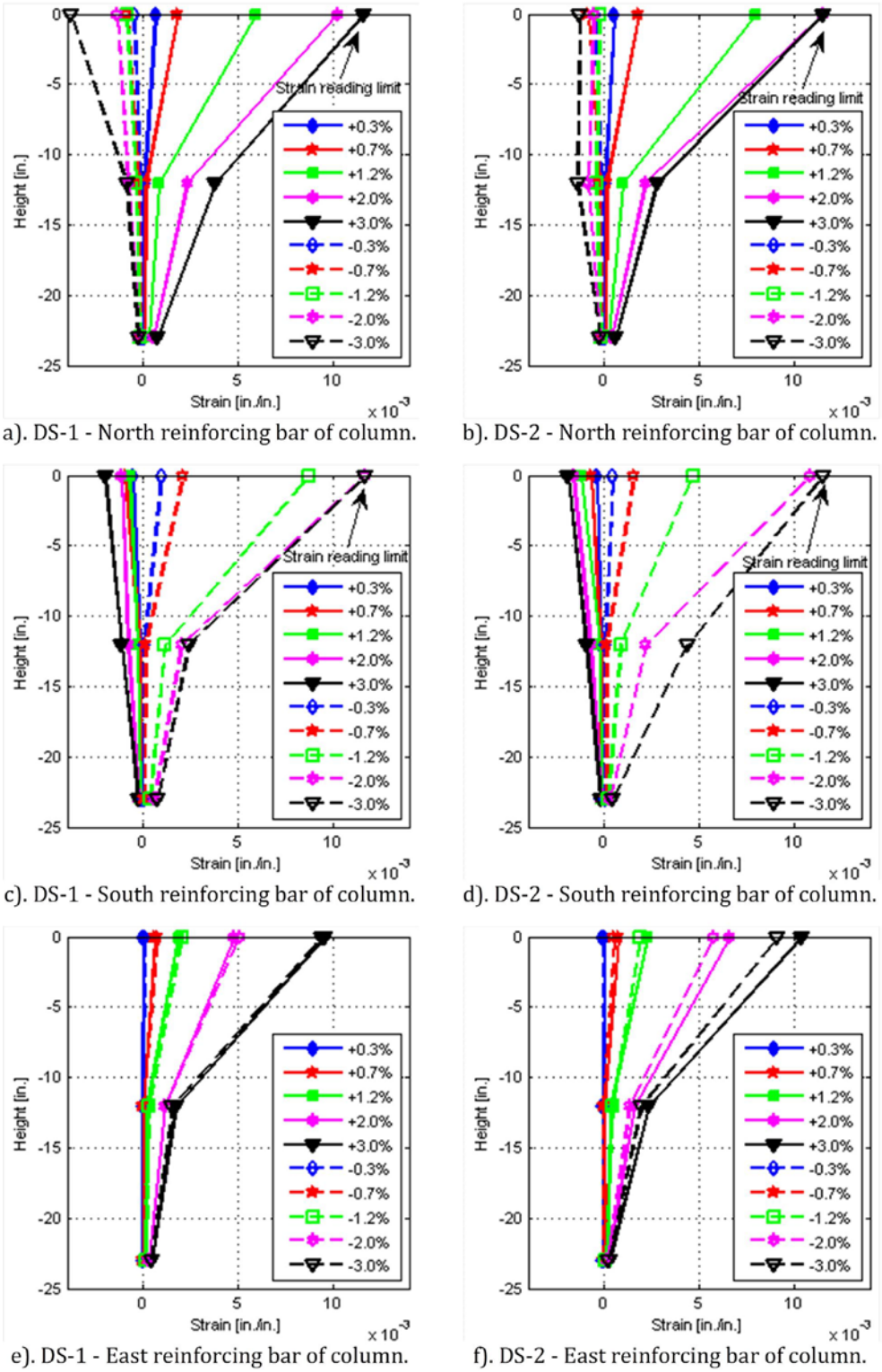

a). DS-1 - North reinforcing bar of column.

b). DS-2 - North reinforcing bar of column.

c). DS-1 - South reinforcing bar of column.

d). DS-2 - South reinforcing bar of column.

e). DS-1 - East reinforcing bar of column.

f). DS-2 - East reinforcing bar of column.

Figure 33. Graphs. Strain profiles in reinforcing bars of the column (until 3 percent drift).

At a location 12 inches below the interface, the bars started to yield at 2.0 percent drift in the north and south reinforcing bars, and at 3.0 percent drift in the east reinforcing bars in both specimens. After 3.0 percent drift, the tension strains began to exceed the measurement range of the data acquisition system, which was from -0.011 to +0.011 in./in. For real strains outside this range, the recorded value was +/- 0.011 in./in. When the real strain came back within the readable range, the correct value was again recorded.

The axial strains distributions after 3 percent drift are plotted in figure 34. Again, the recorded values are limited to the range +/- 0.11 in./in. They were plotted up to 8.4 percent drift, when the spiral in the column broke. At the next cycle, 10 percent drift, the reinforcing bars in the column broke, so no strain is presented.

The plots show that, after 3 percent drift, the strain distributions of specimens DS-1 and DS-2 were different. Consider first the bar strains at the interface. In both the north and south bars in specimen DS-2, and in the south bar in specimen DS-1, the bar experienced only modest compression strain (no more than -0.003 in./in.). This suggests that the concrete in the region was reasonably intact and was still carrying most of the compression force. By contrast, the north bar in specimen DS-1 experienced large compressive strains (to -0.009 in./in.) at 6.9 percent drift because the concrete had suffered significant damage and most of the force was being carried by the bars. However, by 8.4 percent drift, the column spiral has fractured and the bars had buckled, so the load they resisted and the strain they displayed were reduced.

At the bottom of the column, the bars in all cases never reached yield in tension. This suggests that the anchorage of the bars was being provided at least partly by bond. However, because the tension strain was close to yield, the anchor heads were clearly necessary. In specimen DS-2, the south bars exhibited high compression strains at drifts of 6.9 percent and above. These are believed to be caused by the column rocking on its edges after the resistance of the shaft had largely been lost. This can be seen in the figures illustrating the damage at the bottom of column of specimen DS-2 after testing (see appendix C).

The strain distributions in the east bars were also different between specimens DS-1 and DS-2. In specimen DS-1, the strain distribution was non-linear, suggesting that the moment decayed rapidly with depth. However, in specimen DS-2, after 4.6 percent drift, the strain distribution was linear. It suggests that there was no friction between the surface of column and the shaft, and that the moments were determined only by the horizontal forces at the top and vertical forces at the bottom of the transition region. It is also noticeable that the strains decreased after 4.6 percent drift. This is explained by the drop in load then, caused by the damage to the transition region of the shaft.

Figure 35 shows the cyclic effective force-strain relationships of the column reinforcing bars at the interface, 12 inches, and 23 inches below the interface in specimens DS-1 and DS-2. In each plot, the cyclic effective force-strain relationships were plotted for the north, south, and east reinforcing bars in blue, green, and purple, respectively, at the given depth.

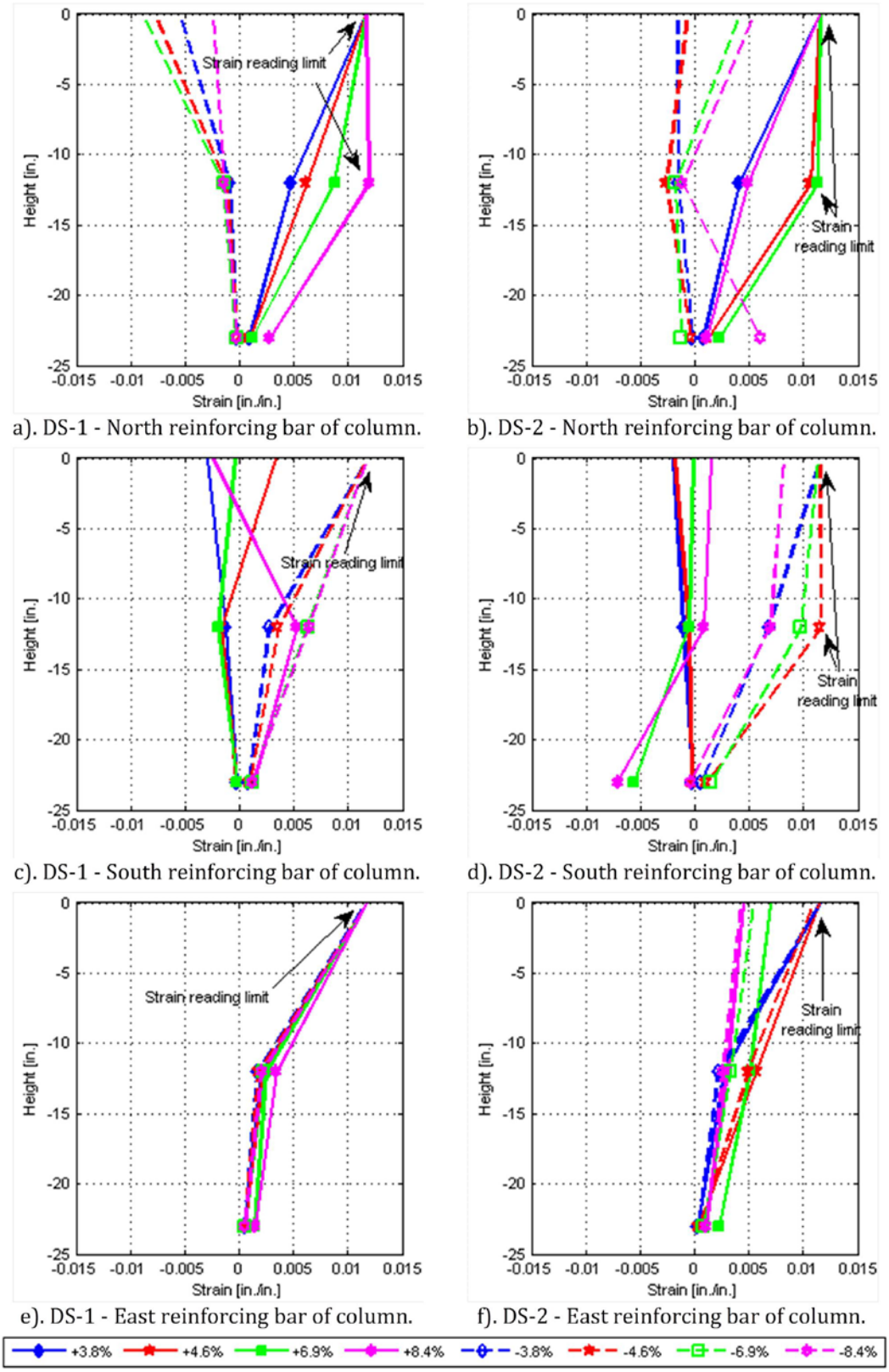

a). DS-1 - North reinforcing bar of column.

b). DS-2 - North reinforcing bar of column.

c). DS-1 - South reinforcing bar of column.

d). DS-2 - South reinforcing bar of column.

e). DS-1 - East reinforcing bar of column.

f). DS-2 - East reinforcing bar of column.

Figure 34. Graphs. Strain profiles in reinforcing bars of column (after 3 percent drift).

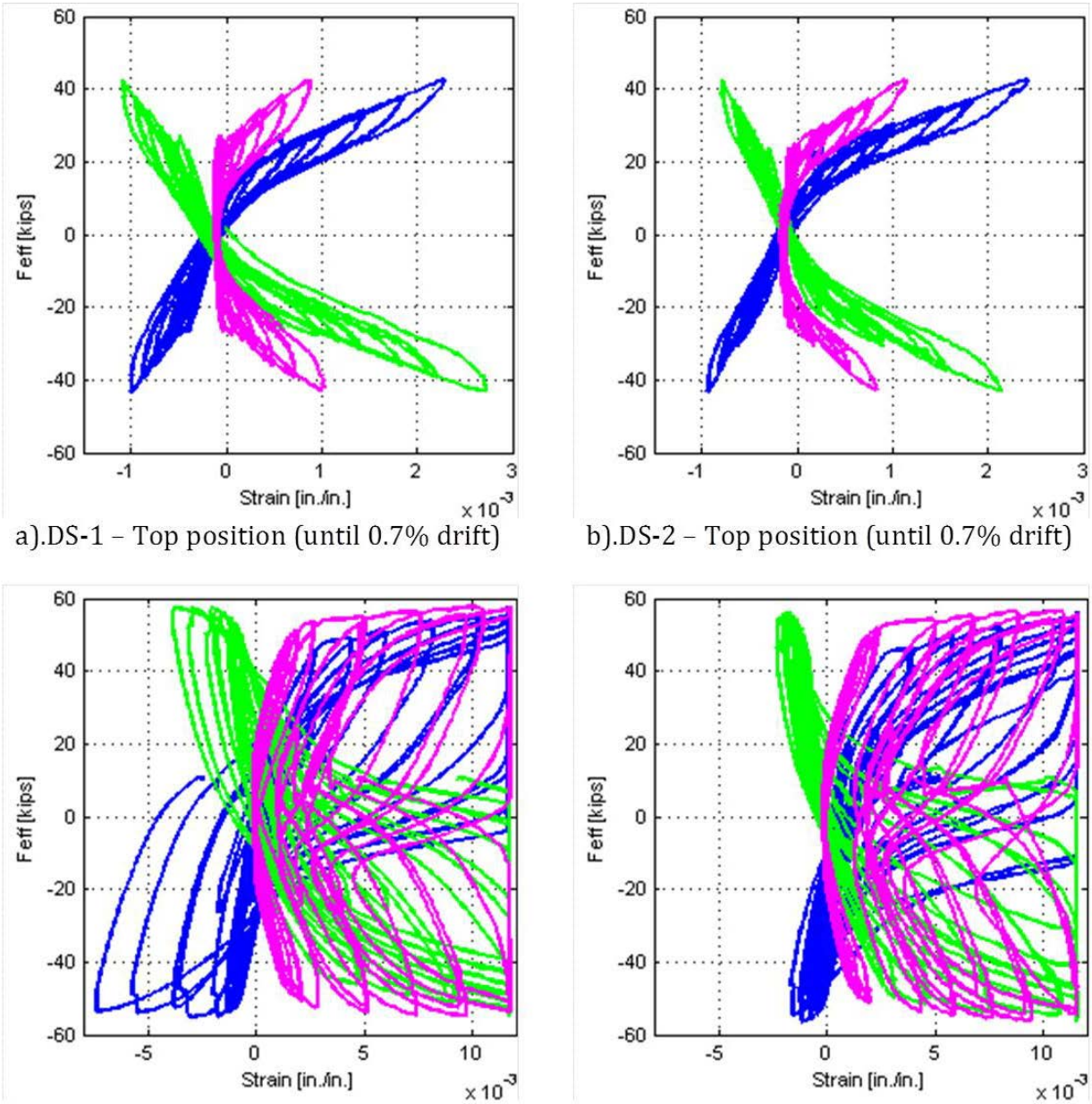

a).DS-1 – Top position (until 0.7% drift)

b).DS-2 – Top position (until 0.7% drift)

c).DS-1 – Top position (0.7%-4.6% drift)

d).DS-2 – Top position (0.7%-4.6% drift)

Figure 35. Graphs. Strain-effective force relationship of the column reinforcing bars.

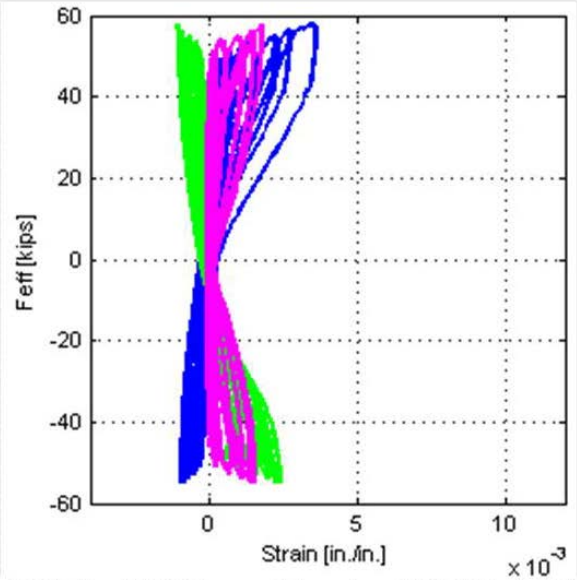

e).DS-1 – Middle position (until 3.0% drift)

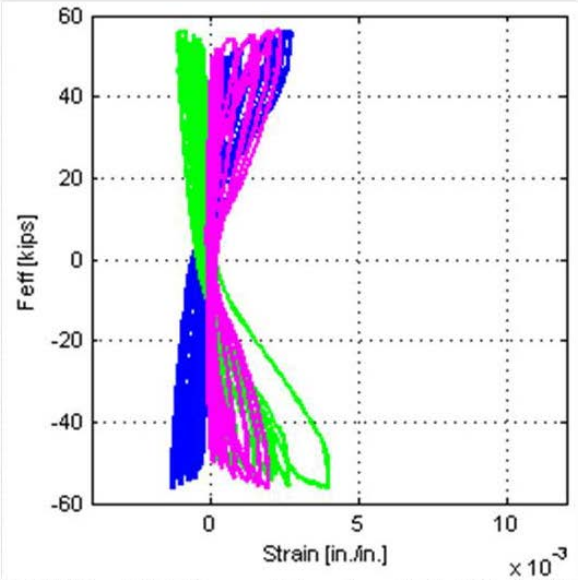

f).DS-2 – Middle position (until 3.0% drift)

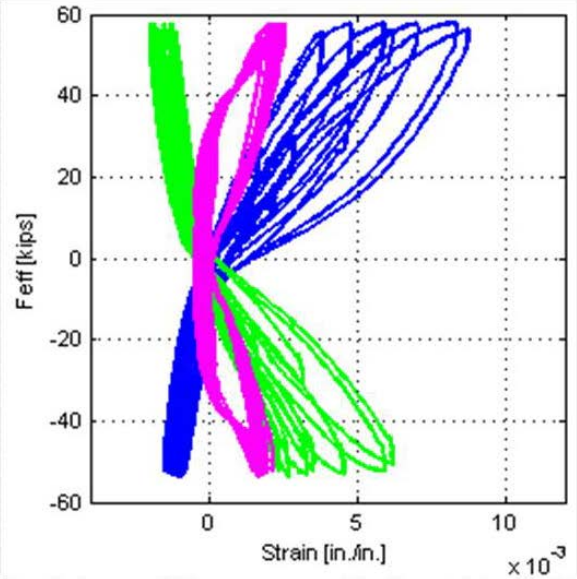

g).DS-1 – Middle position (3.0%-6.9% drift)

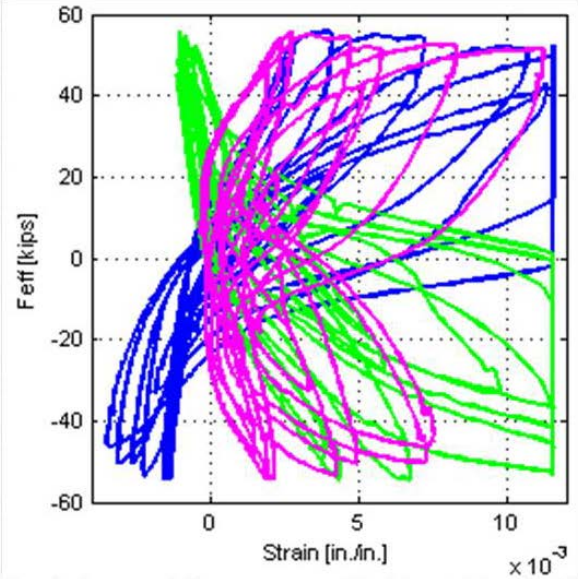

h).DS-2 – Middle position (3.0%-6.9% drift)

Figure 35. Graphs. Strain-effective force relationship of the column reinforcing bars, continued.

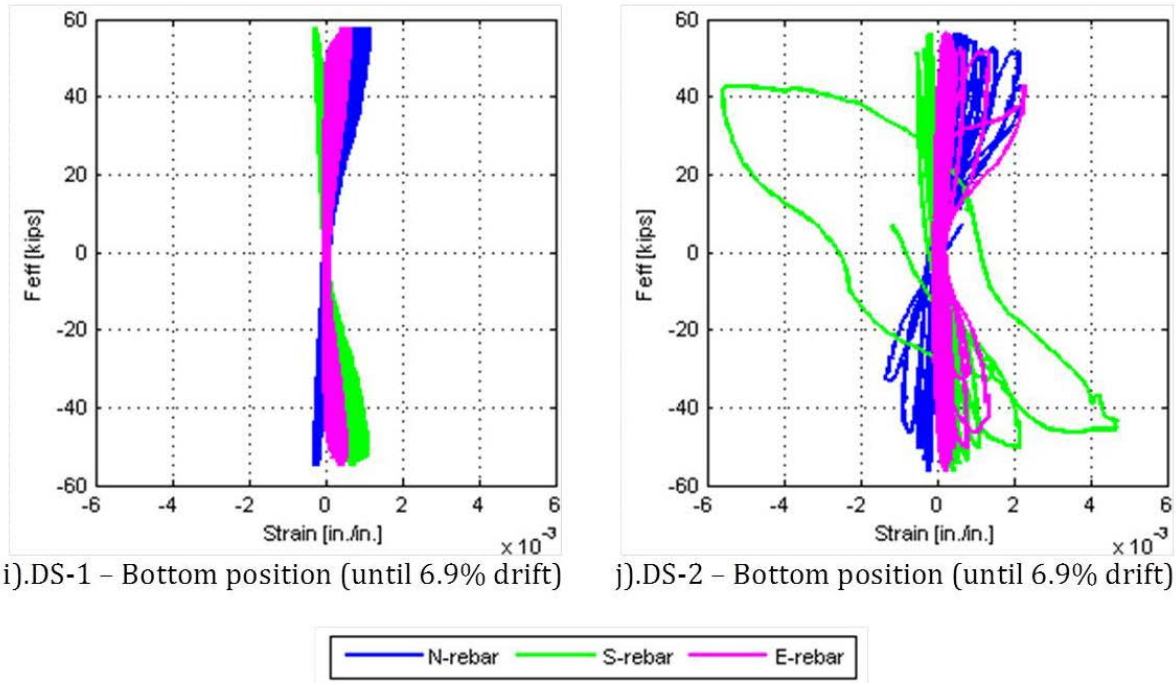

i).DS-1 – Bottom position (until 6.9% drift)

j).DS-2 – Bottom position (until 6.9% drift)

Figure 35. Graphs. Strain-effective force relationship of the column reinforcing bars, continued.

At the interface, up to 0.7 percent drift, the relationships in specimens DS-1 and DS-2 were similar. When the effective force reached 40 kips, the strains in the north, south, and east reinforcing bars were 2.25e-3, -1.0e-3, and 1.0e-3, respectively, in both specimens. This illustrated that the north and south reinforcing bars reached a yield point at 0.7 percent drift in both specimens. The relationships had a line of symmetry through effective force F_{eff} = 0. At F_{eff} = 0, all the strains in reinforcing bars were nearly zero. It suggested that the friction between the column surface and the shaft was still good. When the cyclic drift went from 0.7 percent to 4.6 percent, the relationships in DS-1 and DS-2 were different. As illustrated in the plots, the compression strain in the north and south reinforcing bars in specimen DS-1 were higher than in DS-2. This indicated that, at this time, the column concrete in DS-1 was crushed and more compression force was being carried by the bars. This contrasts with the behavior of specimen DS-2, where the column concrete was not crushed. During this period, the strains in the north, south, and east reinforcing bars in both specimens were not only non-zero when F_{eff} = 0, but they also increased after each cycle.

At 12 inches below the column-shaft interface, up to 3.0 percent drift the relationships in both specimens were similar. It can be recognized that the friction between the column surface and the shaft were still good in both specimens because the strain values at F_{eff} = 0 were nearly zero. When the drift increased from 3.0 percent to 6.9 percent, the relationships in DS-1 and DS-2 were different. In DS-1, the strain values when F_{eff} = 0 were increased a little bit, which indicated that the friction was decreased but still good. That is because when the tension reinforcing bar strain dropped from two times the yield strain (0.004 in./in.) to zero, stress in that bar must be equal to compression yield strength (assume -60 ksi). At the same time, the compression reinforcing bar strain increased from about -0.001 in./.in to zero, so stress in that bar must be equal to half of the compression yield strength (assume -30 ksi). Therefore, when F_{eff}

= 0, the moment at this position by column reinforcing bars was not zero. Thus, friction moment must equal this value to equilibrate. The maximum values were 0.008, 0.006, and 0.002 in the north, south, and east reinforcing bars, respectively. The maximum effective forces remained about 60 kips. However, in DS-2, effective force decreased from about 50 kips to 35 kips. The strain values when F_{eff} = 0 were not zero and increased after each cycle. This illustrated that the friction was lost. Therefore, most of flexure transferred to column. Thus, the strain in rebar increased dramatically over the reading capacity about 12e-3.

At 23 inches below the interface, the relationships were plotted from 0 percent to 6.9 percent drift. As shown, the reinforcing bars in specimen DS-1 remained elastic through the test. In specimen DS-2, they remained elastic up to 4.6 percent drift, during which the strain values were similar to those in specimen DS-1, but the bars yielded in tension thereafter. Yielding at the anchor head, 23 inches below the interface, implies that the bar experienced little change in force along its length, and therefore little friction between the column and shaft.

STRAINS IN SHAFT REINFORCING BARS

The longitudinal reinforcing bars in the shaft were gauged as shown in figure 36. The symmetry of the shaft and column was utilized; thus, only the east bars were gauged. In both specimens, gauges were attached on the reinforcing bars in pairs at three locations: 4 inches, 16 inches, and 28 inches below the shaft-column interface.

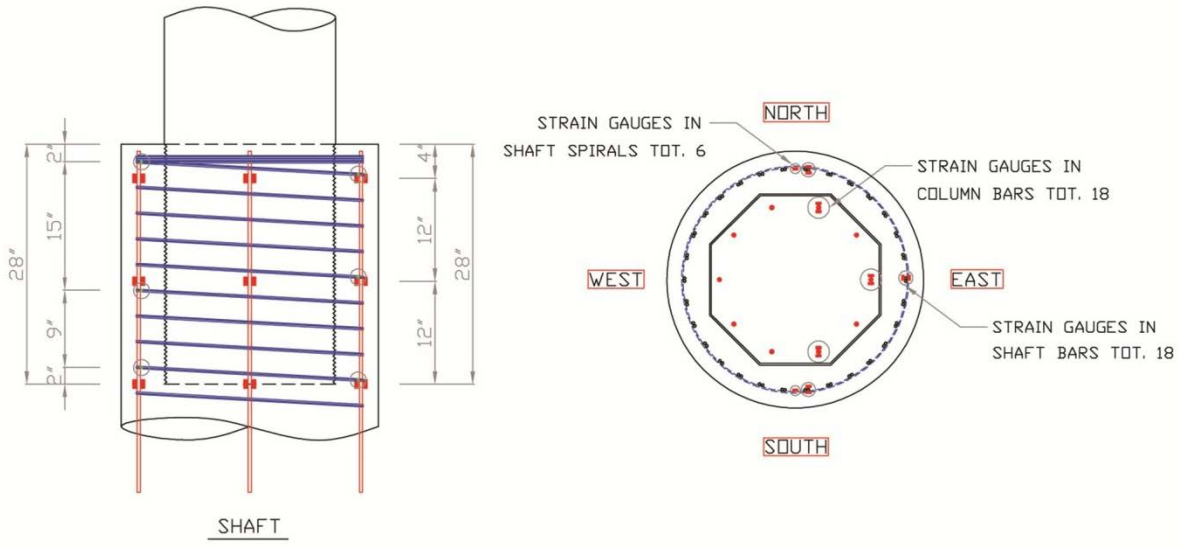

Figure 36. Diagrams. Strain gauge positions in the shaft.

The strains in the shaft reinforcing bars in both specimens are shown in figure 37 and figure 38. At 4 inches below the interface position, the strains recorded by the inner and outer gauges at the same position in the north bar in specimen DS-1 were similar. The strain gauge pair in the south bar in specimen DS-1 were damaged before testing. In the east bars, the two gauges gave nearly the same values until near the end of the test. The fact that the gauges gave nearly the same values implies that the bars were primarily in tension, with little bending.

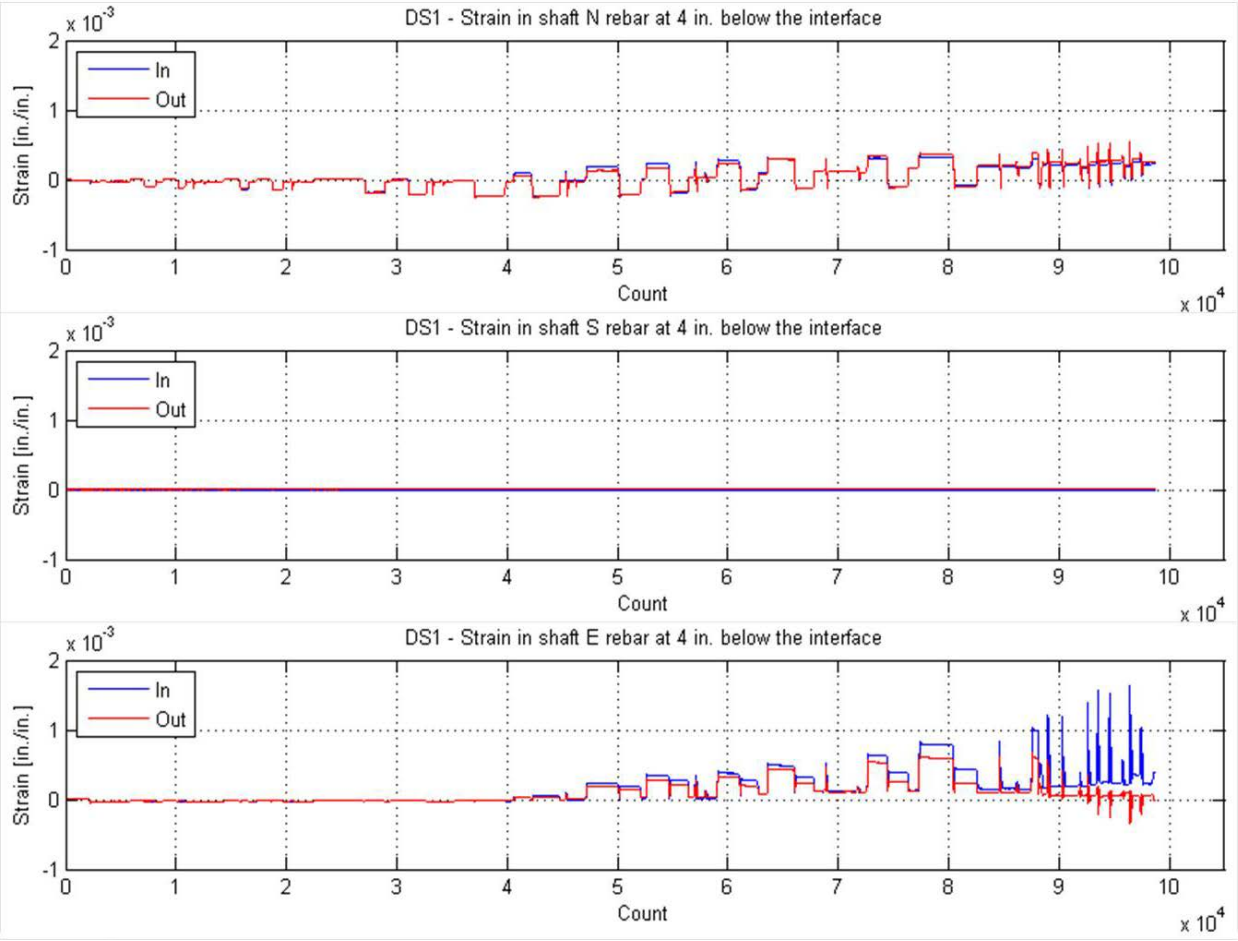

Figure 37. Graphs. Strain in shaft reinforcing bars in specimen DS-1.

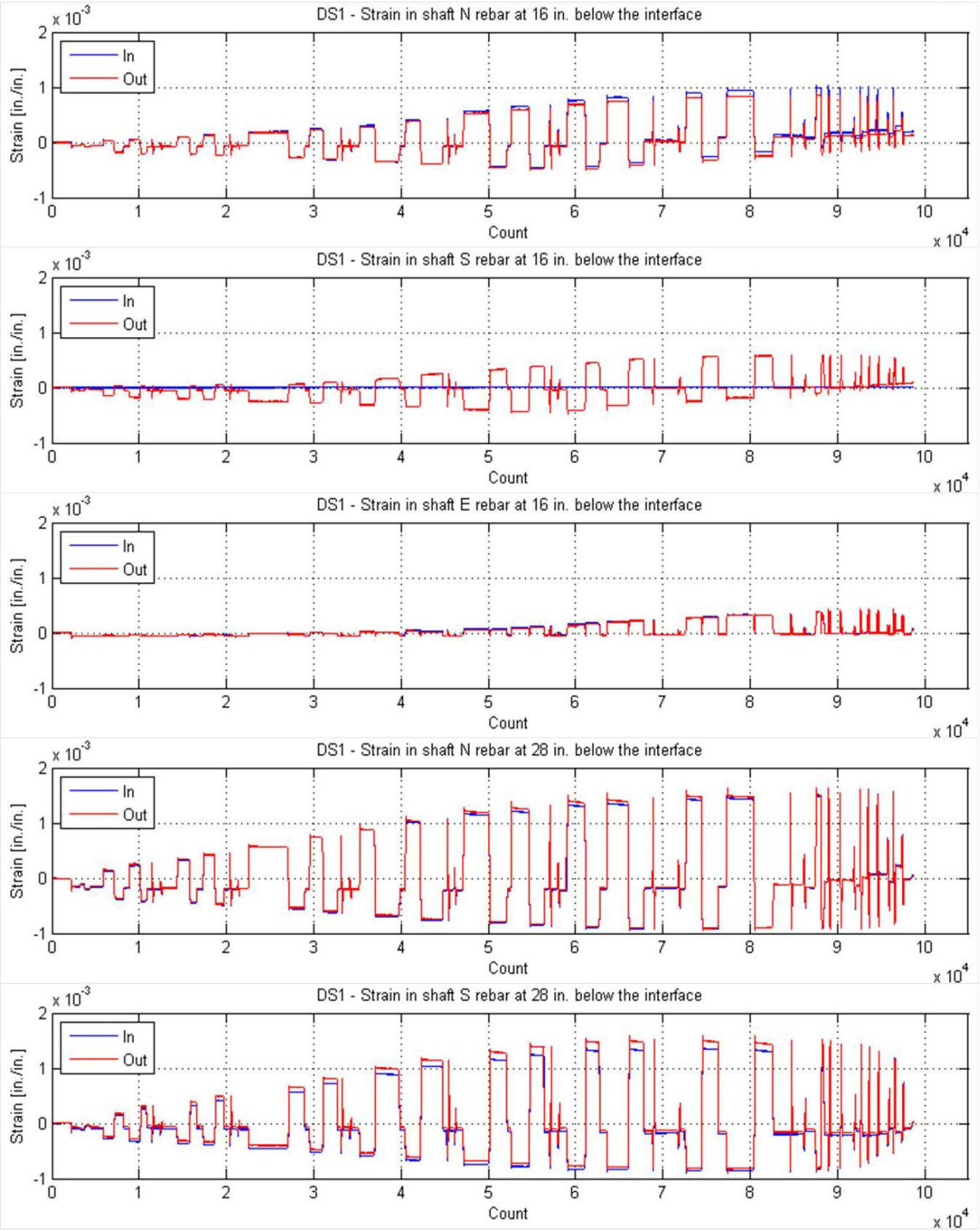

Figure 37. Graphs. Strain in shaft reinforcing bars in specimen DS-1, continued.

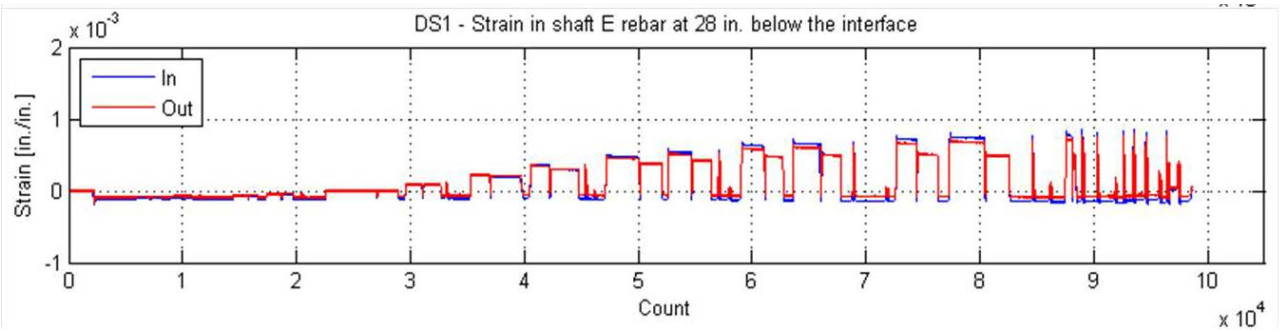

Figure 37. Graphs. Strain in shaft reinforcing bars in specimen DS-1, continued.

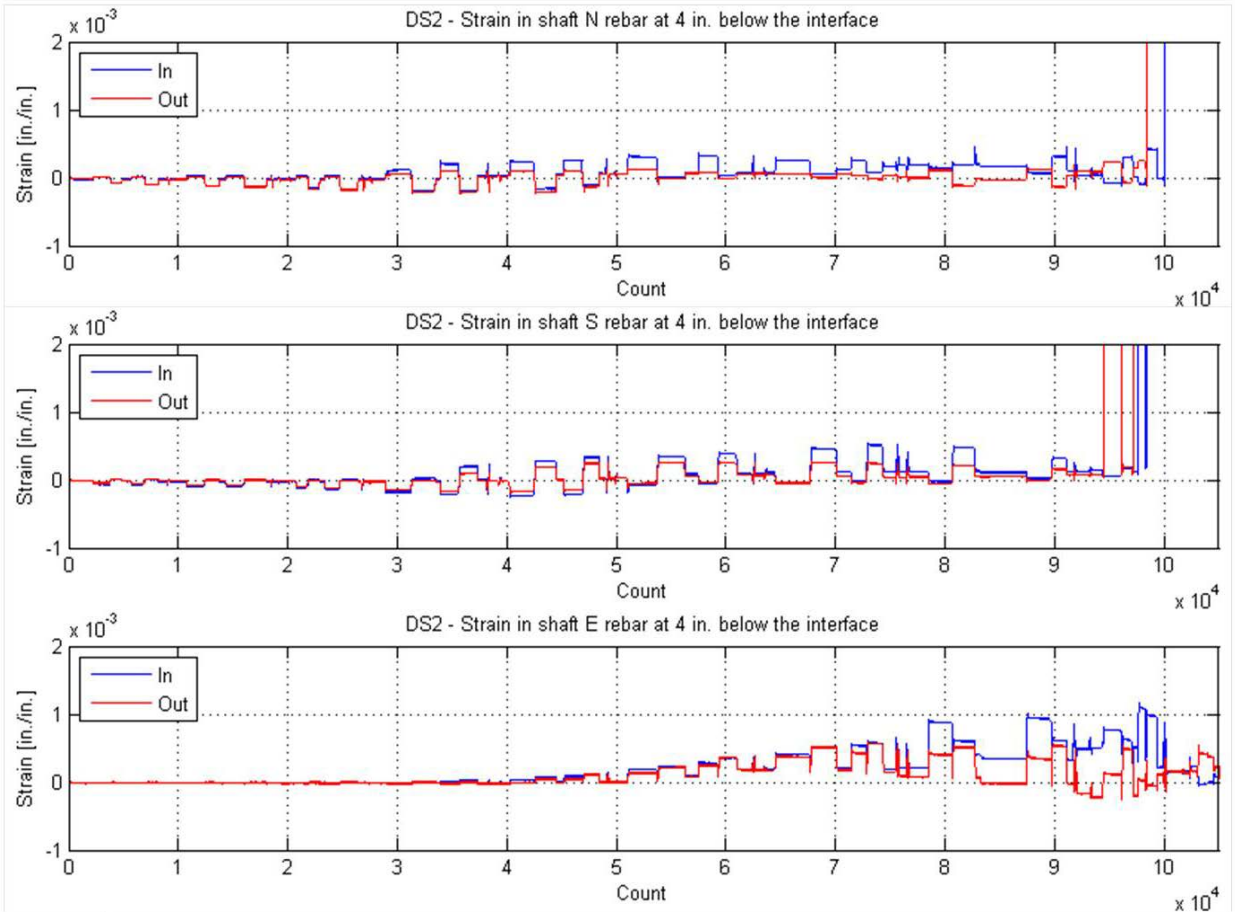

Figure 38. Graphs. Strain in shaft reinforcing bars in specimen DS-2.

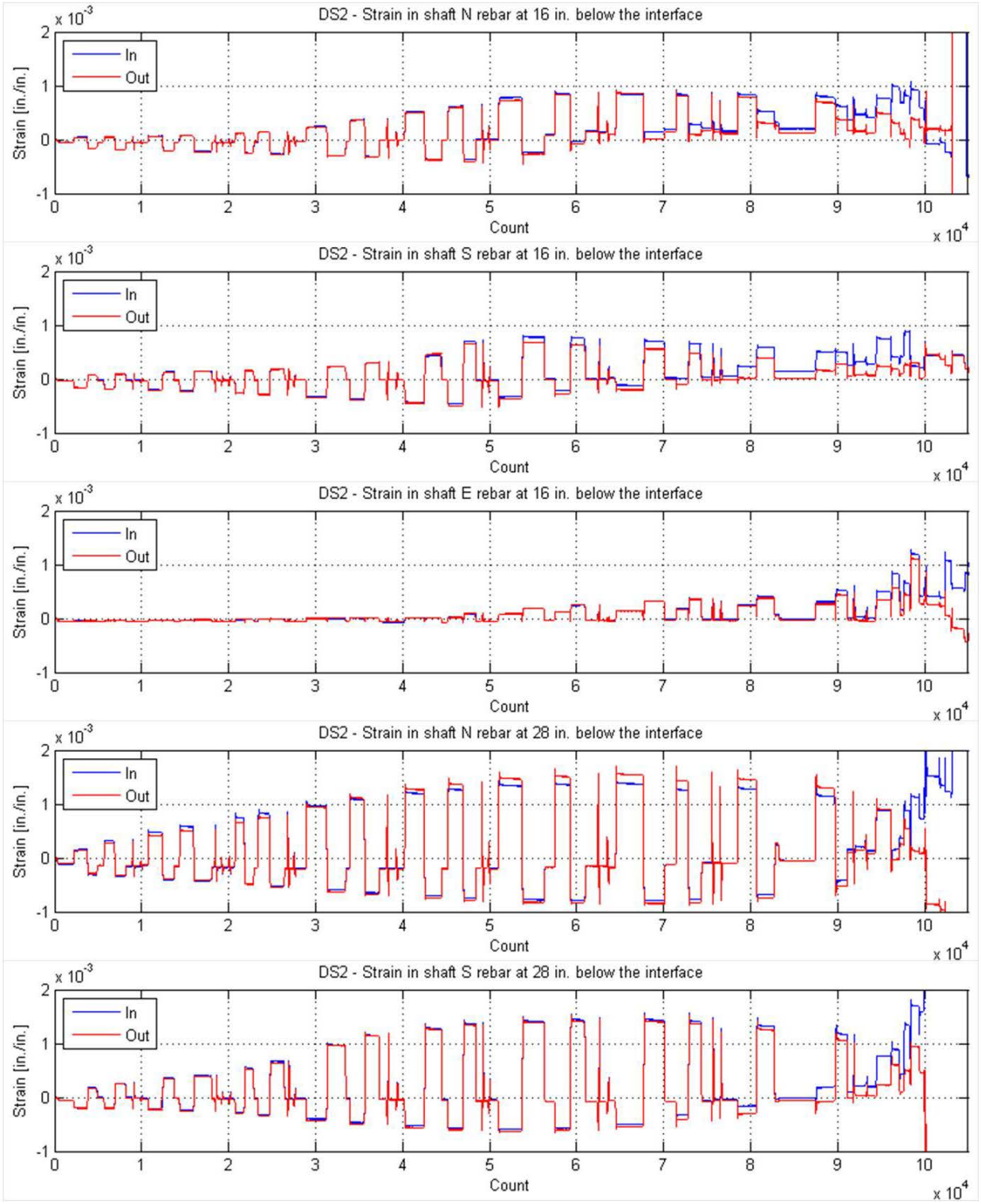

Figure 38. Graphs. Strain in shaft reinforcing bars in specimen DS-2, continued.

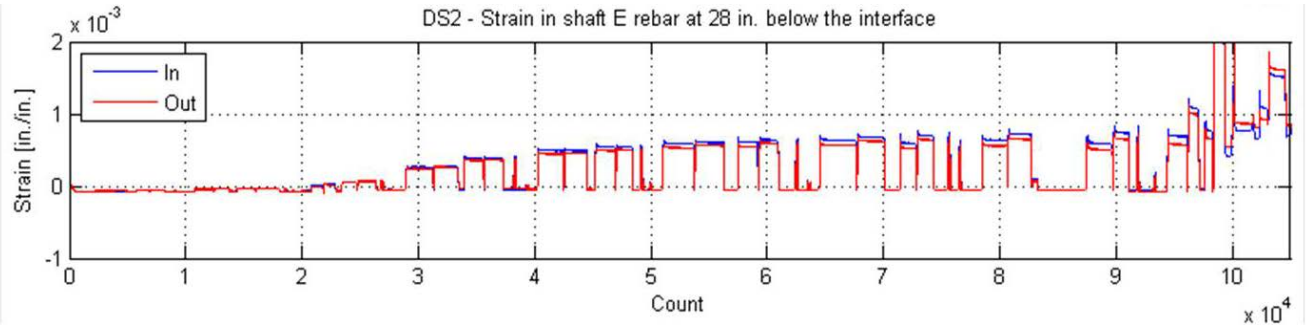

Figure 38. Graphs. Strain in shaft reinforcing bars in specimen DS-2, continued.

In specimen DS-2, the values of the strain gauge pairs in the north and south bars were relatively different from count = 40,000 (0.9 percent drift) to the end of the test. These differences in gauge readings suggest that local bending happened at these positions. As illustrated in the plots, local bending caused the outside strain gauges (red line) to experience less tension and the inside strain gauges (blue line) to experience more tension. This local bending occurred after the transition region of the shaft cracked and the spiral in it yielded. This behavior was not seen at the positions 16 and 28 inches below the interface in specimen DS-1, and it can only be seen at the very end cycles when the spirals of the shaft were broken in specimen DS-2.

The pattern of strains in the vertical bars of the shaft, 4 inches below the interface, is also consistent with the way that the shaft behaved. Before cycle 4-1 (0.7 percent drift, count = 29,000), the shaft was essentially uncracked, so it behaved like a beam made from continuous, uncracked material. Because the applied load consisted of both compression and bending, the vertical bar strains on the compression side were higher than the tension strains on the opposite side. However, when the shaft cracked (at cycle 4-1, 0.7 percent drift), the concrete could no longer resist tension. Then the tension strain at the top of the shaft was higher than the compression strain on the opposite side. This change in the strain pattern, from high compression to high tension, is the one seen in the gauge records.

The strain distributions (the average of each pair of gauge readings) over the height of the north, south, and east shaft bars at various drifts for specimen DS-1 and DS-2 are shown in figure 39. The strains were plotted up to 3.0 percent drift. Both specimens show similar strain profiles before 1.2 percent drift. Until 0.7 percent drift, tension strains at the top position (4 inches below the interface) were nearly zero in both specimens. The compression strains were higher, about $200\mu\epsilon$. However, after 0.7 percent drift, the top of the shaft cracked vertically and diagonally, so the tension strain in the bars increased as explained above. After 1.2 percent drift, the strain profiles in specimens DS-1 and DS-2 were different. The tension strains increased when drift increased. However, the compression strains at 4 inches and 16 inches below the interface decreased. The compression strain decreased gradually in specimen DS-1 and suddenly in specimen DS-2. This suggested that the friction between the column surface and the shaft reduced gradually in specimen DS-1 and was lost suddenly and almost completely in specimen DS-2 because the compression strain values dropped to nearly zero. The increasing of compression strain at 28 inches below the interface indicated that, at this time, friction was still good at this position in both specimens.

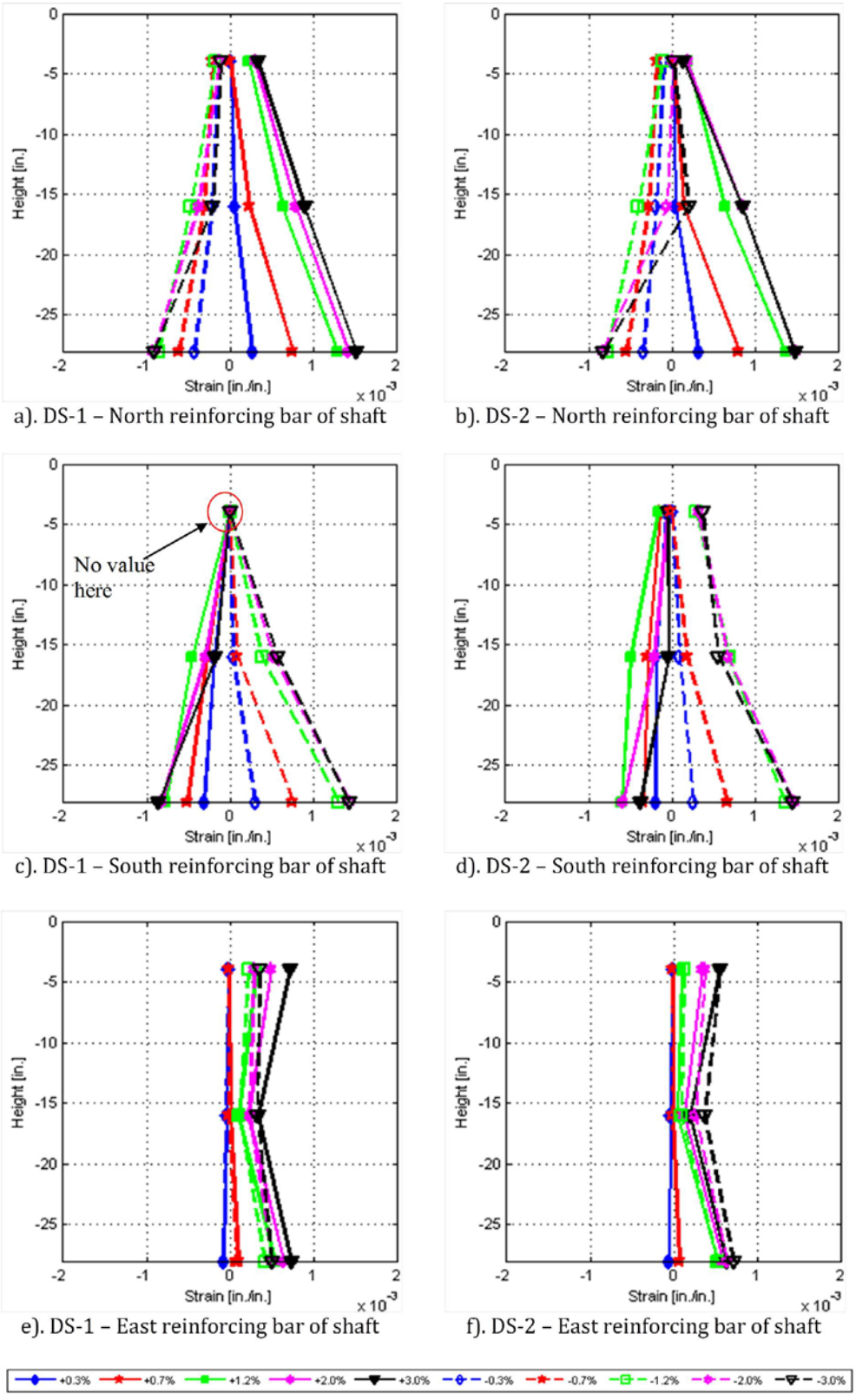

a). DS-1 – North reinforcing bar of shaft

b). DS-2 – North reinforcing bar of shaft

c). DS-1 – South reinforcing bar of shaft

d). DS-2 – South reinforcing bar of shaft

e). DS-1 – East reinforcing bar of shaft

f). DS-2 – East reinforcing bar of shaft

Figure 39. Graphs. Strain profiles in the shaft reinforcing bars.

Figure 40 shows the cyclic effective force-strain relationships of the shaft bars at 4, 16, and 28 inches below the interface, for specimens DS-1 and DS-2. In each plot, the cyclic effective force-strain relationship is plotted for the north, south, and east bars in blue, green, and purple, respectively. As illustrated, the strain values in all gauges in the shaft reinforcing bars were smaller than 0.002. This indicated that all the shaft-reinforcing bars remained elastic throughout the test.

At 4 inches below the interface, as shown in the figures, the strain gauges in the south bar in DS-1 were broken before testing. Up to 0.7 percent drift, the force-strain relationships in specimens DS-1 and DS-2 were similar. When the effective force reached 40 kips, the strains in the north, south, and east reinforcing bars were about 25, 0, and 200$\mu\epsilon$, respectively, in both specimens. This illustrates that, in both specimens, the south bars were subjected to more compression when the effective force increased and the north reinforcing bars were subjected to more compression when the effective force decreased. The relationships had a line of symmetry through effective force F_{eff} = 0. At F_{eff} = 0, all the bar strains were about -25$\mu\epsilon$. As was shown in the column bar behavior, this suggested that the friction between the column surface and the shaft was still good. When the cyclic drift went from 0.7 percent to 4.6 percent, the relationships in DS-1 and DS-2 were also similar. As illustrated in the graphs, the compression strain in the north bar in specimen DS-1 and the north and south bars in DS-2 decreased while the tension strain increased after each cycle. This suggested that, at this time, the shaft concrete was cracked in the top of the shaft, so the tensile force transferred to the reinforcing bars.

At 16 inches below the column-shaft interface position, the behaviors were nearly the same as at the previous position. Until 1.5 percent drift the relationships in both specimens were similar. The north and south reinforcing bars were still transferring more compression. The friction between the column surface and the shaft was still good in both specimen because the strain values at F_{eff} = 0 were nearly -50$\mu\epsilon$. When drift went from 1.5 percent to 6.9 percent, DS-1 and DS-2 behaved differently. In DS-1, the strain values when F_{eff} = 0 were increase a little bit, indicating the friction was decreased but still good. Therefore, the compression strains in the reinforcing bars were decreased gradually. The maximum effective forces remained about 60 kips. However, in DS-2, effective force decreased from about 50 kips to 35 kips. The strain values when F_{eff} = 0 were not zero and increased after each cycle. It illustrated that, at this period, the concrete was cracked and could not sustain tensile forces. Therefore, most of the tension transferred to the spirals. Thus, when the strain in the spiral increased over the yielding point, it would have residual strain. Consequently, there would have been some force in the reinforcing bars and spirals when the horizontal load was released to zero.

At 28 inches below the interface position, the relationships were plotted up to 6.9 percent drift. As shown in the figures, the friction was still good, and the reinforcing bars were still in the elastic range in DS-1. In DS-2, before 4.6 percent drift, the behavior was similar to that in specimen DS-1. The friction was good, and the reinforcing bars remained elastic. However, after 4.6 percent drift, the friction was lost and the spirals were broken, and the strains in the rebar decreased dramatically.

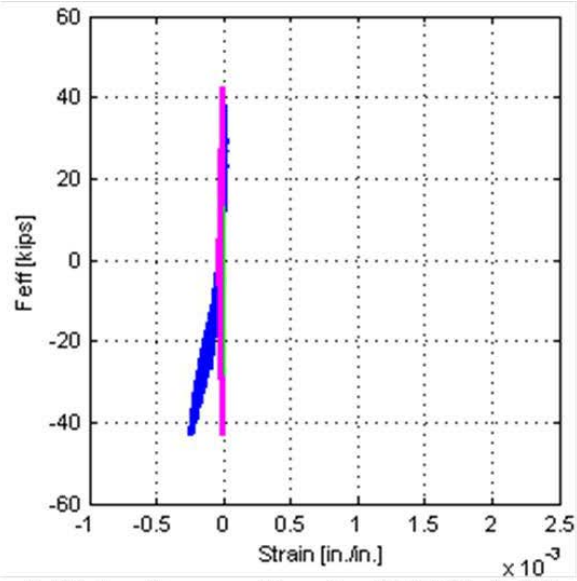

a).DS-1 – Top position (until 0.7% drift)

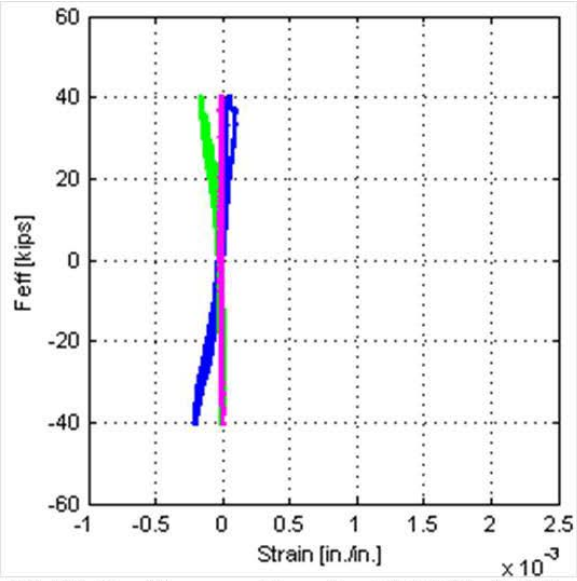

b).DS-2 – Top position (until 0.7% drift)

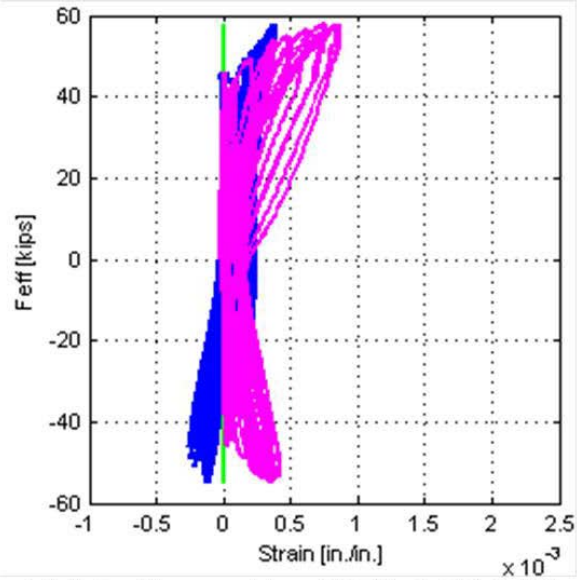

c).DS-1 – Top position (0.7%-4.6% drift)

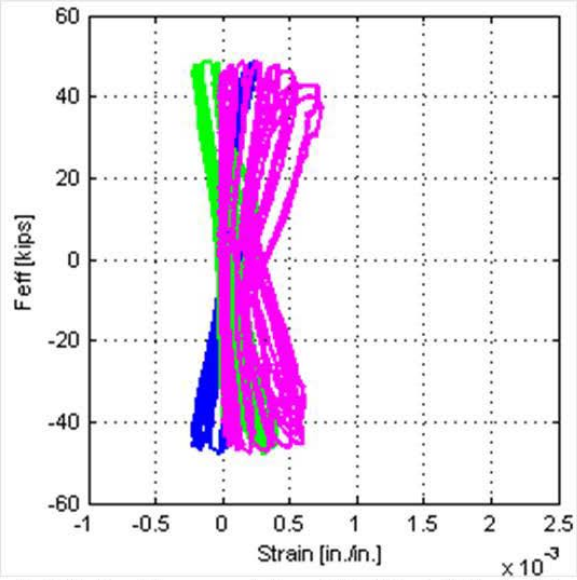

d).DS-2 – Top position (0.7%-4.6% drift)

Figure 40. Graphs. Strain-Effective force relationship of the shaft reinforcing bars.

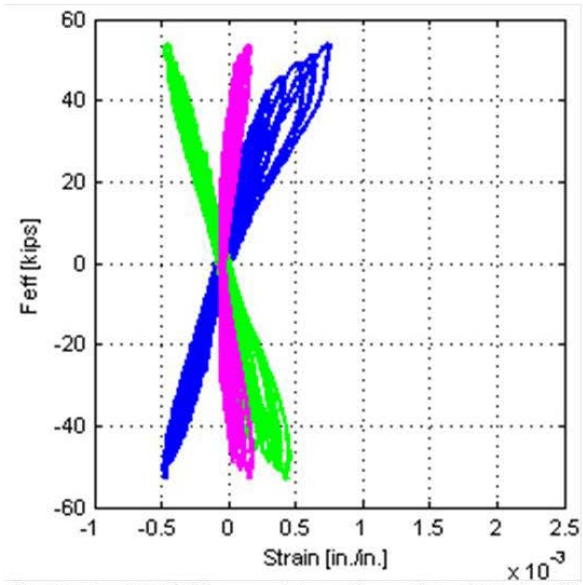

e).DS-1 – Middle position (until 1.5% drift)

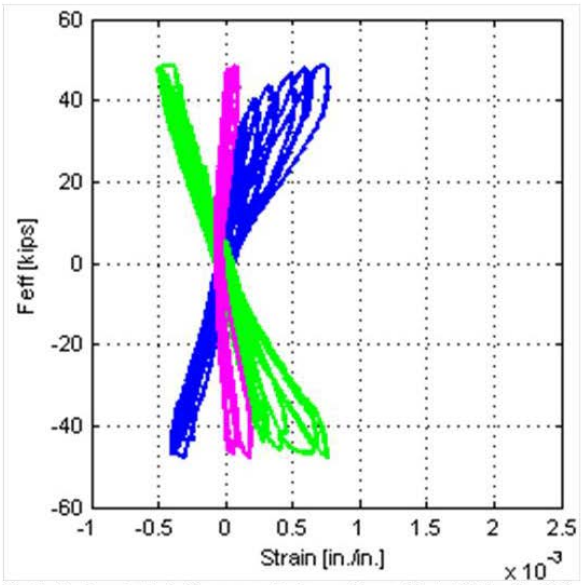

f).DS-2 – Middle position (until 1.5% drift)

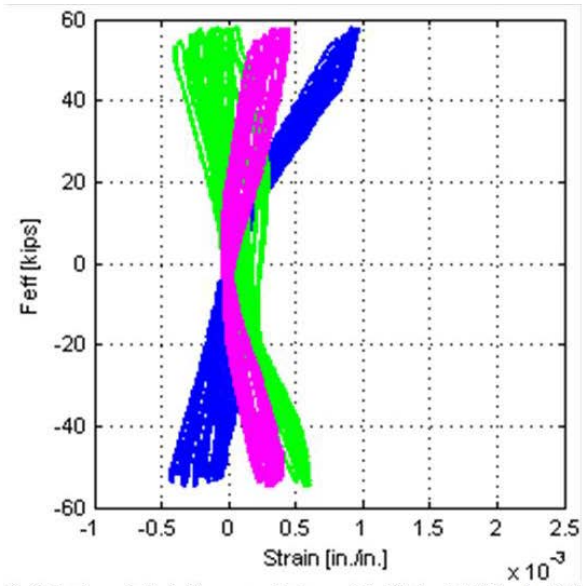

g).DS-1 – Middle position (1.5%-6.9% drift)

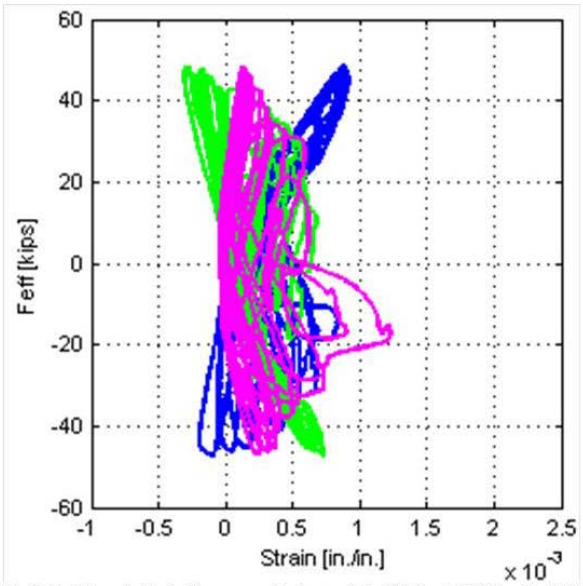

h).DS-2 – Middle position (1.5%-6.9% drift)

Figure 40. Graphs. Strain-Effective force relationship of the shaft reinforcing bars, continued.

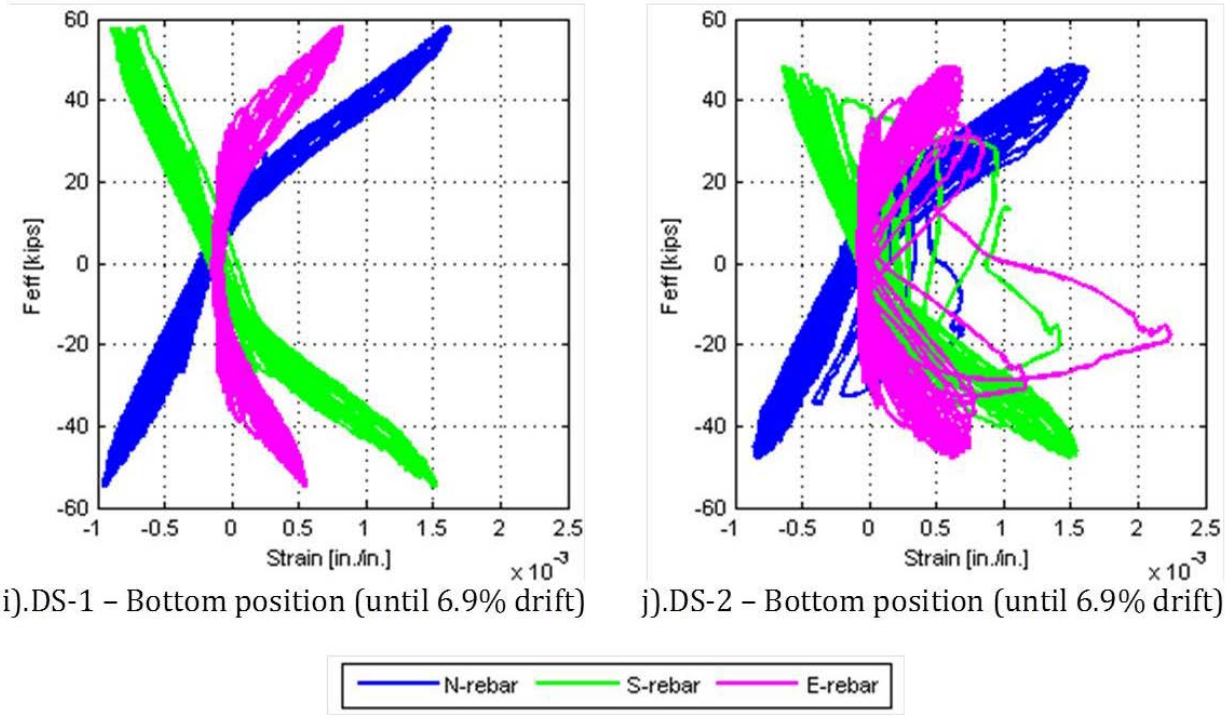

Figure 40. Graphs. Strain-Effective force relationship of the shaft reinforcing bars, continued.

STRAINS IN SHAFT SPIRALS

Because of the symmetry of the column longitudinal bars, only the east and south sides of the shaft spirals were gauged. In both specimens, gauges were attached on the spirals at three locations close to those of the gauges on the vertical bars—4, 16, and 28 inches below the interface of the shaft and column. At each place, only one strain gauge was used.

The strains in the shaft spiral are shown in figure 41. Because all three gauges on the south side of specimen DS-1 were broken before testing, only the spiral strains on the east side in DS-1 and on the east and south sides in DS-2 were plotted.

The overall trends were as follows:

- In both specimens, the strains in the spiral were tensile regardless of the direction of loading.
- In both specimens, the strains were much larger at the top of the shaft than in the middle or bottom.
- The spiral in specimen DS-1 just reached the yield point. However, in specimen DS-2, the spiral first yielded at the top at 3 percent drift and fractured at 6.9 percent drift.
- The strain was slightly larger at the south gauge than at the east gauge, at any drift ratio, in specimen DS-2. That comparison was not possible in specimen DS-1 because no data were available from the south gauges.

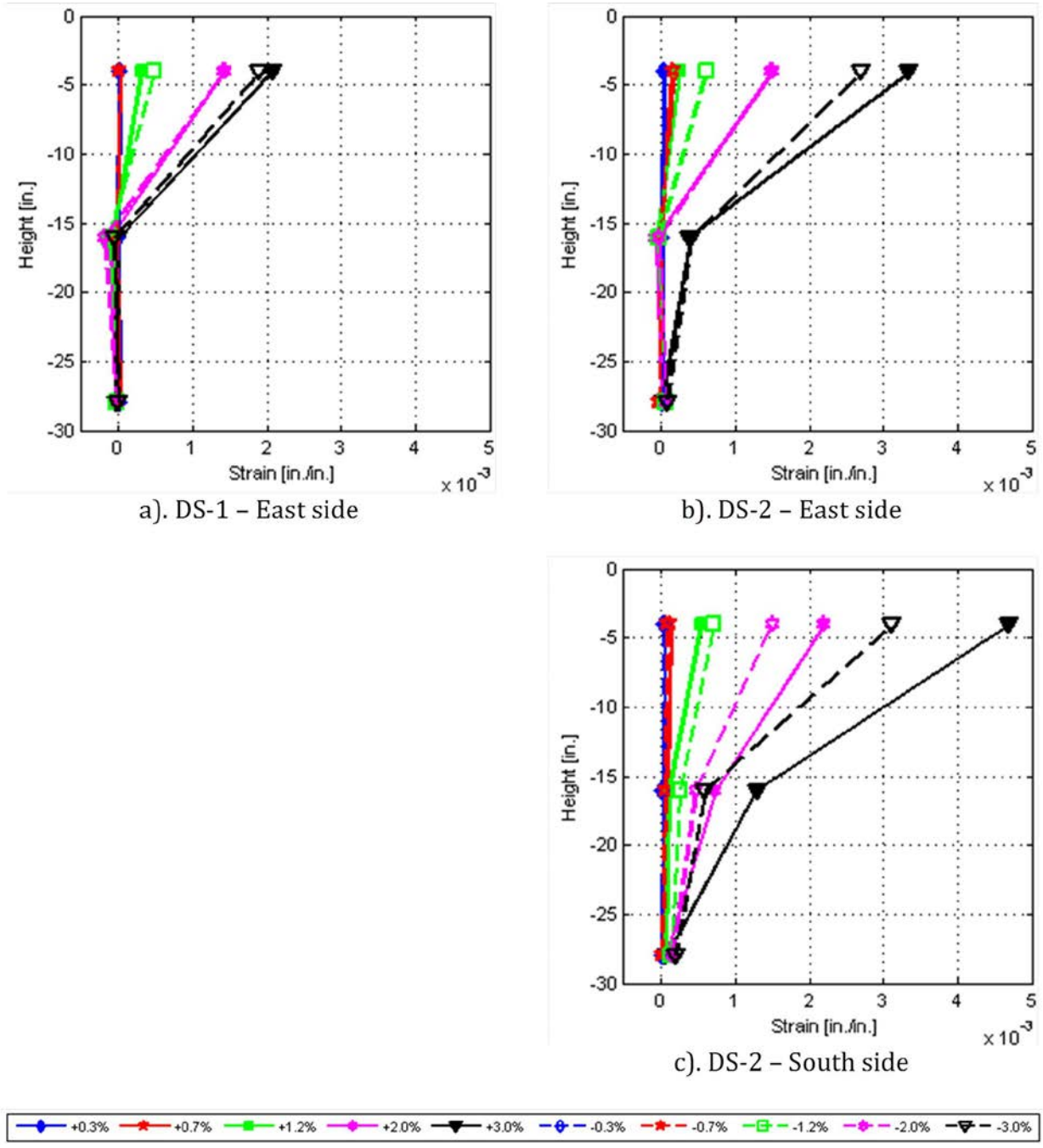

Figure 41. Graphs. Strain in shaft spiral.

The fact that the strains in specimen DS-2 were higher than those in specimen DS-1 is consistent with the lower spiral steel ratio in specimen DS-2.

As illustrated in the graphs, in specimen DS-1, tension strain increased at the top position after each cycle and reached 0.002 at 3.0 percent drift. At the middle position, strains were in compression and increased a little until 3.0 percent drift. At the bottom position, strains were nearly zero. However, the spiral strains in specimen DS-2 were different. All strain values were

in tension at 3.0 percent drift. At the top position, the strains were in tension and increased after each cycle like in DS-1, but the values were higher. The maximum strain on the east side was about 3.4e-3, and on the south side it was 4.7e-3. At the middle position, until 2.0 percent drift, strain was nearly zero on the east side and increased to 0.4e-3 at 3.0 percent drift. On the south side, strains increased in tension after each cycle and reached 1.25e-3 at 3.0 percent drift. At the bottom position, the maximum strains were about 0.2e-3. This different behavior between specimens DS-1 and DS-2 suggests that, until 3.0 percent drift, friction between the column and shaft was lost from the interface position to some position above the mid-position (16 inches below the interface) in DS-1. However, in specimen DS-2, friction was lost at a position below the mid-position.

CHAPTER 6. DATA ANALYSIS

In bridges designed by WSDOT, the diameter of a drilled shaft is larger than that of the column that it supports. The splices between the longitudinal bars in the transition region are therefore non-contact splices, and special design requirements are necessary. McLean and Smith proposed a model for such a splice, and WSDOT has incorporated a modified version of it into the BDM.[11,18] However, the predictions of the modified model are not consistent with the test results from specimens DS-1 and DS-2. Therefore, a new conceptual model was developed to describe the observed behavior of the column-to-shaft "socket" connection.

First, the overall statically determinate test assembly was analyzed to give some guidance on parameters for design. Then, a simple strut-and-tie model was proposed to determine the amount of lateral reinforcement required in the connection. The proposed model is simple, easy to use in design, and consistent with the data from the two tests. However, because it is based on evidence from only two tests (DS-1 and DS-2), it cannot be guaranteed to provide correct predictions in all cases, and further testing is needed to support its use on a wider basis.

NON-CONTACT LAP SPLICES MODELS

McLean and Smith proposed both two-dimensional and three-dimensional models.[18] These models are based on the truss analogy to represent the force transfer mechanism within a splice.

Figure 42 illustrates a two-dimensional representation of the force transfer between non-contact longitudinal bars.

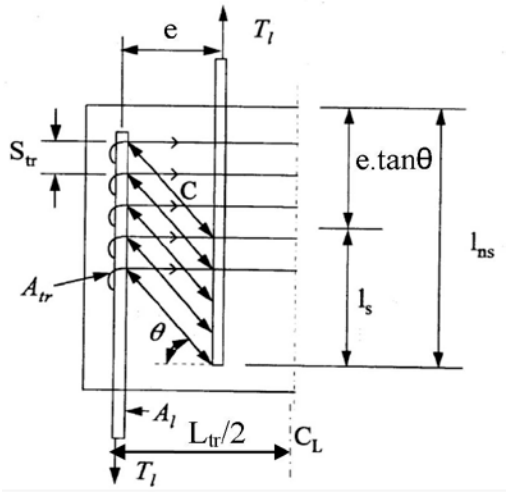

Figure 42. Diagram. Two-dimensional behavioral model for non-contact lap splices.

The transverse reinforcement is determined from the equation in figure 43.

$$\frac{A_{tr}}{s_{tr}} = \frac{A_l f_{ul}}{f_{yt}\, l_s \tan\theta}$$

Figure 43. Equation. Shaft transverse reinforcement for rectangular columns.

In this equation:

A_{tr} = area of shaft transverse reinforcement or spiral (in.^{2}).

A_l = total area of longitudinal column reinforcement (in.^{2}).

f_{yt} = specified minimum yield strength of shaft transverse reinforcement (ksi).

f_{ul} = specified minimum tensile strength of column longitudinal reinforcement (ksi), 90 ksi for A615 and 80 ksi for A706.

l_s = Class C tension lap splice length of the column longitudinal reinforcement (in.).

s_{tr} = spacing of shaft transverse reinforcement (in.).

θ = inclination angle of the strut (degree or rad).

This equation indicates that a longer splice requires less spiral, and vice versa. For the special case of $\theta = 45°$ the equation becomes as shown in figure 44.

$$\frac{A_{tr}}{s_{tr}} = \frac{A_l f_{ul}}{f_{yt}\, l_s}$$

Figure 44. Equation. Shaft transverse reinforcement for rectangular columns with $\theta = 45°$.

There is no unique definition for the optimum value of θ to be used. One possible criterion is to use the θ that minimizes the total volume of steel, including both longitudinal and transverse steel, required in the splice. It is given by the equation in figure 45.

$$VOL_s = 2A_l l_{ns} + \frac{A_{tr}\, l_s}{s_{tr}} L_{tr}$$

Figure 45. Equation. Volume of shaft reinforcement for rectangular columns.

In figure 45:

l_{ns} = total noncontact lap splice length.

= $l_{ns} = l_s + e.\tan\theta$

L_{tr} = distance between the outer bars.

Substituting figure 44 into figure 45 results in the equation in figure 46.

$$VOL_s = 2A_l(l_s + e.\tan\theta) + \frac{A_l f_{ul}}{f_{yt}\tan\theta} L_{tr}$$

Figure 46. Equation. Volume of shaft reinforcement for rectangular columns – expanded equation.

The value of VOL_s can be minimized by differentiating with respect to θ and setting the result to zero. This leads to the equation in figure 47.

$$VOL_{s,min} = 2A_l\left(l_s + \sqrt{2eL_{tr}\frac{f_{ul}}{f_{yt}}}\right)$$

Figure 47. Equation. Minimum volume of shaft reinforcement for rectangular columns.

The inclination angle of the concrete strut can be determined using the equation in figure 48.

$$\tan\theta = \sqrt{\frac{L_{tr}}{2e}\frac{f_{ul}}{f_{yt}}} \qquad with\ \theta \in (0°, 90°)$$

Figure 48. Equation. Inclination angle of the concrete strut.

The relationship of the total volume of steel used in the splice, VOL_s, and the inclination angle of the strut, θ, are illustrated in figure 49 using the nominal properties of the splice in the test specimens:

- f_{ul} = 90 ksi
- f_{yt} = 60 ksi
- A_l = 10 x 0.31 = 3.1 in^2
- l_s = 22 in.
- e = 4 in.
- L_{tr} = 26 in.

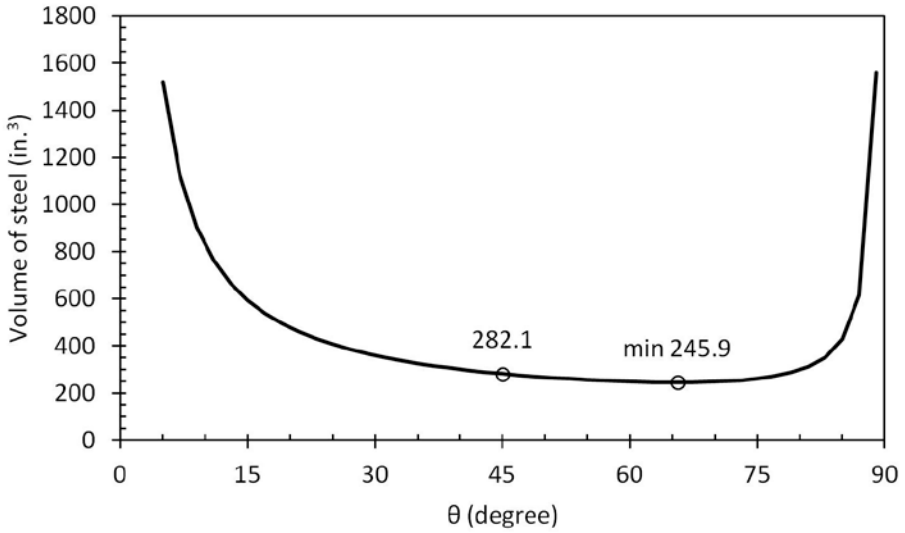

Figure 49. Graph. Relationship between the total steel volume in a splice and the inclined angle of struts.

At θ = 45°, the volume of steel in the splice is calculated as follows:

$$V_{s,45} = 2A_l\left(l_s + e + \frac{L_{tr}}{2}\frac{f_{ul}}{f_{tr}}\right) = 282.1\ in.^3$$

$$V_{s,min} = 245.9\ in^3 \quad at \quad \theta = 65.6°$$

$$\frac{V_{s,45}}{V_{s,min}} = \frac{282.1}{245.9} = 1.15$$

This analysis and the graph in figure 49 show that the minimum is very flat; even quite a large change in θ makes little difference to the total steel volume.

The foregoing model of a non-contact splice is two-dimensional and applies to rectangular tied columns. For a circular column, a three-dimensional model is needed. Such a model is illustrated in figure 50. It, too, is taken from MacLean and Smith, and it addresses loading in pure tension, rather than in bending.[18]

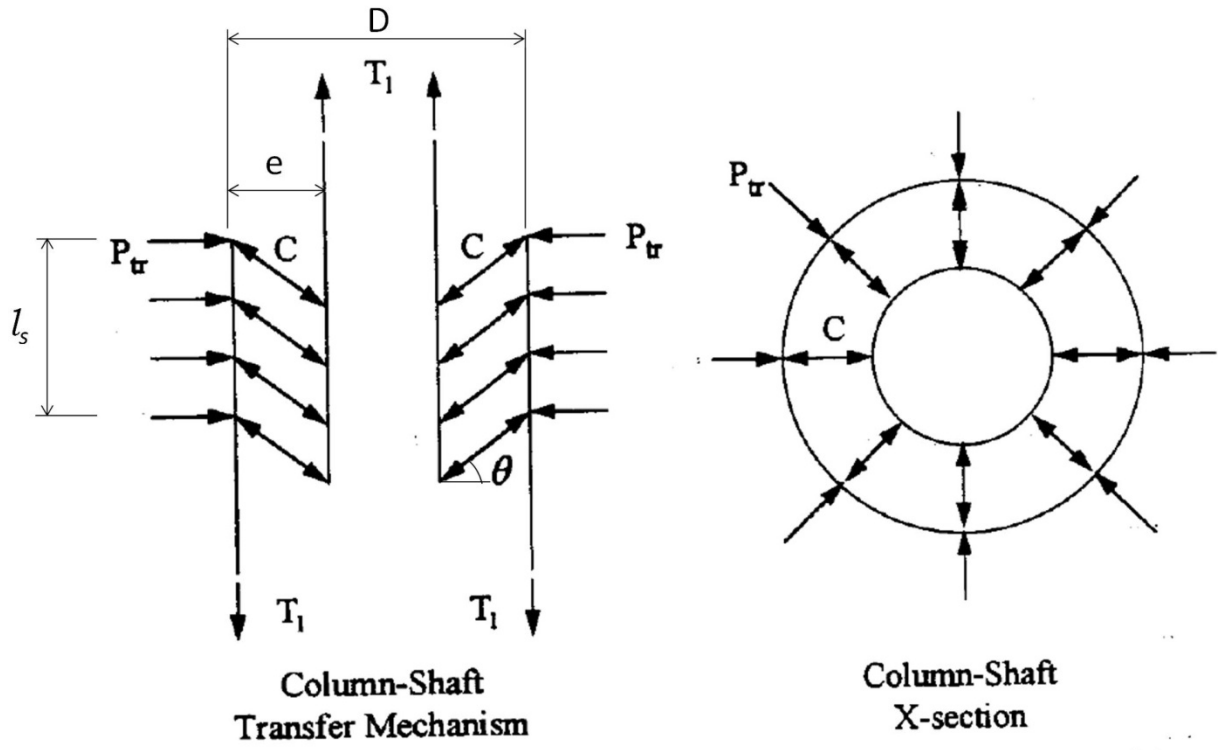

Figure 50. Diagrams. Proposed three-dimensional behavioral model for non-contact lap splices.[18]

The area of spiral reinforcement required in the transition region of the column-to-shaft connection, to fully develop the column reinforcing bars, is determined as shown in figure 51.

$$\frac{A_{tr}}{s_{tr}} = \frac{A_l f_{ul}}{2\pi f_{yt} l_s \tan\theta}$$

Figure 51. Equation. Shaft transverse reinforcement for circular columns.

The total volume of steel used in the splice, including both longitudinal and transverse steel, is determined as shown in figure 52.

$$VOL_s = 2A_l l_{ns} + \frac{A_{tr} l_s}{s_{tr}} \pi D$$

Figure 52. Equation. Volume of shaft reinforcement for circular columns.

Substituting figure 51 into figure 52 results in the equation shown in figure 53.

$$VOL_s = 2A_l(l_s + e.\tan\theta) + \frac{A_l f_{ul}}{f_{yt}\tan\theta}\frac{D}{2}$$

Figure 53. Equation. Volume of shaft reinforcement for circular columns – expanded equation.

In figure 53:

D = diameter of shaft spiral (in.).

The minimum steel volume VOL_s is given by the equation in figure 54.

$$VOL_{s,min} = 2A_l\left(l_s + \sqrt{eD\frac{f_{ul}}{f_{yt}}}\right)$$

Figure 54. Equation. Minimum volume of shaft reinforcement for circular columns.

The inclination angle of the concrete strut can be determined using the equation in figure 55.

$$\tan\theta = \sqrt{\frac{D}{e}\frac{f_{ul}}{f_{yt}}} \qquad with\ \theta \in (0°, 90°)$$

Figure 55. Equation. Inclination angle of the concrete strut.

Using the nominal properties listed earlier, and D = 26 in., θ becomes θ_{min} = 57.4°. At θ = 45° the volume of steel in the splice is calculated as follows:

$$VOL_{s,45} = 221.7\ in^3$$

$$VOL_{s,min} = 213.8\ in^3$$

$$\frac{VOL_{s,45}}{VOL_{s,min}} = \frac{221.7}{213.8} = 1.04$$

The three-dimensional model was developed for a column in pure tension, in which all the bars are subjected to equal tension stress. In a column subjected to combined compression and bending, only some of the bars are in tension. Therefore, WSDOT modified the model before including in in the BDM, to the equation shown in figure 56.

$$\frac{A_{tr}}{s_{tr,max}} = \frac{kA_l f_{ul}}{2\pi f_{yt} l_s}$$

Figure 56. Equation. Shaft transverse reinforcement for circular columns under axial load and bending.

In figure 56, *k* is a factor representing the ratio of column tensile reinforcement to total column reinforcement at the nominal resistance. The ratio is to be determined from column moment-curvature analysis or, as a default, taken as $k = 0.5$.

The length of the splices in specimens DS-1 and DS-2 was chosen as 28 inches. The spiral used in the splices was designed using the equation in figure 56 in specimen DS-1, and it was reduced by half in specimen DS-2. However, the measured strains from the gauges on the spirals of specimen DS-1 showed that the spirals at mid-height and the bottom of the transition region experienced almost no stress. Most of the transverse strain was concentrated in the top part of the transition region. In specimen DS-2 the spiral strain was much larger at the top and almost zero at the bottom. These data are inconsistent with the model predictions using the equation from McLean and Smith, because the model assumes that the spirals are fully stressed over the entire length of the splice.[18]

COLUMN MOMENT-CURVATURE ANALYSIS

To develop a method for column-shaft connection design, the distribution of longitudinal bar stresses round the column was needed. It was found using moment-curvature analysis. The validity of the analysis was confirmed by comparing the predicted and measured moments. Moment-curvature analysis was conducted using an in-house University of Washington program.[22] Two analyses were conducted, each with different material properties, and compared with test data from specimen DS-1.

The concrete model used in the program is based on the one proposed Kent and Park and is illustrated in figure 57.[15] Note that tension stress and tension strain are positive. It consists of a parabolic rising curve, followed by a linear falling segment, then a constant stress extending to infinite strain. In the program, the initial parabolic curve is replaced by a cubic, which allows the user to specify E_{c0}, ϵ_{c0} and f'_c independently. It defaults to the original parabolic curve if E_{c0} is chosen to be $f'_c/(2\,\epsilon_{co})$. The strain at peak stress, $\epsilon_{cc} = 0.002$. However, here the values of the confined concrete strength, $f_{cc} = 8$ ksi, and the ultimate compression strain, ϵ_{cu}=0.009, were generated from the properties of the confinement reinforcement using Mander's formula, rather than using the values recommended by Kent and Park.[16,17]

The steel model in the program contains three regions: elastic region, a yield plateau, and a curved strain-hardening region. In the first analysis, the expected steel reinforcement properties were used, in accordance with the AASHTO Seismic Guide Specifications.[13] These recommendations ($f_y = 68$ ksi; $\epsilon_{sh} = 0.015$; $f_u = 95$ ksi) are based on data collected by Caltrans.[23] The steel properties in the second analysis were based on the measured reinforcement properties for these tests ($f_y = 68$ ksi; $\epsilon_{sh} = 0.0027$; $f_u = 106$ ksi). The stress-strain curves for the reinforcing steel and concrete, and resulting moment-curvature relationships, are shown in figure 57 and 58. The flexural strengths from the two analyses and specimen DS-1 are shown in table 8.

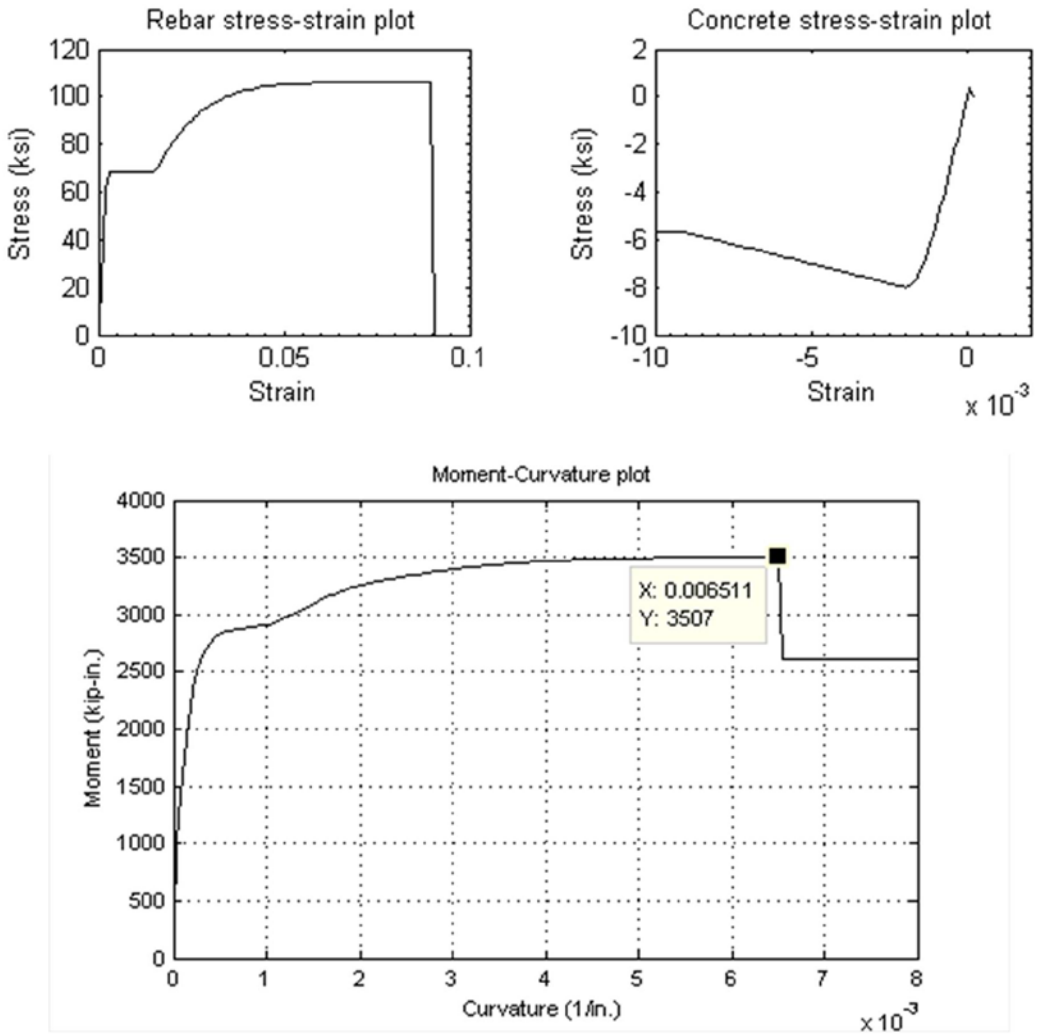

Figure 57. Graph. Moment-curvature analysis (based on expected material properties).

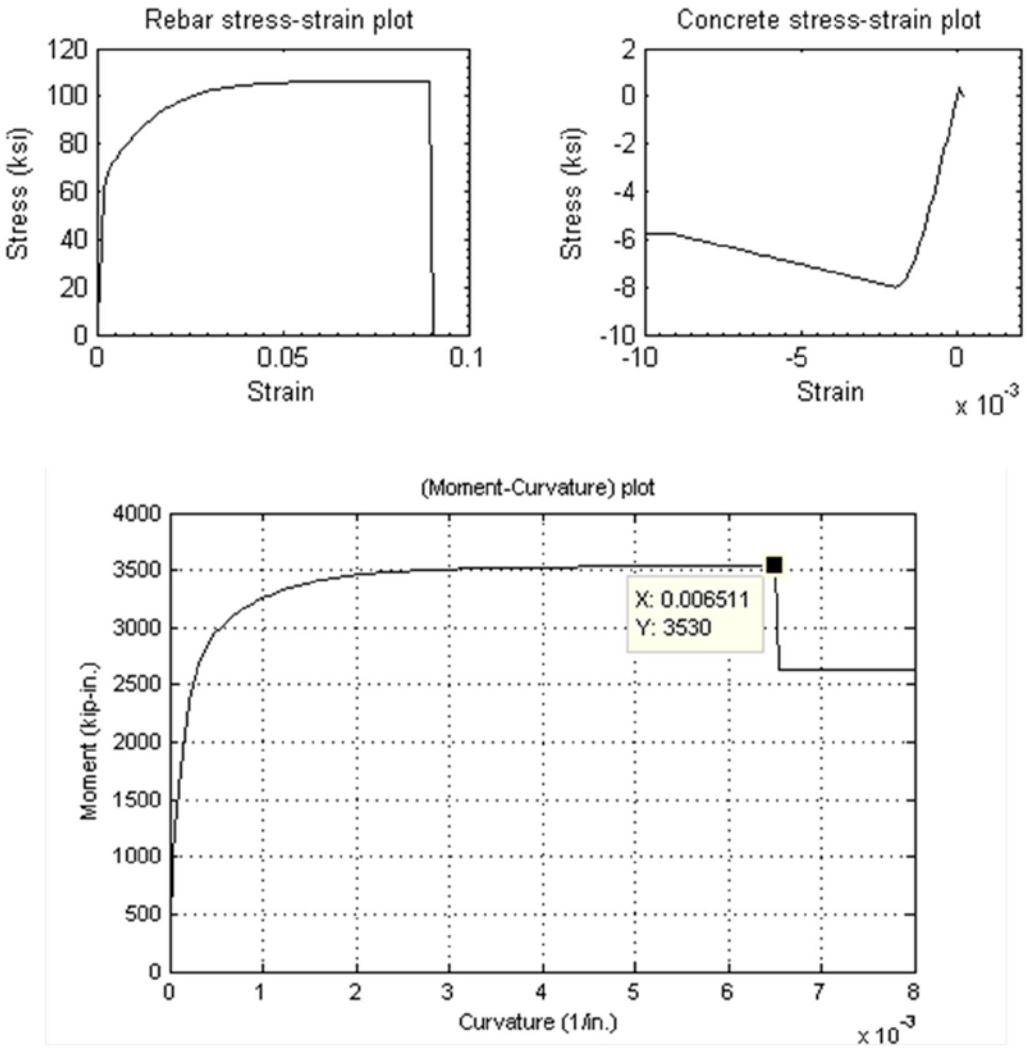

Figure 58. Graph. Moment-curvature analysis (based on measured material properties).

Table 8. Comparision of peak column moment.

Analysis 1 (Expected Properties) (kip-in.)	**Analysis 2 (Measured Properties) (kip-in.)**	**Measured (Specimen DS-1) (kip-in.)**
3507	3530	3476

The moments predicted by both analyses are close to the measured peak moment. These results suggest that the differences in longitudinal reinforcement properties do not affect the flexural strength of the column. Both analyses give the ultimate flexural strength at the curvature value of 0.0065. However, when curvature increases from about 0.0005 to 0.002, the moments in the two analyses are different. This occurs because, at those curvatures, the reinforcement strain in analysis 1 reaches the yield plateau region, whereas the reinforcement strain in analysis 2 starts going to the strain-hardening region. Thus, the tension force in reinforcement in analysis 2 is

larger than in analysis 1, so the moment in analysis 2 is higher. Later, when the reinforcement strain reaches the fracture point, the difference in stress between in analysis 1 and analysis 2 is small. Therefore, the moments of column are equal in both analyses.

Figures 59 and 60 show a plot of moment vs. strain in the extreme tensile reinforcement, and they show the measured values for specimens DS-1 and DS-2 and the values predicted by the moment-curvature analyses. The curves were plotted up to the peak strain measured in the tests, of about 0.011. (At larger strains, the gauges continued to read but the data acquisition system saturated and simply displayed the saturation strain.) All curves include two regions: an elastic region and a curved post-yield region.

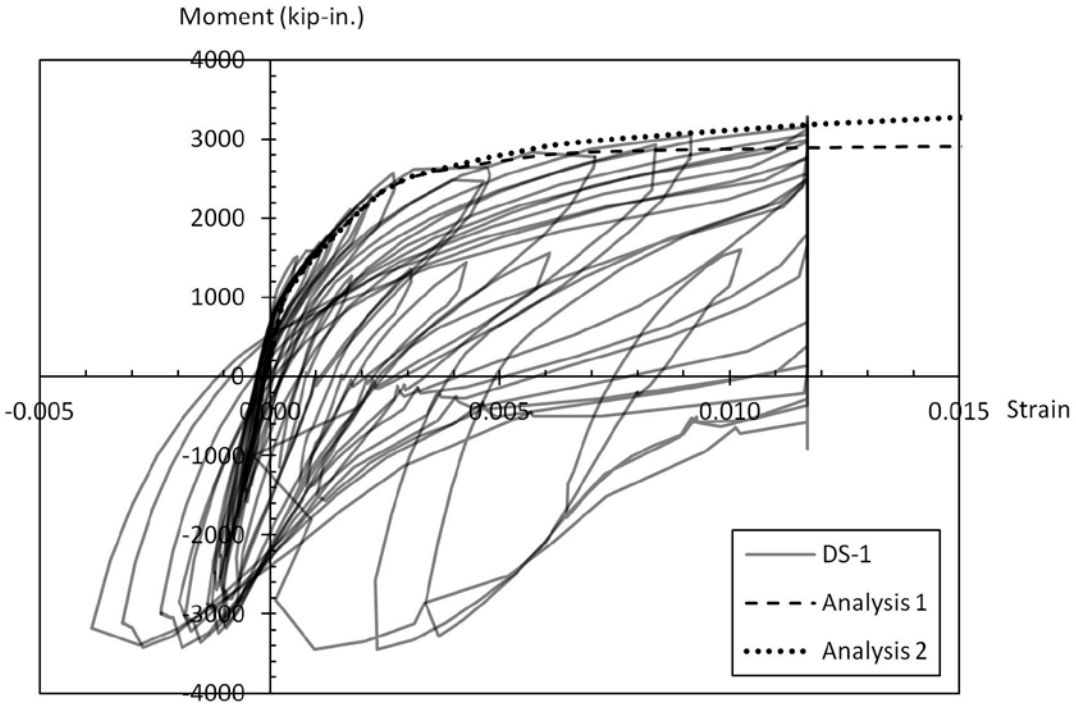

Figure 59. Graph. Moment-extreme reinforcement tensile strain relationship for column (in specimen DS-1).

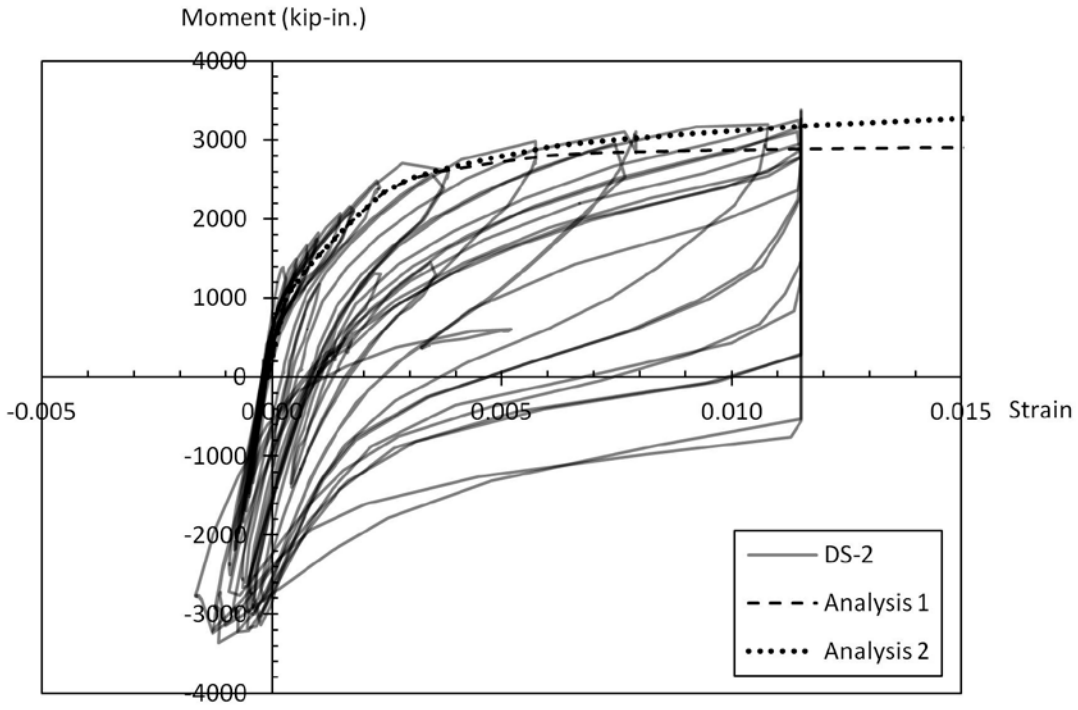

Figure 60. Graph. Moment-extreme reinforcement tensile strain relationship for column (in specimen DS-2).

The measured moments for a given strain in both specimens DS-1 and DS-2 are remarkably similar to the ones predicted in analysis 2, which used measured reinforcement properties. The moments in the post-yield region in analysis 1, using expected reinforcement properties, are smaller than the measured ones. At a strain of 0.0115, the measured moment is approximately 10 percent higher than the predicted one in analysis 1. This discrepancy, as mentioned earlier, is because of the yield plateau region of the expected steel model. In the confined concrete model, the strain at peak stress, ϵ_{cc} is given as 0.002 instead of 0.0034 as in Mander's formula. If Mander's formula is used here, the predicted moments in the yield region in analysis 1 and 2 are approximately 10 percent and 20 percent smaller than the measured ones, respectively. It suggests that Mander's confined concrete model is inconsistent with the tests on specimens DS-1 and DS-2.

The shaft longitudinal reinforcement strain was smaller than 0.002 during the testing, so the shaft remained elastic. Figure 61 shows the relationship between moment at the base of the shaft and tensile strain in the extreme longitudinal reinforcement in the shaft at three different levels. The figure includes measured data from specimens DS-1 and DS-2 and moments predicted using measured material properties and strains at the bottom of the shaft. The analysis is comparable to analysis 2 for the column but used the shaft geometry. Note that the jump in the predicted curve at about 2,400 kip-in. indicates first cracking.

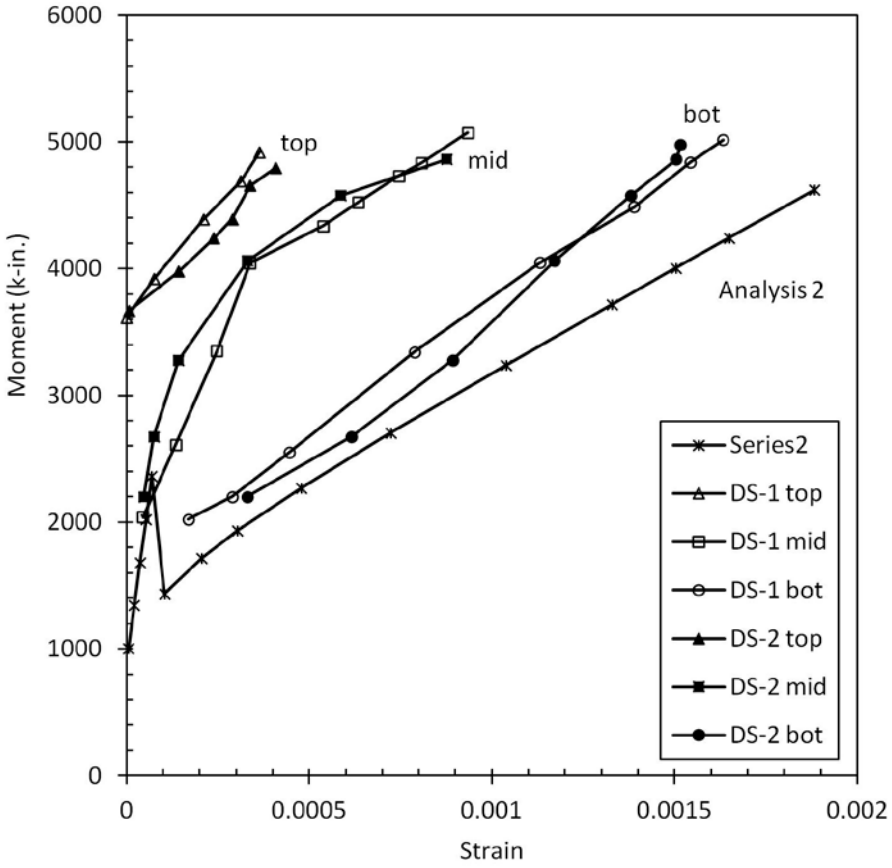

Figure 61. Graph. Relationship of moment at the base and extreme reinforcement tensile strain for the shaft.

Several features are evident.

For a given moment at the base of the shaft, the strains in the longitudinal shaft bars are the largest at the bottom and smallest at the top. This is as expected because it follows the trend of the moment diagram.

The measured strains from specimens DS-1 and DS-2 are remarkably similar. This similarity reflects the fact that, early in the load sequence, the load-deflection curves of the two specimens were similar.

The measured strains are smaller than the predicted ones. This is the opposite of what might be expected, for several reasons. First, application of a strain gauge involves some grinding and sanding of the bar, which inevitably reduces its area. For a given bar force, the measured strain is therefore likely to be higher than that obtained by dividing the nominal stress by *E*. Second, reinforcing bars tend to have areas that are, on average, less than the nominal value, but they have a higher true f_y to compensate. However, because the Young's modulus is essentially unchanged, this tendency should be expected to lead to measured strains that are, again, higher than those predicted from the nominal material properties. Last, the bars are elastic, so increases in the yield strength cannot explain the difference.

THE STRUT-AND-TIE MODEL AND SHAFT SPIRAL DESIGN

The geometry of the transition region defines it as a "disturbed region" in which Engineering Beam Theory is not applicable. Other methods, such as the strut-and-tie method, must be used to model the behavior of the column-shaft connection. Schlaich and Schäfer proposed two models for a socket footing.[24] One has smooth surfaces, and the other has rough surfaces between the column and the walls of the socket (see figure 62).

For the geometry used in specimens DS-1 and DS-2, the model for the column-shaft connection with a smooth surface leads to a horizontal force T_2 of approximately150 kips when V = 50 kips, and an additional tensile force T_4 of approximately 100 kips at the bottom of the transition. To resist these forces, 55 turns of spiral of the size used in the tests would be needed at the top and 36 turns at the bottom of the transition, whereas specimen DS-1 had a total of 24 turns and specimen DS-2 had 12. Thus, when the specimens reached their peak loads, the distribution of internal forces cannot have been the same as in the smooth surface model. However, at the very end of the specimen DS-2 test, when contact between the column surface and shaft surface was lost and friction was no longer possible, the specimen is believed to have behaved like the smooth surface model. At that stage, the loads were much smaller, and the low capacity of the spiral was consistent with the low load.

In the tests on specimen DS-1, no vertical slip at the interface was observed. The tie forces in the test were much smaller than those needed for the smooth model. Thus, the rough surface model for the column-shaft connection appears to be more consistent with the observed behavior. However, Schlaich and Schäfer's model is for a two-dimensional system, so it was necessary to perform a three-dimensional analysis for the circular column used in the tests. Figure 63 illustrates the model.

The column contained 10 No. 5 bars and the shaft contained 30 pairs of No. 3 bars. Thus, the tension force, T, in any column bar is assumed to transfer to the three nearest bar pairs of shaft reinforcement, as indicated in figure 64. The angle of inclination between struts C_1 and C_3 and the horizontal is taken to be θ. To simplify the analysis, the longitudinal reinforcement in the column and shaft was assumed to be distributed continuously round the perimeter, rather than as discrete bars, and the strut C_1 directions are radial, as shown in figure 65. The horizontal component of the strut force C_1 is $T_1/tan\,\theta$, and this is therefore the radial force per unit length applied to the shaft spiral. The distribution of tension T_1 in the shaft longitudinal bars is calculated by using the proposed moment-curvature analysis.

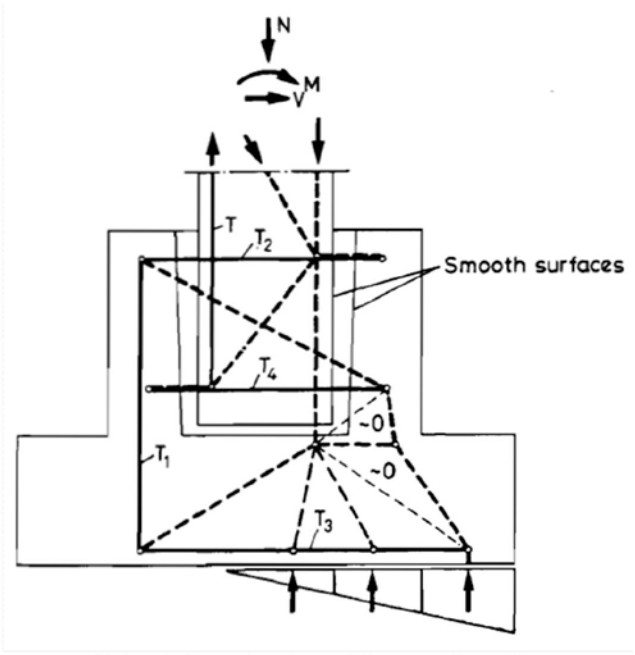

a)Model for a footing with smooth surfaces

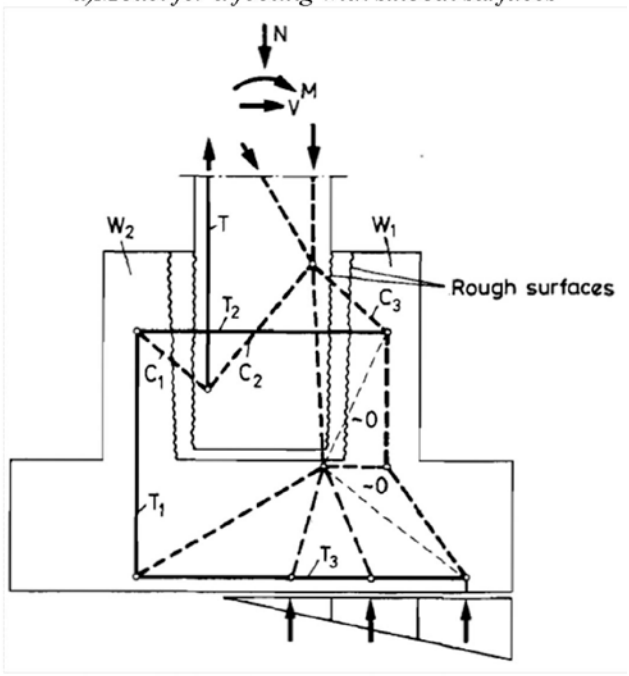

b)Model for a footing with rough surfaces

Figure 62. Diagram. Strut-and-tie model proposed by Schlaich and Schäfer.[(24)]

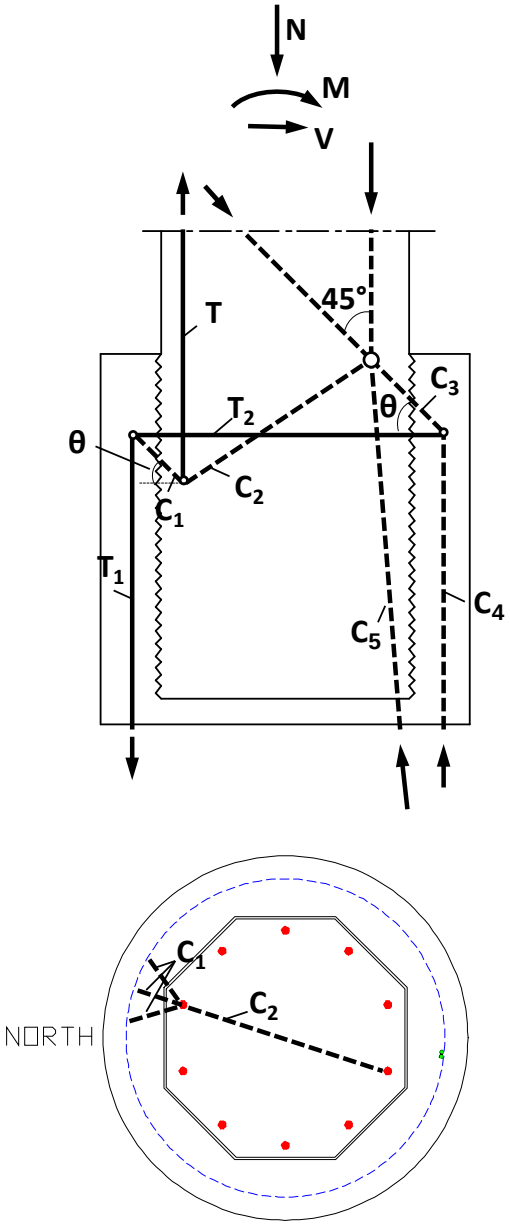

Figure 63. Diagrams. Elevation and plan of the strut-and-tie model for transmitting load from one column reinforcing bar to the three nearest shaft bundles bars.

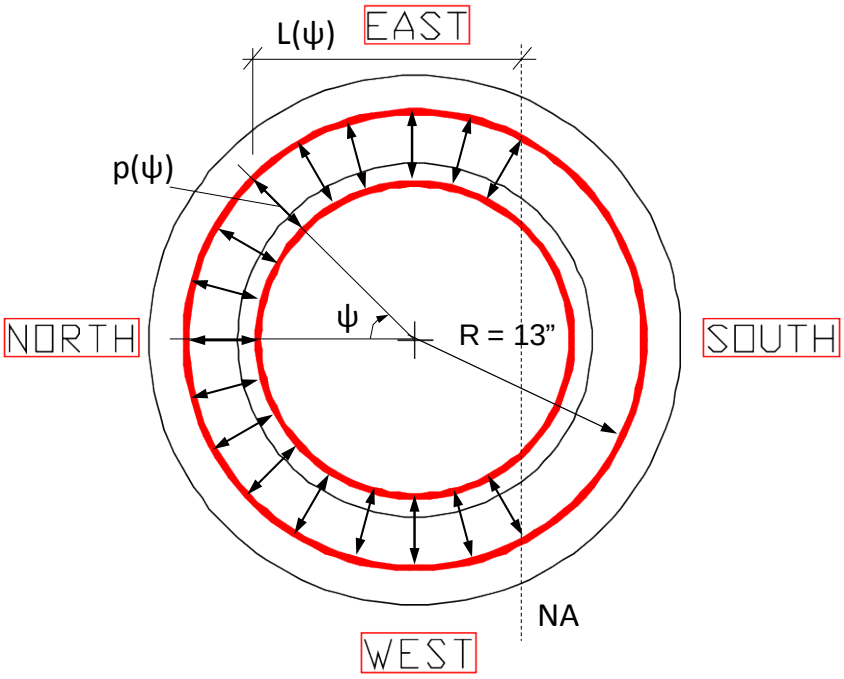

Figure 64. Diagram. Tension transfer from column to shaft longitudinal reinforcement.

As indicated in figure 64, the distributed load, p, applied around the circumference of the shaft spiral is given by the equation in figure 65.

$$p(\psi) = \frac{T_1(\psi)}{\tan\theta}$$

Figure 65. Equation. Distributed load determination.

The distribution of tension in the shaft reinforcement is obtained using the equation in figure 66.

$$T_1(\psi) = \frac{A_{l,sh}}{2\pi R} E_s \Phi L(\psi)$$

Figure 66. Equation. Distribution of tension in the shaft reinforcement.

In figure 66:

$A_{l,sh}$ = total area of longitudinal shaft reinforcement (in.^{2}).

f_s = tensile stress in shaft reinforcement (ksi).

ϵ_s = tensile strain in shaft reinforcement.

$L(\psi)$ = distance from the neutral axis to the tension longitudinal reinforcement.

E_s = modulus of elasticity of reinforcement (ksi).

R = radius of shaft spiral (in.).

Φ = curvature (1/in.).

ψ = angular coordinate (rad).

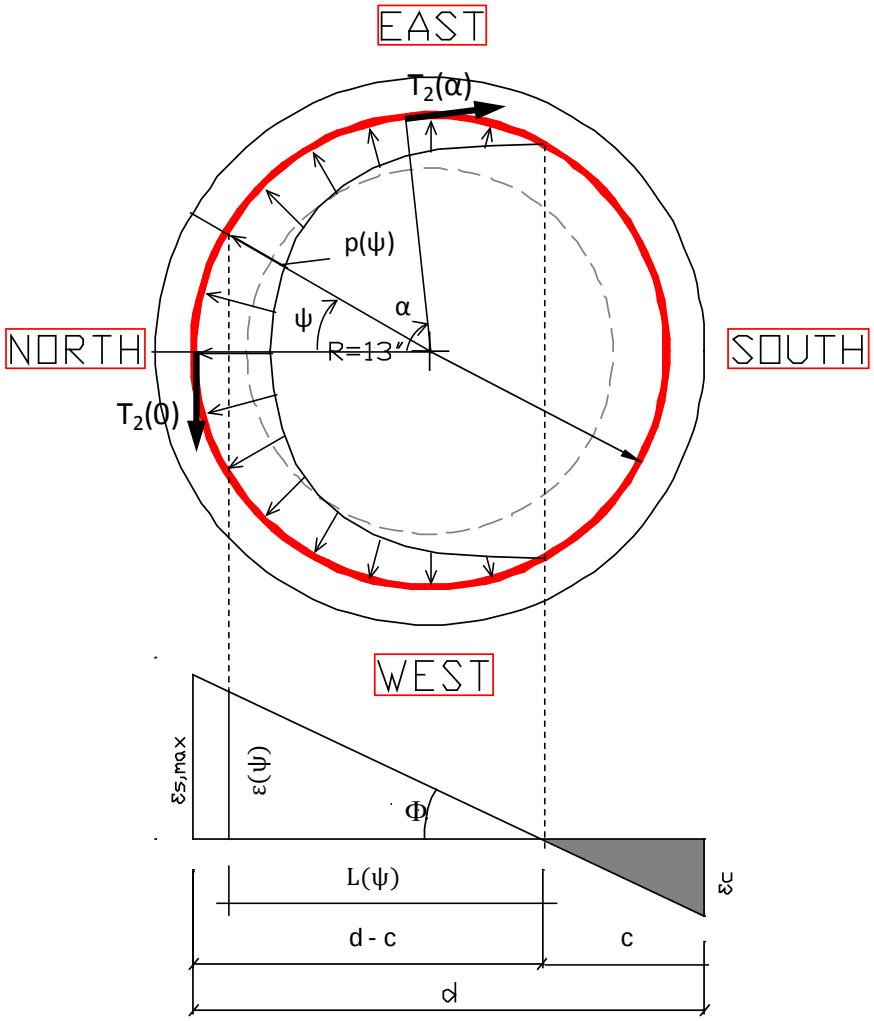

Figure 67. Diagram. Distributed load applied to shaft spirals.

From the strain distribution in figure 67, we have:

$$L(\psi) = (d - c) - R(1 - \cos\psi)$$

Figure 68. Equation. Distance of tensile forces from the neutral axis.

In figure 68:

d = distance from the extreme compression fiber to the extreme tension longitudinal reinforcement.

c = depth to the neutral axis.

Substituting $L(\psi)$ in the equation in figure 67 results in the equation shown in figure 69.

$$T_1(\psi) = \frac{A_{l,sh}}{2\pi} E_s \Phi . \left[\frac{(d - c)}{R} - (1 - \cos\psi)\right]$$

Figure 69. Equation. Distribution of tension in the shaft longitudinal reinforcement.

Substituting $T_1(\psi)$ in the equation in figure 65 results in the equation shown in figure 70.

$$p(\psi) = \frac{\Phi A_{l,sh} E_s}{2\pi \tan\theta} . \left[\frac{(d - c)}{R} - (1 - \cos\psi)\right]$$

Figure 70. Equation. Distributed load applied to the shaft transverse reinforcement.

Summing the north-south horizontal forces leads to the equation shown in figure 71.

$$\sin(\alpha) . T_2(\alpha) = \int_0^{\alpha} R . p(\psi) . \cos\psi . d\psi$$

Figure 71. Equation. Equilibrium equation.

In figure 71, α is an angular coordinate measured from the north.

Substituting figure 70 in figure 71 yields the equation shown in figure 72.

$$T_2(\alpha) = \frac{R\Phi A_{l,sh} E_s}{2\pi \tan\theta} \left[\frac{(d - c) - R}{R} + \left(\frac{\cos\alpha}{2} + \frac{\alpha}{2\sin\alpha}\right)\right]$$

Figure 72. Equation. Distribution of tensile force in the shaft spirals.

The parameters used in the tests were as follows:

- R = 13 in.

- A_l = 30*0.22 = 6.6 in.^{2}
- E_s = 29000 ksi
- d = 28 in.
- c = 9 in.

If θ is assumed to be 45 degrees, and the curvature is taken when the predicted moment is equal to the peak measured moment (Φ = 106.11 e-6 in.$^{-1}$), the distribution of the tensile force, T_2, in the shaft spirals is shown in figure 73.

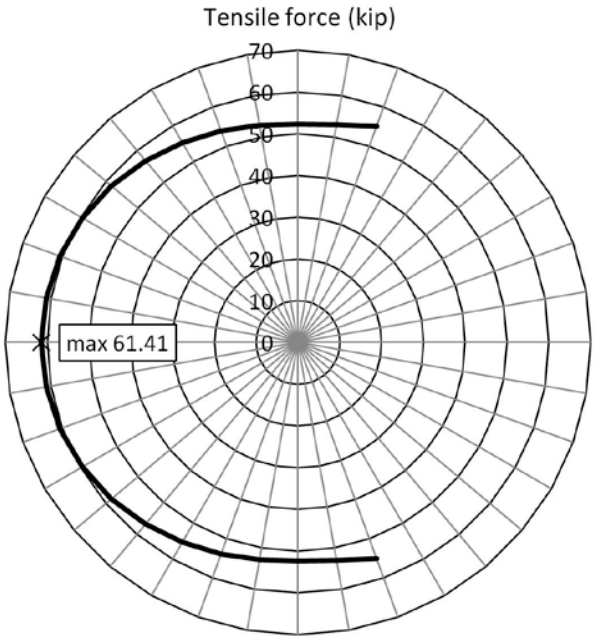

Figure 73. Diagram. Tensile force distribution in tie T_2 in tension area.

The maximum tensile force in the tie, T_2, occurs at α = 0.0, and is calculated using the equation in figure 74.

$$T_{2,max} = \frac{\Phi A_{l,sh} E_s}{2\pi \tan\theta}(d - c)$$

Figure 74. Equation. Maximum tensile force in the tie.

The relationship between the maximum spiral force, $T_{2,max}$, and the assumed strut inclination angle, θ, is shown in figure 75. As might be expected, steeper strut angles lead to lower spiral forces.

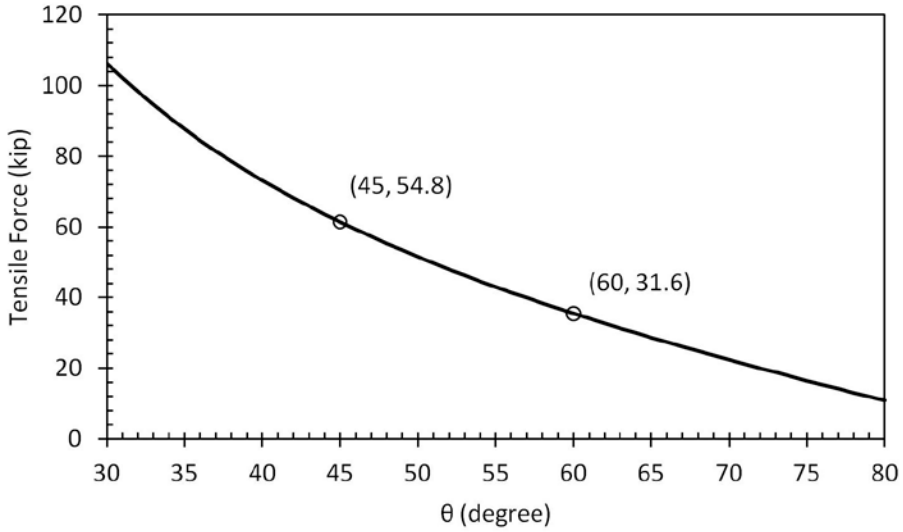

Figure 75. Graph. Relationship of T_{2max} vs. θ.

The strut angle can be estimated by equating the spiral capacity and demand. The yield strength of a single spiral wire is calculated as shown in figure 76.

$$f_{yt}A_{tr} = 80 \times \left(\pi \times \frac{0.148^2}{4}\right) = 1.376\ k/wire$$

Figure 76. Equation. Yield strength of a single spiral wire.

If all 24 turns of the spiral in specimen DS-1 were to be active in the load transfer, the total spiral capacity would be 24*1.376 = 33.0 kips, for which figure 75 shows a corresponding strut angle of 62 degrees. However, the measured strains in specimen DS-1 showed that only the spiral in the top of the transition region was stressed significantly. If only the spiral at the 15-inch upper transition (i.e., 16 turns) was active, the force would have been 22.0 kips and the angle close to 70 degrees. The assumed 16 active spirals is probably too high, given the strain distribution in the spiral. However if less spiral is assumed to be active, the strut angle becomes steeper. This 70-degree angle is sufficiently steep that it is improbable, both because the space for such a strut is not available and because it implies a low ratio of radial force to shear force being transferred across the column-to-shaft interface. The latter implies a friction coefficient significantly greater than 1.0.

In fact, the concrete may have provided some of the hoop tension force. If the concrete surrounding each spiral is taken into account, and the concrete width is taken as the thickness of the concrete annulus outside column, 5 inches, the strength of the surrounding concrete per unit length is calculated as follows:

$$f_r A_c = 0.63 \times (5 \times 1) = 3.15 \text{ kips/in.}$$

where:

f_r = concrete modulus of rupture.

$= \quad 7.5\sqrt{f_c'} = (7.5\sqrt{7000})/1000 = 0.63$ ksi.

If the strut angle is taken as $\theta = 45$ degrees, which implies a friction coefficient equal to 1.0, figure 75 shows a maximum tensile force of 54.8 kips. At the upper transition, the strength of the spirals is 22 kips, as mentioned above. Thus, the necessary length of concrete is calculated as follows:

$$l = \frac{54.8 - 22}{3.15} = 10.4 \text{ in.}$$

The necessary length of concrete is smaller than the assumed length of upper transition (15 inches), so this assumption seems to be plausible. If the designers do not want to rely on the concrete tensile strength, they can increase the number of spirals 2.5 times to get a strength of 55 kips.

This suggests that the spiral was at yield stress (80 ksi, $\epsilon = 0.003$) at the upper transition while the concrete was still uncracked (f_r = 630 psi, $\epsilon = 0.630 / 5000 = 0.00012$) at the lower transition.

CHAPTER 7. SUMMARY AND CONCLUSIONS

SUMMARY

A new system is proposed for connecting drilled shafts to precast columns in bridge bents. It is adapted from the column-to-footing "socket" connection proposed for spread footing by Haraldsson, and it consists of embedding a precast column into the cast-in-place transition region of the drilled shaft.[10] The purpose is to facilitate rapid on-site construction through the use of prefabricated elements. The system is suitable for use in seismic regions.

Two drilled shaft specimens were fabricated and tested at the University of Washington. This section of the document summarizes the construction procedure, the design methodology, the test specimens and performance, and analytical models used to study the connection.

Construction Sequence

The field construction sequence is as follows:

1. A precast column is cast. The surface is roughened in the region where the column will be embedded in the cast-in-place drilled shaft.
2. The hole for the shaft is bored, the reinforcing cage is placed, and the shaft is cast up to the bottom of the transition region (approximately 10 feet below grade).
3. The precast column is positioned, leveled, and braced in the drilled shaft.
4. The transition region (approximately the top 10 feet of the shaft) is cast around the precast column.

Connection Design

A shaft and column system prototype was designed according to the AASHTO LRFD Bridge Design Specifications, AASHTO Seismic Guide Specifications, and the WSDOT BDM.[11,12,13] Reduced-scale test specimens were then developed from the prototype.

The prototype precast column was designed to have a reinforcement ratio of approximately 1 percent. The transverse reinforcement in the column was defined by requirements for shear and confinement of the concrete core.

The column longitudinal reinforcement was equipped with anchor heads, instead of using the conventional detail of bending the longitudinal bars outwards into the foundation. This configuration has several benefits. It reduces the development length of the reinforcement and, thus, indirectly reduces the embedment length of the column in the shaft. It has better seismic performance, because the force transfer between the column and shaft is more direct. This design also makes fabrication, transportation, and erection safer and easier.

The surface of the column was roughened where it was to be embedded in the drilled shaft. The details of the roughening were the same as those specified in the WSDOT BDM for roughening the ends of prestressed concrete girders. Load transfer at the interface was designed using the AASHTO LRFD shear-friction design procedure. In the embedded region, the column section

was an octagon, circumscribed within the circular section of the main column. This was done to facilitate the forming of the roughened surface, which used wooden strips.

The embedment length of the column in the drilled shaft was defined by requirements for splicing the shaft and column bars. The splice is by definition a non-contact splice, for which the WSDOT BDM provides design requirements. The column bars were larger than the shaft bars, so they would normally control the splice length.[5] However, the heads on the column bars improve their anchorage so that the shaft bars, which had no such heads, in fact controlled the splice length.

The shaft was designed as a capacity-protected element to ensure that the hinge would form in the column and not in the shaft. The scale of the system was chosen so that the ratio of shaft diameter/column diameter was as small as possible according to the WSDOT BDM, so that test specimens represented the most critical conditions. That choice led to a prototype system of a 6-foot-diameter column and a 9-foot-diameter shaft, which were represented at 28 percent scale in the laboratory specimens by a 20-inch-diameter column and a 30-inch-diameter shaft.

The shaft spiral was designed according to WSDOT BDM requirements for non-contact lap splices in conventional cast-in-place drilled shafts. The spiral was terminated by three turns of the spiral.

Test Specimens

Two test specimens were built. The scale factor (1/3.6, or 28 percent) was chosen to match the 20-inch-diameter of column specimens tested by previous researchers.[10,14]

The only difference between specimens DS-1 and DS-2 was the amount of spiral in the column-to-shaft transition region, which was reduced by half in DS-2. The goal was to promote failure in the shaft transition region in specimen DS-2, to develop an understanding of the load transfer mechanism there.

In both specimens, a cast-in-place base was built monolithically with the transition region to attach the specimen to the testing rig. The specimens were heavily instrumented.

Test Performance

Quasi-static, cyclic lateral load tests were performed to evaluate the seismic performance of the two specimens.

In each test, the specimen was subjected to a constant, unfactored axial dead load value of 159 kips, accompanied by a cyclic displacement-controlled lateral excitation. The displacement history was a modification of a loading history for precast structural walls recommended in NEHRP.[19]

The response and mode of failure of each specimen was the same as had been anticipated during design. Specimen DS-1 was controlled by column behavior. Failure occurred by plastic hinging in the column, while the connection region in the shaft remained largely undamaged. Testing was stopped when almost all the column longitudinal reinforcement had fractured. By contrast,

specimen DS-2 was dominated by deformations of the shaft. The failure mode was prying action of the shaft in the transition region. Testing was stopped when all the spiral reinforcement in the shaft had broken.

Response Data

The measured data included loads and displacements, deflection and rotation of column and shaft, strain in the column and shaft longitudinal reinforcement, and strain in the shaft spiral. The measured data confirmed the observed responses and modes of failure.

Analytical Model

Load transfer within the transition region was modeled using a three-dimensional strut-and-tie mechanism. This model is necessarily a simplification of the true behavior, but it provides reasonable agreement with the experimental results and helps to identify the probable load paths.

CONCLUSIONS

From the results obtained in these tests, the following conclusions can be drawn for the behavior of the column-to-shaft connection:

- Provision in the precast system of the amount of spiral reinforcement required for conventional drilled shafts of the same dimensions protects the shaft and causes failure to occur by plastic hinging of the precast column, as desired. Because the test specimens had the smallest possible shaft/column diameter ratio, and the shortest possible embedment length, this conclusion will hold for all permissible shaft and column combinations.
- Use of half of the conventional amount of shaft spiral causes failure to occur in the shaft, by prying action of the concrete shell surrounding the precast column. The test specimens contained no external confining steel shell. If one were used, it might provide some of the benefits of additional spiral and force the failure back into the column.
- Mechanical anchor heads are needed at the ends of the column longitudinal reinforcement to ensure hinging in the column without anchorage failure, especially if the large bar system proposed by Pang et al. is used.[5] The need for heads on the shaft bars is apparent from the strut-and-tie model, but it was not clear from the test results.
- The spiral at the very top of the shaft is subjected to high tension during lateral loading. The strut-and-tie model shows that the spiral resists prying failure of the shaft, and that conclusion is supported by the high strains recorded in the spiral in specimen DS-1 and the fractured spiral in specimen DS-2. However, the spiral was in both cases distributed uniformly up the transition region, with additional turns at the termination point at the top. Further testing is needed to determine whether a non-uniform distribution of the spiral, with the majority at the top, would provide better response.
- The WSDOT requirements for non-contact lap splices do not provide satisfactory agreement with the experimental results.
- Two questions are raised to obtain a consistent strut-and-tie model.

    - What is the value of inclined angle, θ, of struts which transfer tensile force from column reinforcement to shaft reinforcement? This value has a large effect on the amount of spirals required in the splice. A bigger value of θ leads to a smaller amount of spirals. However, the size of these struts is limited by the small space between the column reinforcement and shaft reinforcement. Thus, a large θ is not plausible.
    - What role, if any, does the tensile strength of the shaft concrete play in the confinement of the splices? It appears to have played an important role in the tests.
- If the tension strength of the shaft concrete is excluded, the analytical model shows that the amount of spiral steel must be increased by a factor of 2.5.

RECOMMENDATIONS FOR FURTHER RESEARCH

This study demonstrated the fundamental behavior of the column-to-shaft socket connection. However, further work is needed in the following areas:

- Two more tests are recommended to determine the optimal distribution of the transverse reinforcement at the top of the shaft. One test specimen should be the same as specimen DS-1 except that the shaft spiral should be anchored in such a way that additional spiral turns are not used. Welding is a possibility. The other test specimen should be designed with no distributed spiral in the shaft and a concentrated ring of spiral at the top of the shaft. If the first specimen fails in the shaft and the second one fails in the column, the top of the shaft will have been proven to be the optimal location for the spiral.
- Experiments should be conducted to determine the need for mechanical anchorages or hooks on the top of the longitudinal shaft bars. The strut-and-tie model suggests the need for anchorage devices of some struts, but the test specimens performed well without them.
- The WSDOT requirements for confinement of non-contact splices in drilled shafts should be re-examined. In particular, the *k*-factor of 0.5 should be evaluated critically.
- The contribution of the tensile strength of concrete in the confinement of non-contact splices should be examined. One test specimen should be the same as specimen DS-1 except that the transition concrete is separated in two parts. Two plastic pieces can be placed on the north side and the south side to isolate two parts of the transition concrete so the confinement would be based on only spirals.
- Experiments should be conducted to determine the three-dimensional force transfer mechanism between reinforcing bars in the splice. The bars should be heavily gauged. Based on the force transfer mechanism, a consistent value of inclination angle of the struts should be proposed for design.

ACKNOWLEDGEMENTS

A debt of gratitude is due to professors John F. Stanton and Marc O. Eberhard, for their inspiration, friendship and guidance. Thanks to Vietnamese Education Foundation (VEF) for giving me a great chance in my life. Thanks to my friends Todd Janes, Olafur Haraldsson, Bo-Shiuan Wang, Po-Chien Hsio, Patricia Clayton, and Tu Nguyen for making graduate school an enjoyable experience. Thanks to my family for always being so supportive and encouraging. Finally, thanks to my wife, Hang, for everything she has done for me, and I apologize for the many long nights and lost weekends.

REFERENCES

1. Matsumoto, E., Waggoner, M., Sumen, G., Kreger, M., Wood, S., and Breen, J. (2001). "Development of a Precast Bent Cap System," Center for Transportation Research, Research Project 0-1748, University of Texas at Austin.
2. Hieber, D.G., Wacker, J.M., Eberhard, M.O., and Stanton, J.F. (2005). *Precast Concrete Pier Systems for Rapid Construction of Bridges in Seismic Regions.* Washington State Department of Transportation Report WA-RD 611.1, Olympia, WA.
3. Hieber, D.G., Wacker, J.M., Eberhard, M.O., and Stanton, J.F. (2005) *State-of-the-Art Report on Precast Concrete Systems for Rapid Construction of Bridges.* Washington State Department of Transportation Report WA-RD 594.1, Olympia, WA.
4. Wacker, J.M, Hieber, D.G., Eberhard, M.O., and Stanton, J.F. (2005). *Design of Precast Concrete Piers for Rapid Construction in Seismic Regions*. Washington State Department of Transportation Report WA-RD 629, Olympia, WA.
5. Pang, J.B.K., Steuck, K.P., Cohagen, L.S., Eberhard, M.O., and Stanton, J.F. (2008). *Rapidly Constructible Large-Bar Precast Bridge-Bent Connection*. Washington State Department of Transportation Draft Report WA-RD 684.2, Olympia, WA.
6. Steuck, K.P., Pang, J.B.K., Eberhard, M.O., and Stanton, J.F. (2008). *Anchorage of Large-Diameter Reinforcing Bars Grouted into Ducts*. Washington State Department of Transportation Report WA-RD 684.1, Olympia, WA.
7. Steuck, K., Stanton, J.F., and Eberhard, M.O. (2009). "Anchorage of Large-Diameter Reinforcing Bars in Ducts," *ACI Structural Journal*, Vol. 106, No. 4, pp. 506-513.
8. Cohagen, L.S. Pang, J.B.K., Steuck, K.P., Eberhard, M.O., and Stanton, J.F. (2008). *A Precast Concrete Bridge Bent Designed to Re-center after an Earthquake.* Washington State Department of Transportation Report WA-RD 684.3, Olympia, WA.
9. Restrepo, J.I., Tobolski, M.J., and Matsumoto, E.E. (2011). *Development of a Precast Bent Cap System for Seismic Regions,* NCHRP Report 681. National Cooperative Highway Research Program, Transportation Research Board, Washington, DC.
10. Haraldsson, O. (2011). "Spread Footing Socket Connections for Precast Columns." Master's thesis, University of Washington, Seattle, WA.
11. WSDOT. (2012). *Bridge Design Manual (LRFD) M23-50.12.* Olympia, WA: Washintgon State Department of Transportation, Olympia, WA.
12. American Association of State Highway and Transportation Officials (AASHTO). (2009). *LRFD Bridge Design Specifications.* 4th ed., AASHTO, Washington, DC.
13. American Association of State Highway and Transportation Officials. (2009). *AASHTO Guide Specification for LRFD Seismic Bridge Design*. AASHTO, Washington DC.
14. Janes, T. (2011). "Precast Column Socket Connections for Thin Spread Footings." Master's thesis, University of Washington, Seattle, WA.
15. Kent, D.C., and Park, R. (1971). "Flexural Members with Confined Concrete," *Journal of the Structural Division, ASCE,* Vol. 97, No. 7, pp. 1969-1990.
16. Mander, J.B., Priestley, M.J.N., and Park, R. (1988). "Theoretical Stress-Strain Model for Confined Concrete," *Journal of the Structural Division, ASCE,* Vol. 114, No. 8, pp. 1804-1826.
17. Priestley, M.J.N., Seible, F., and Calvi, G.M. (1996). *Seismic Design and Retrofit of Bridges.* John Wiley & Sons, Inc., Hoboken, NJ.

18. McLean, D.I., and Smith, C.L. (1997), *Noncontact Lab Splices in Bridge Column-Shaft Connections*, Washington State Department of Transportation Report WA-RD 417.1, Olympia, WA.
19. Building Seismic Safety Council for the FEMA. (2004). *NEHRP Recommended Provisions for Seismic Regulations and for New Buildings and Other Structures (FEMA 450).* Washington D.C.
20. Berry, M.P., and Eberhard, M.O. (2004). *PEER Structural Performance Database User's Manual.* Pacific Earthquake Engineering Research Center Report 2004, <www.ce.washington.edu/~peeral>, University of California, Berkeley, CA.
21. Brown, W. (2008). "Bar Buckling in Reinforced Concrete Bridge Columns." Master's Thesis, University of Washington, Seattle, WA.
22. Stanton, J.F. (2010). "Moment-Curvature Program," University of Washington, Seattle, WA.
23. Caltrans (2006). *Seismic Design Criteria Version 1.4*. Caltrans, Sacramento, CA.
24. Schlaich, J., and Schäfer, K. (1991). "Design and Detailing of Structural Concrete Using Strut-and-Tie Models," *The Structural Engineer*, Vol. 69, No. 6, pp. 113-125.

APPENDIX A: SPECIMEN CONSTRUCTION DRAWINGS

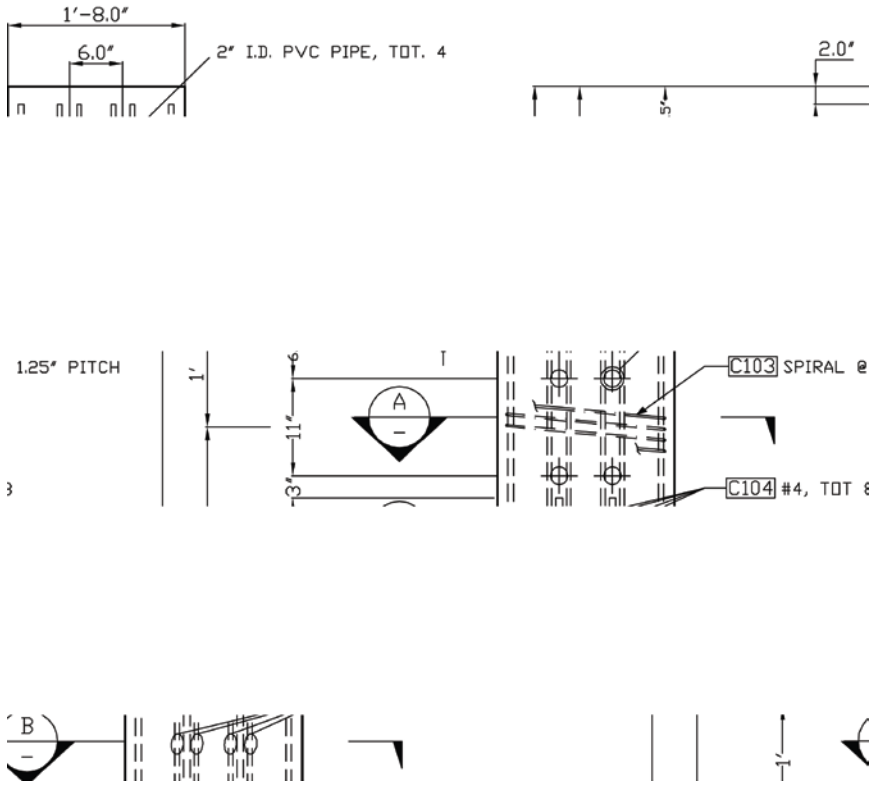

Figure 77. Diagram. Column elevation.

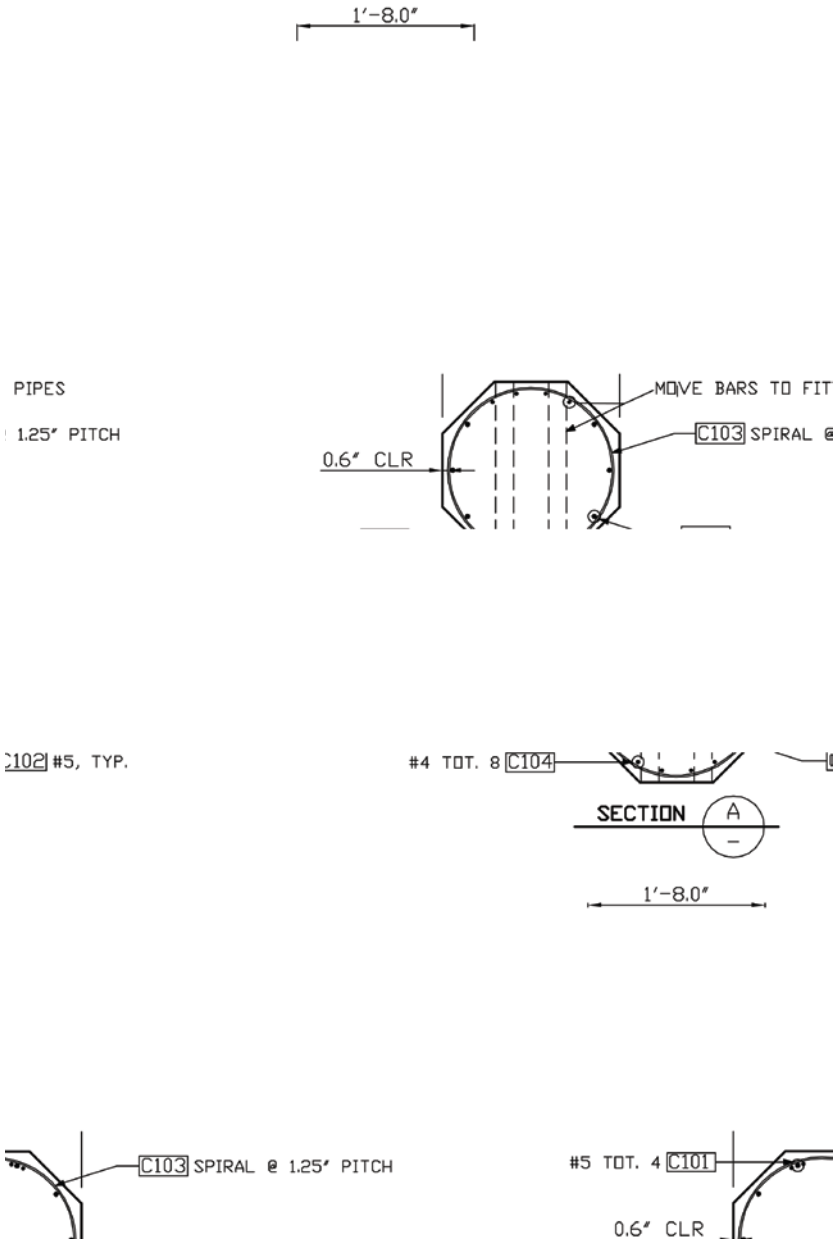

Figure 78. Diagram. Column sections.

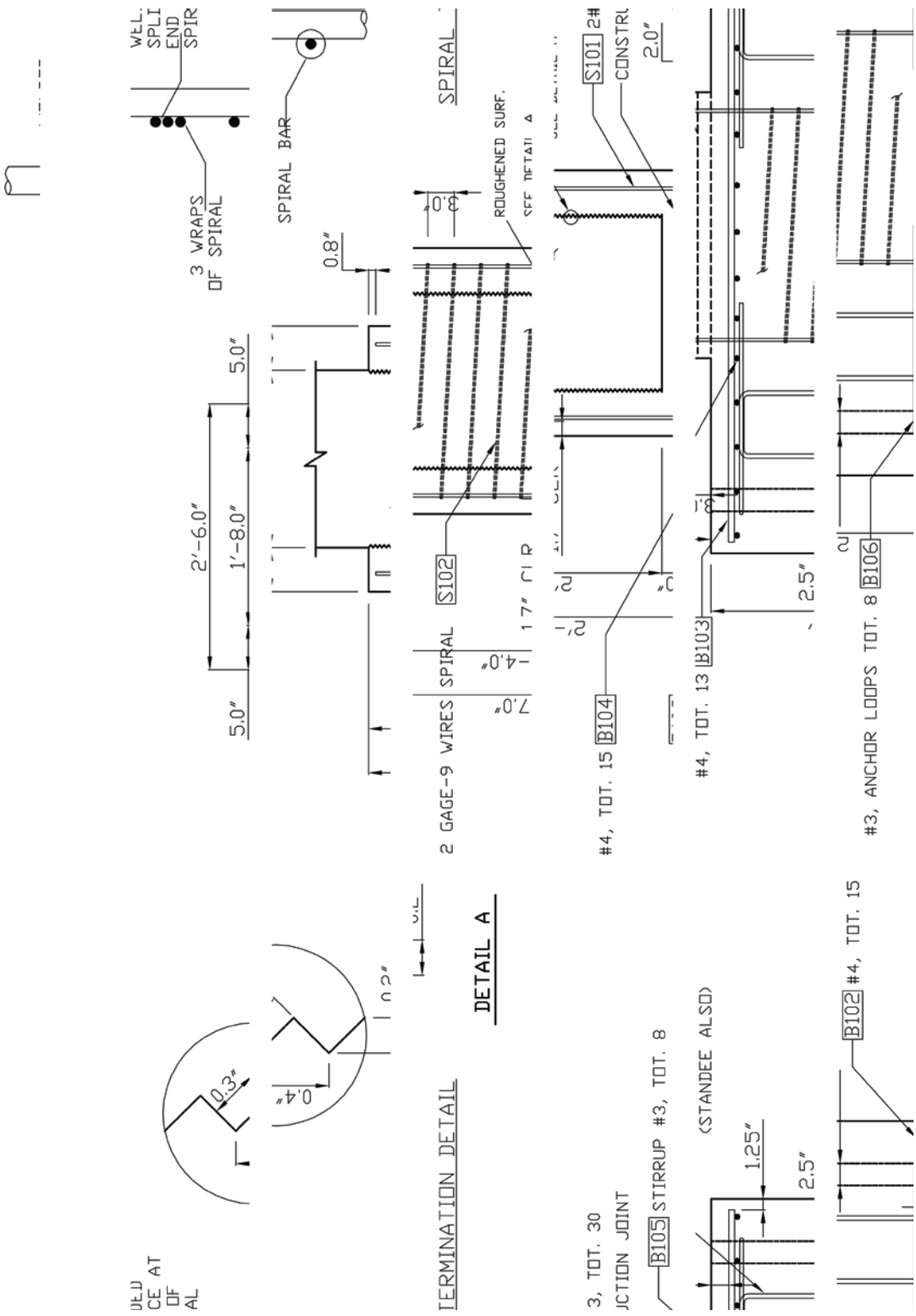

Figure 79. Diagram. Shaft and base – longitudinal section.

Figure 80. Diagram. Shaft and base – transverse section.

Figure 81. Diagram. Shaft and base reinforcement arrangement.

APPENDIX B: MATERIAL TESTS

CONCRETE STRENGTHS

Both specimen DS-1 and DS-2 used the common concrete mix with code 09468 provided by Calportland Company. The concrete design strength was 6,000 psi. It used 3/8-inch aggregate pea gravel and had a specified slump of 5 inches.

The concrete compressive strength at 7, 14, and 28 days are provided in the following table.

Table 9. Concrete strengths for specimen DS-1 and DS-2.

Time	7-Day (psi)	14-Day (psi)	28-Day (psi)	Day of Test (psi)
DS1 Column	5130	5820	6250	7770
DS1 Shaft	5320	6350	6600	7360
DS2 Column	4780	6350	6600	7170
DS2 Shaft	5270	5790	6400	6450

REINFORCEMENT

Reinforcement used in the footing and column conformed to ASTM standard 706. The column spiral used the three-gauge wire (0.244-inch diameter), which was the same as that used by Haraldsson and Janes.[10,14] The shaft spiral used the 9-gauge wire (0.148-inch diameter). All spirals conformed to ASTM A82.

The tension tests were performed using the MTS system machine, and the elongation was measured by an extensometer. The tension specimen was loaded slowly until the load reached its maximum and started decreasing. The extensometer was then removed to prevent damage to the equipment. The specimen was then loaded to failure, after which the length was measured to obtain a strain at failure.

Results of the tension tests for bars No. 3 and No. 5 are shown in figures 82 and 83. Because the spirals were too small and extensometer cannot be used to measure the elongation, only the ultimate stresses of spirals were found. These are reported in table 10.

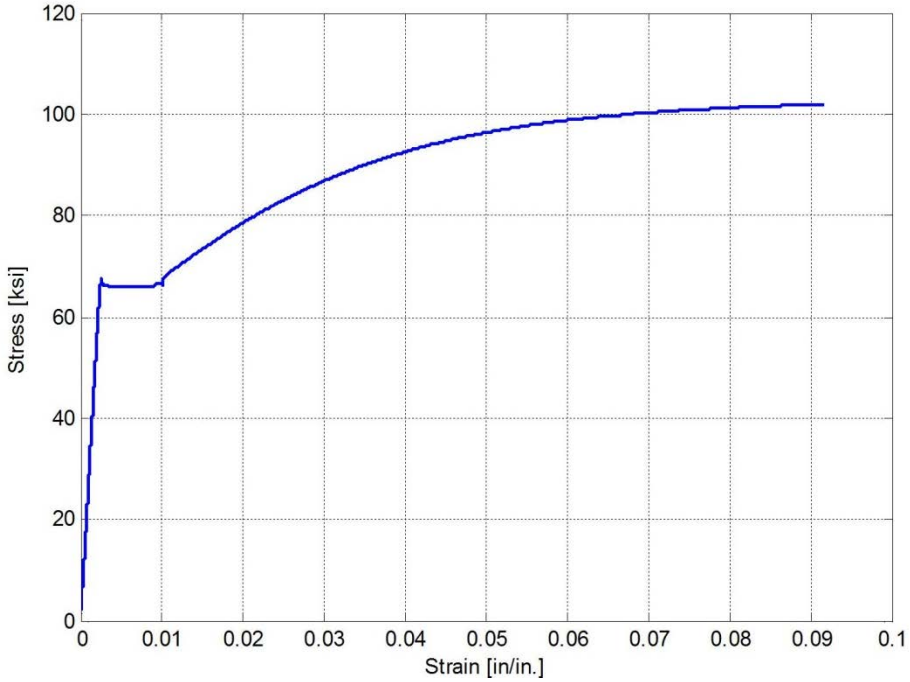

Figure 82. Graph. Stress-strain curve for No. 3 bar.

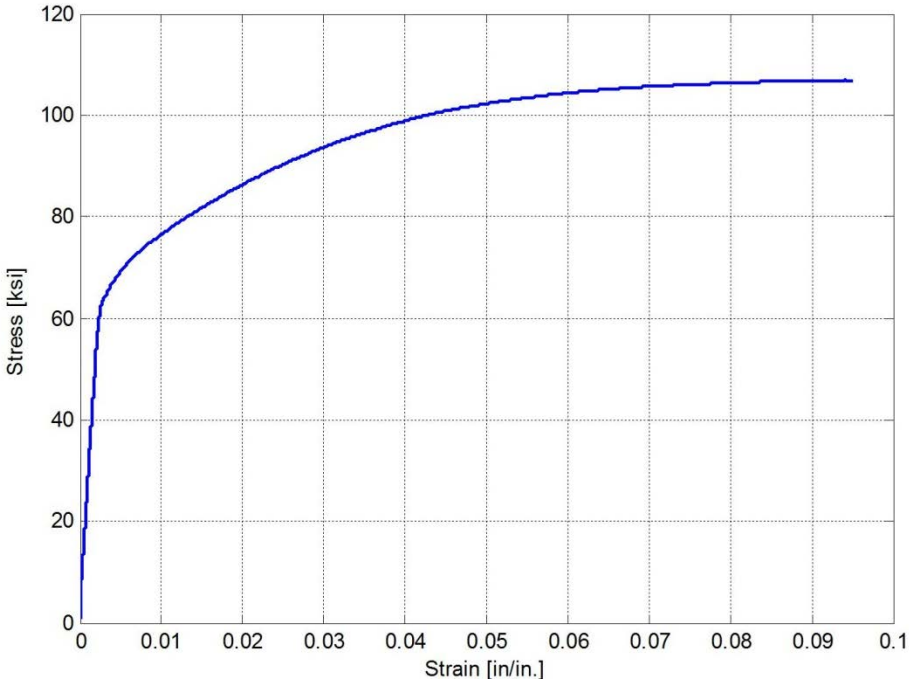

Figure 83. Graph. Stress-strain curve for No. 5 bar.

Table 10. Tensile strength of spiral.

9-gauge wire (psi)	**3-gauge wire (psi)**
109,860	95,050

APPENDIX C: DAMAGE PROGESSION

SPECIMEN DS-1

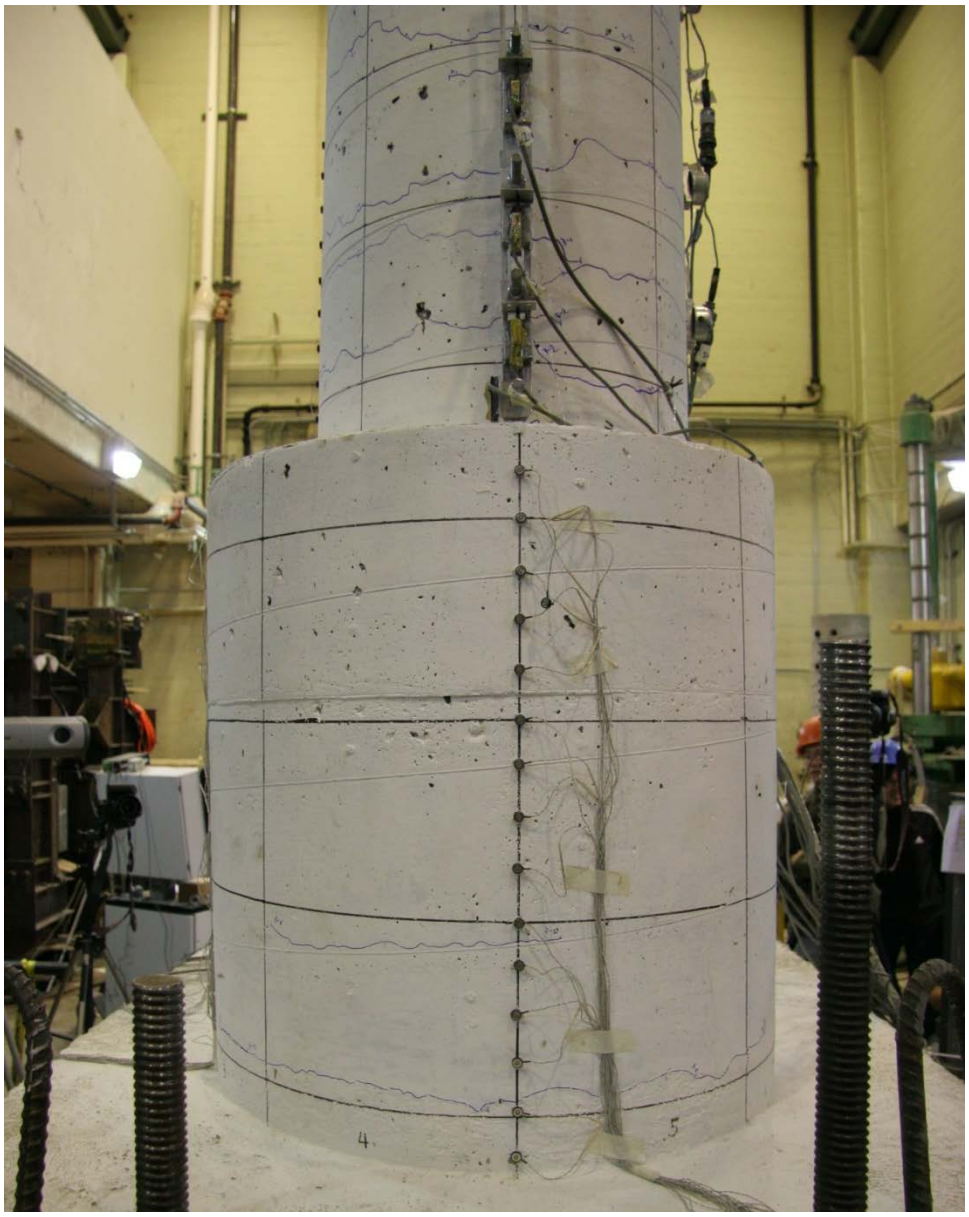

Figure 84. Photo. Specimen DS-1 – significant horizontal crack in cycle 4-1 (0.56/-0.75 percent drift).

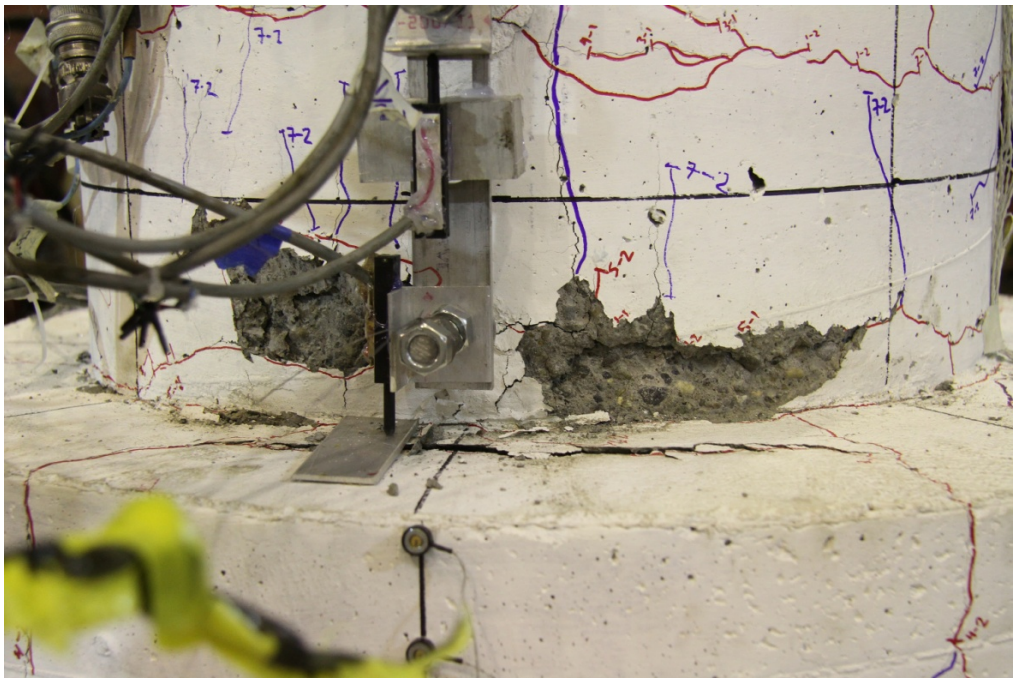

Figure 85. Photo. Specimen DS-1 – first significant spalling occurred in the column in cycle 7-2 (3.00/-3.14 percent drift).

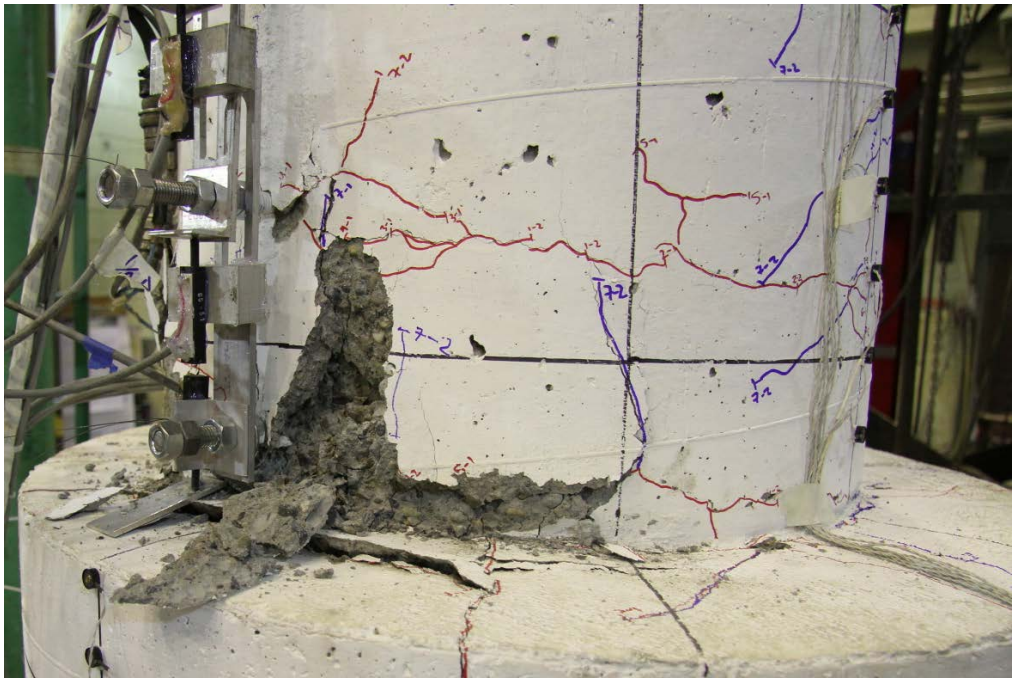

Figure 86. Photo. Specimen DS-1 – plastic hinge formed in the column in cycle 8-3 (4.60/-4.68 percent drift).

Figure 87. Photo. Specimen DS-1 – first noticeable bar buckling in the column in cycle 9-3 (6.90/-6.81 percent drift).

Figure 88. Photo. Specimen DS-1 – first column spiral fractured in cycle 10-1 (8.43/-8.27 percent drift).

Figure 89. Photos. Specimen DS-1 column damage after cyclic testing.

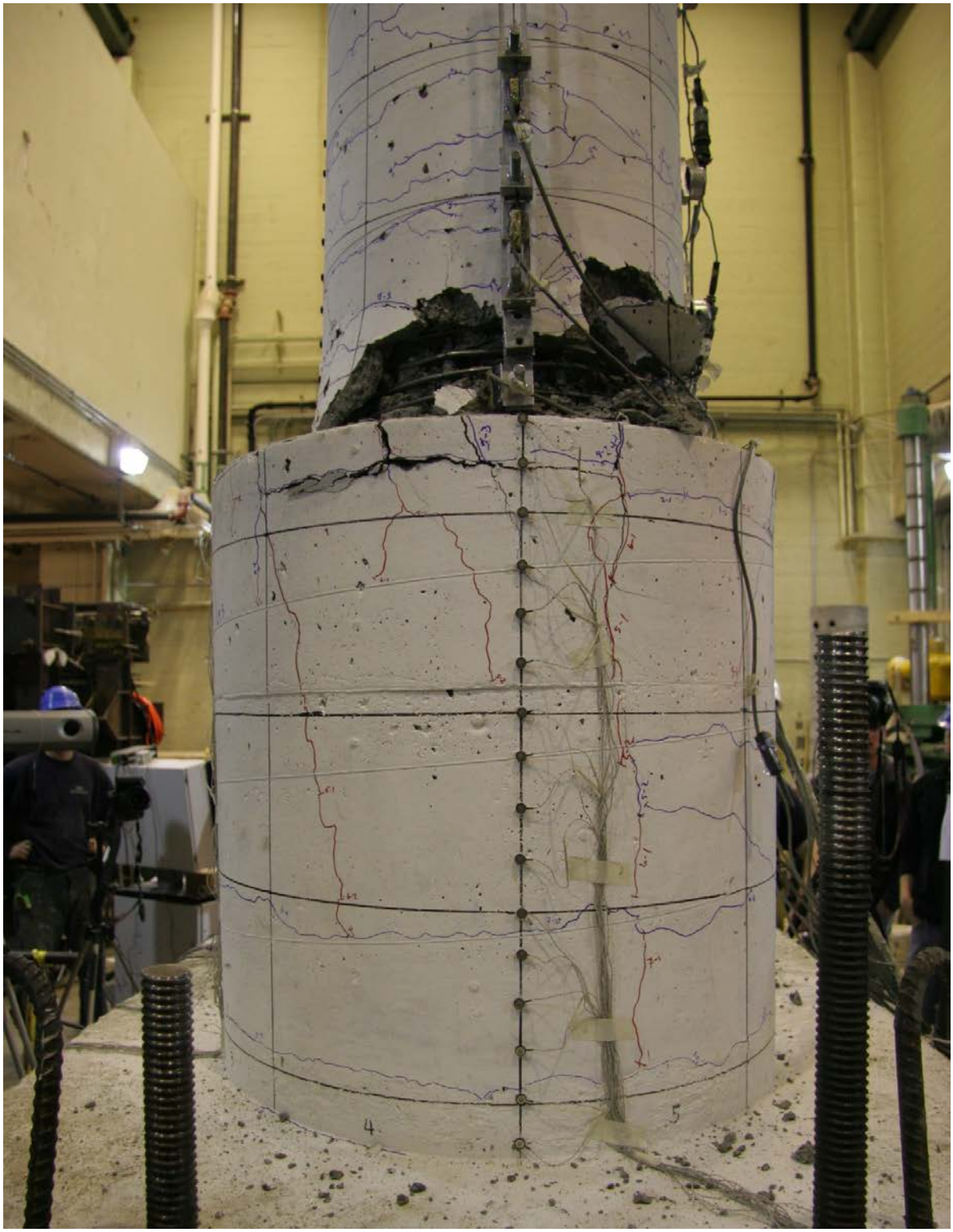

Figure 90. Photo. Specimen DS-1 shaft damage after cyclic testing.

SPECIMEN DS-2

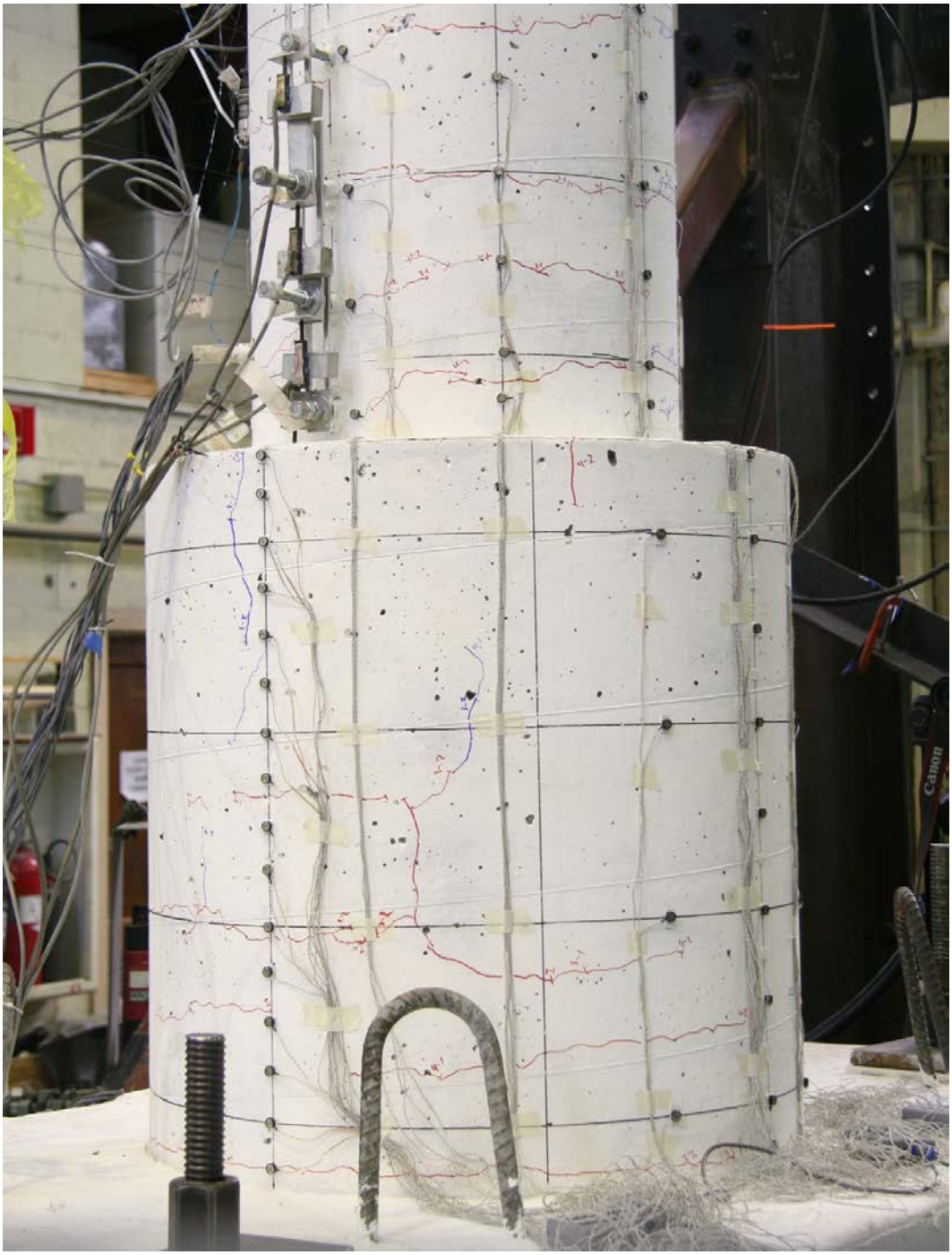

Figure 91. Photo. Specimen DS-2 – significant horizontal crack in cycle 4-2 (0.73/-0.87 percent drift).

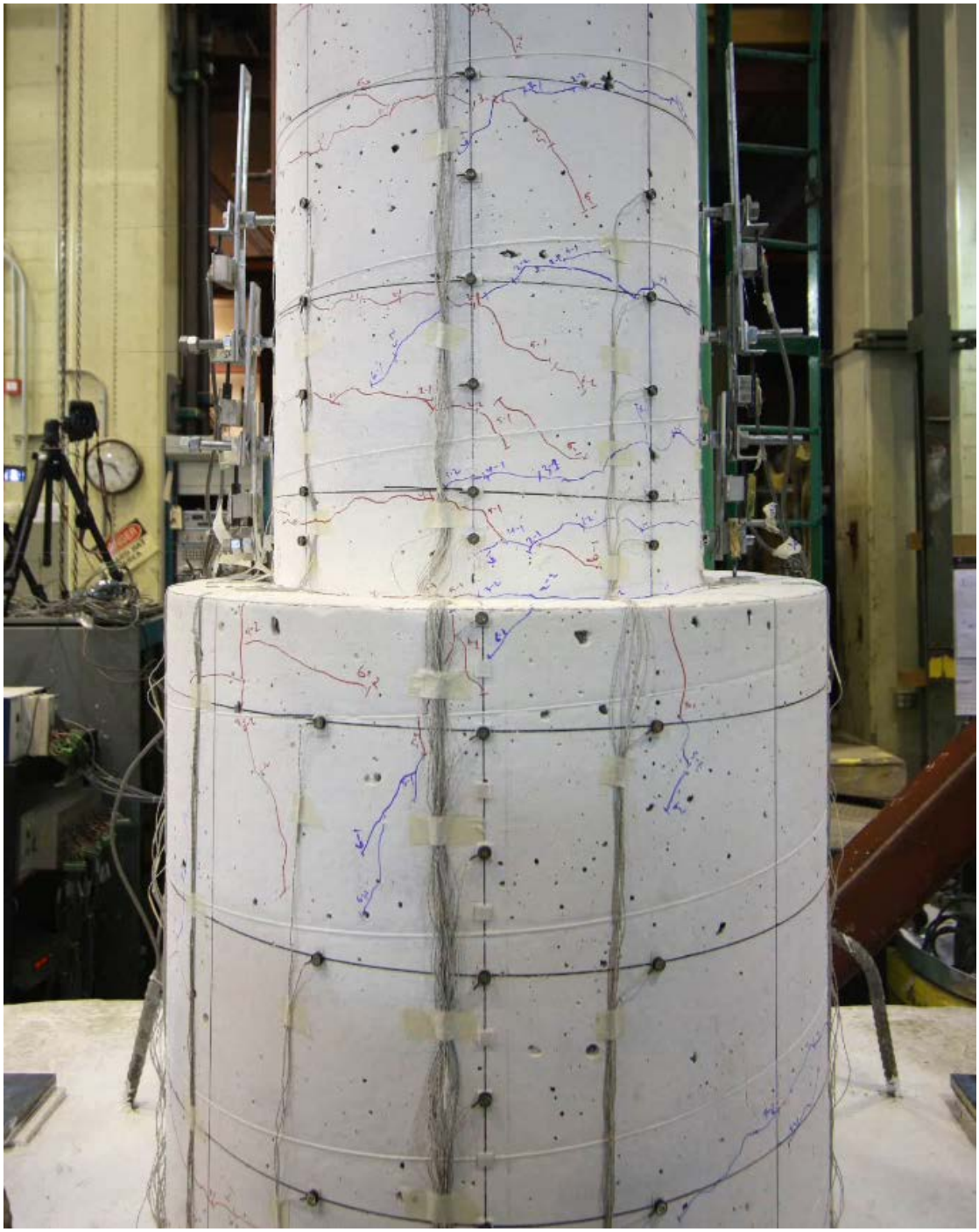

Figure 92. Photo. Specimen DS-2 – first diagonal crack in the shaft in cycle 6-2 (1.87/-2.02 percent drift).

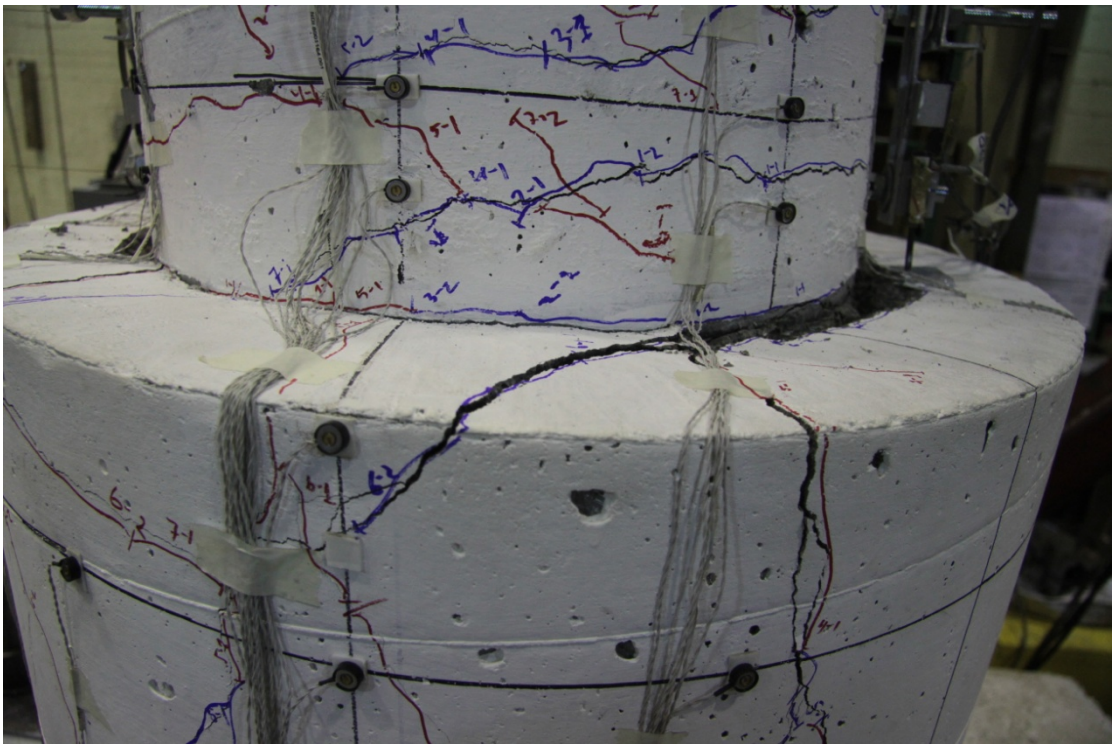

Figure 93. Photo. Specimen DS-2 – shaft damage when first shaft spiral fractured in cycle 8-2 (4.59/-4.59 percent drift).

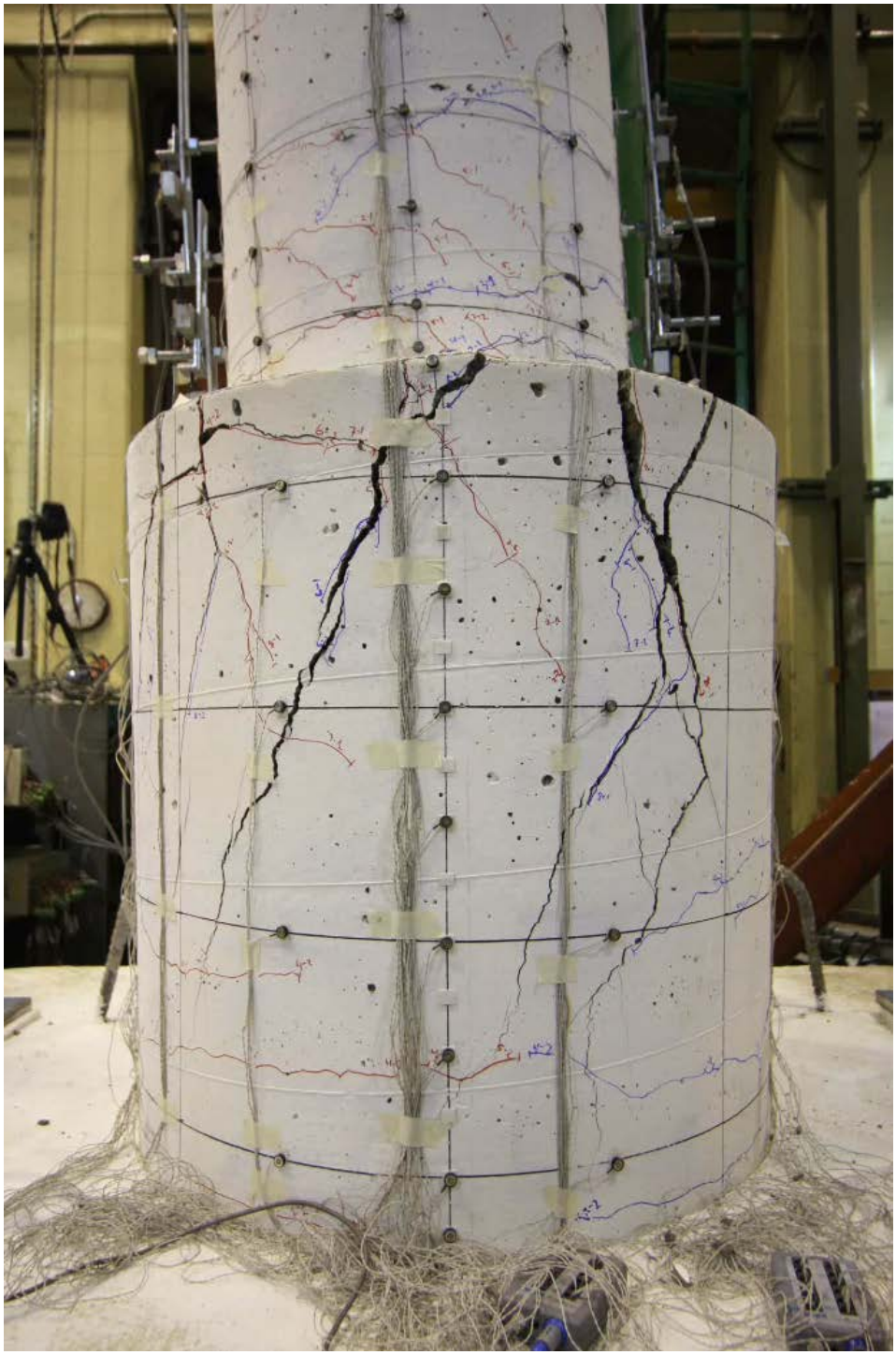

Figure 94. Photo. Specimen DS-2 – first noticeable prying action in shaft in cycle 9-2 (6.72/-6.83 percent drift).

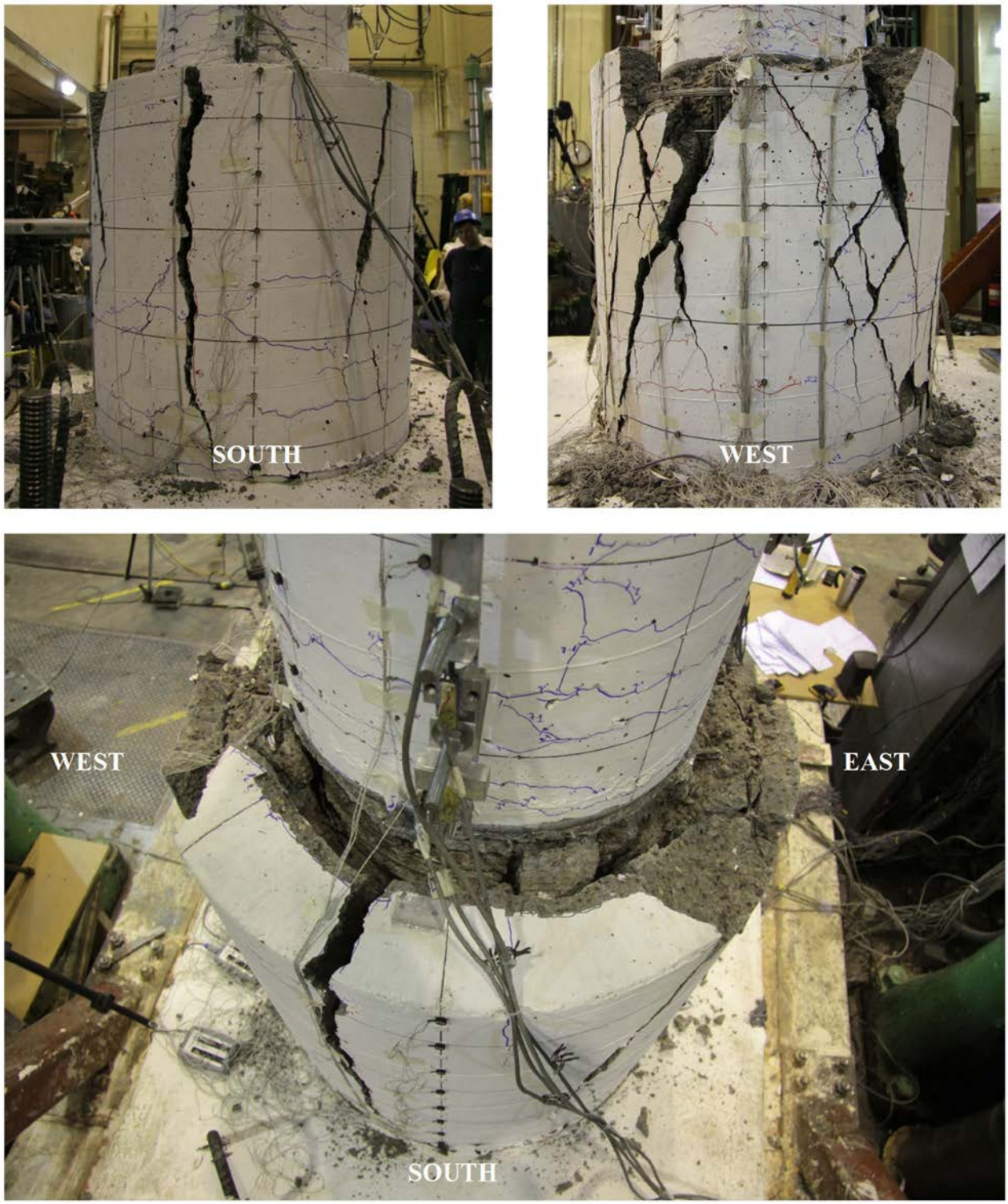

Figure 95. Photos. Specimen DS-2 shaft damage after cyclic testing.

Figure 96. Photo. Specimen DS-2 column damage after cyclic testing.